Electrical, Optical and Structural Properties of CdSe Nanocrystals coupled to Organic π-systems

Dissertation

der Mathematisch-Naturwissenschaftlichen Fakultät

der Eberhard Karls Universität Tübingen

zur Erlangung des Grades eines

Doktors der Naturwissenschaften

(Dr. rer. nat.)

vorgelegt von

Krishan Kumar

Aus Bawwa/Indien

Tübingen

2020

Gedruckt mit Genehmigung der Mathematisch-Naturwissenschaftlichen Fakultät der Eberhard Karls Universität Tübingen.

Tag der mündlichen Qualifikation:	15.01.2021
Stellvertretender Dekan:	Prof. Dr. József Fortágh
1. Berichterstatter:	Prof. Dr. Marcus Scheele
2. Berichterstatter:	Prof. Dr. Heiko Peisert

TABLE OF CONTENTS

Preface

The significant portion of the work presented in this dissertation has been carried out between September 2016 and August 2020 in the Institute of Physical and Theoretical Chemistry at the University of Tübingen in group of Prof. Dr. Marcus Scheele. The fluorescence measurements were performed in the group of Prof. Dr. Alfred Meixner. The Raman measurements and in-house scattering experiments were performed in the group of Prof. Dr. Frank Schreiber in the Institute of Applied Physics. The scattering experiments were also performed at P10, PETRA III, The Deutsches Elektronen-Synchrotron (DESY).

The Theoretical sections in this dissertation are mainly excerpted from:

i. C. N. R. Rao, A. Müller, and A. K. Cheetham, "*The chemistry of nanomaterials: synthesis, properties and applications*", John Wiley & Sons, **2006**.
ii. A. Rose, "*Concepts in Photoconductivity and Allied Problems*" Interscience Publishers,John Wiley and Sons,Inc., **1963**.
iii. B. I. Shklovskii and A. L. Efros, "*Electronic Properties of Doped Semiconductors*", Springer-Verlag Berlin Heidelberg, 1984.

as well as from the research and review articles:

i. Polte, J. Fundamental Growth Principles of Colloidal Metal Nanoparticles – a New Perspective. *CrystEngComm* **2015**, 17, 6809–6830.
ii. Thanh, N. T. K.; Maclean, N.; Mahiddine, S. Mechanisms of Nucleation and Growth of Nanoparticles in Solution. *Chem. Rev.* **2014**, 114, 7610–7630.
iii. Talapin, D. V.; Lee, J.-S.; Kovalenko, M. V.; Shevchenko, E. V. Prospects of Colloidal Nanocrystals for Electronic and Optoelectronic Applications. *Chem. Rev.* **2010**, *110*, 389–458.
iv. Agrawal, A.; Cho, S. H.; Zandi, O.; Ghosh, S.; Johns, R. W.; Milliron, D. J. Localized Surface Plasmon Resonance in Semiconductor Nanocrystals. *Chem. Rev.* **2018**, *118*, 3121–3207.
v. Boles, M. A.; Engel, M.; Talapin, D. V. Self-Assembly of Colloidal Nanocrystals: From Intricate Structures to Functional Materials. *Chem. Rev.* **2016**, *116*, 11220–11289.

This thesis is organized in five chapters.

Chapter 1 is a brief introduction to the topic and provides information on the theoretical basis of the physical process discussed in the further chapters.

Chapter 2 describes the materials and methods used in carrying out this work.

Chapter 3 is a copy of a manuscript by Krishan Kumar, Quan Liu, Jonas Hiller, Christine Schedel, Andre Maier, Alfred Meixner, Kai Braun, Jannika Lauth, and Marcus Scheele titled "Fast, Infrared-Active Optical Transistors Based on Dye-Sensitized CdSe Nanocrystals" published in *ACS Applied Materials & Interfaces* **2019**, 11, 48271-48280. Doi: 10.1021/acsami.9b18236.

Chapter 4 is a copy of an under-review manuscript by Krishan Kumar, Jonas Hiller, Markus Bender, Saeed Nosrati, Quan Liu, Frank Wackenhut, Alfred J. Meixner, Kai Braun, Uwe H. F. Bunz, Marcus Scheele titled "Periodic Fluorescence Variations of CdSe Quantum Dots Coupled to Aryleneethynylenes with Aggregation Induced Emission", *submitted*, **2020**.

Chapter 5 discusses scattering experiments done on the self-assembly of CdSe NCs.

Abstract

This dissertation focuses on the synthesis and optoelectronic properties of coupled organic-inorganic nanocrystal (COIN) thin films. The hybrid materials studied herein are composed of CdSe nanocrystals (NCs) coupled with an organic semiconductor (OSC) material. The CdSe NCs were synthesized using a hot injection method, which requires encapsulation of the NCs with insulating organic ligands. These were removed with inorganic ligand (I^-) to facilitate the electronic coupling and further incorporation of OSCs. The first chapter of this thesis deals with the basis and theoretical background of the field to understand the underlying principles and possible cause of properties displayed by the NCs and modified NC devices. The second chapter focuses on the synthetic methods and various characterization techniques employed to gain insights into the chemical system. In the following chapters, scientific publications are included systematically.

The first article mainly focuses on the study of the optoelectronic properties of the CdSe NCs coupled with zinc β-tetraaminophthalocyanine (Zn4APc). Chemical changes of the thin film device were evaluated by UV-vis-NIR and Raman spectroscopy, while the morphological changes were observed using electron microscopy. Iodide capping of NCs reduces the nearest-neighbor distance, which increases electronic coupling towards mobilities on the order $2.8 - 5.2 \times 10^{-3}\ cm^2/(Vs)^{-1}$. The chosen Zn4APc dye molecule increases the sensitivity of the hybrid device towards light in the visible regime and, more significantly in the near-infrared region, outperforming the otherwise non-functionalized CdSe/I^- NCs device by $2 - 4$ orders of magnitude in photocurrent. The role of Zn4APc was further investigated by transient absorption spectroscopy measurements showing the transfer of electrons absorbed by the dye molecules to CdSe NCs, which was held responsible for the increase in photocurrent. Thus, the role of Zn4APc is to increase the absorption cross-section of the device to the near-infrared region, thereby broadening the absorption window of the material and making the device attractive for utilization in telecommunication devices. By time-resolved photocurrent measurements, we show that the rise time during near-infrared optical gating is $74 \pm 11\ ns$. Time-resolved photoluminescence measurements show a decreased lifetime, *i.e.,* increased nonradiative pathways upon functionalization of CdSe NCs, again establishing the increased electronic interaction between both the moieties.

In the second article, I chose an aryleneethynylene derivative functionalized with eight carboxyl group (AE **1**) binding sites as the OSC for hybrid, CdSe NC-based thin films. The molecule offers a long flexible geometry and exhibits fluorescence enhancement in a highly concentrated environment like thin films, termed aggregation-induced emission (AIE). Absorption and Raman spectroscopy were applied to examine the chemical features of the thin film material. I observed an additional low energy emission band due to AE **1** functionalization of NCs, which I attributed to AIE. The band-edge emission peak and the induced low energy emission peak shows randomly induced anti-correlated fluorescence fluctuation behavior accompanied with $\sim 25\ nm$ peak position shift at room temperature under $488\ nm$ continuous excitation. These fluctuations become periodic at low temperatures, $160\ K$. The periodicity of the ordered fluorescence fluctuations decreases with increasing the laser power at low temperatures. Time-resolved photoluminescence measurements exhibit lifetimes of $0.8\ ns$ at $734\ nm$ and $1.5\ ns$ at $636\ nm$. The transport properties of the COINs film were further explored and showed an increase of more than 3 orders of magnitude in the mobility of the device with temperature and approximately 1 order of magnitude difference in mobility under optical excitation.

The third chapter explores the effect of the unbounded ligand on the self-assembly process of CdSe NCs. I synthesized and characterized two crystalline phases of the CdSe NCs; wurtzite and zinc blende using optical spectroscopy and wide-angle X-ray scattering. NMR spectroscopy experiments were performed to quantify the amount of bound and free ligand on the NCs. Then, we carried out the self-assembly of CdSe NCs using a drop-casting method allowing slow evaporation of the solvent. The self-assembled thin films were then analyzed using small-angle X-ray scattering (SAXS) and grazing incidence small-angle X-ray scattering (GISAXS). Increasing the free ligand fraction (0.97) favored the formation of ordered hcp structure of CdSe NCs in the wurtzite and zinc blende phase. In addition, a 10 % increase in the lattice parameters was observed with the addition of free ligands in the system.

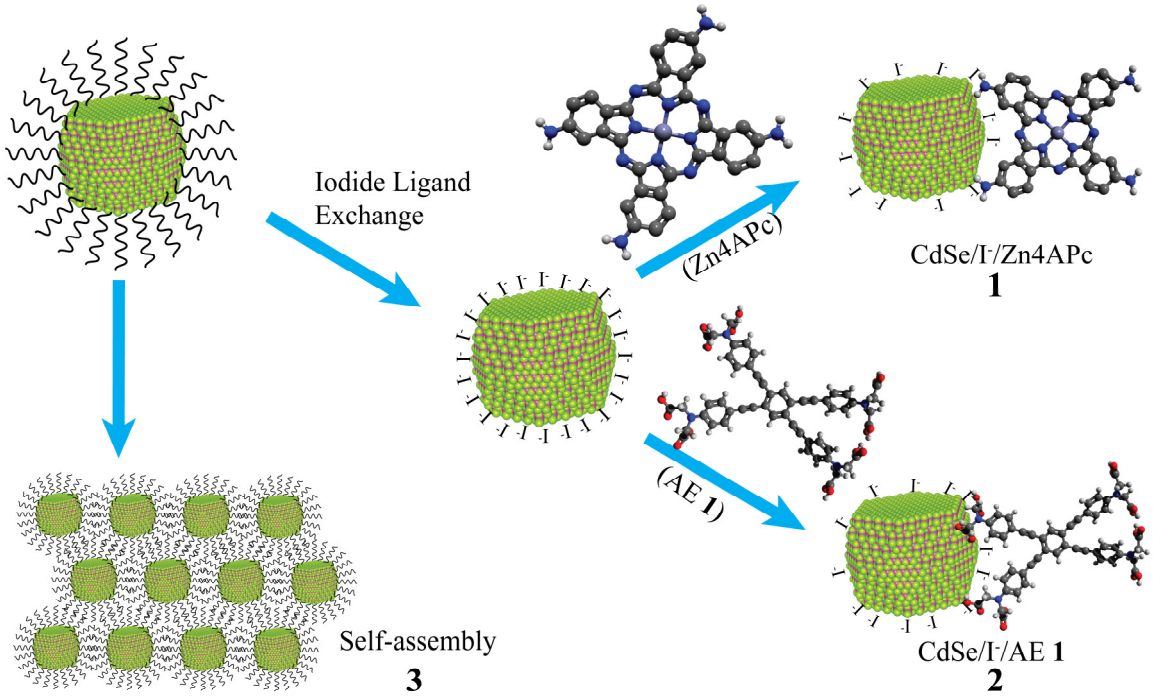

Figure 0-1 Schematic flow of the work presented in this thesis. The first step is the synthesis of the CdSe NCs followed by the iodide ligand exchange. The second step is the incorporation of OSC linker Zn4APc (1) and AE **1** (2). The third step is the preparation of self-assembly of as-synthesized CdSe NCs (3).

1 Introduction

1.1 Background

Nanocrystals refer to small crystals of metal, semiconductor, and magnetic materials with at least one dimension of the order of a nanometer ($10^{-9}\ m$) scale, containing merely a few hundred to thousands of atoms. Developments in this field have led to commercial applications like high contrast display screens and high tensile strength fibers.[1,2] These advancements that we see today essentially have their origin in the discovery of semiconductors in the early *19th* century and humankind's desire to shrink the size of a single useable semiconducting device to store more and more information on a given scale. At present, roughly 100 million transistors per mm^2 are being packed, storing a vast amount of information.[3] This increased information storage demand has brought the size of a single transistor device in the nanometer range and would ideally like it to be of a single atom size. This demand has led to an increased interest of the scientific community to exploit the properties of semiconductor materials in the nanometer regime. However, the use of nanoparticles has been dated back to the middle ages, used for coloring the glasses of the time. However, the science behind it was long hidden. Richard Feynman's talk 'There is plenty of room at the bottom' given in 1959 drew significant attention to the field after being unnoticed for almost two decades, leading Eric Dexler to reposting the question as 'How small we can make a device without affecting the way they work.'[4,5] Further down in history, researchers started to understand the physics associated with these devices and began to explore the change of fundamental properties. However, the research on nanocrystals gained momentum with the generalization of synthesis of cadmium-based semiconductors CdX (X = S, Se, Te) by Murray *et al.,* and the theory of the observed effects was put forward by Brus *et al.* [6–8]

The fundamentally different property mentioned above is that the nanocrystals exhibit intermediate electronic properties compared to individual atoms and their bulk counterpart, owing to the quantum confinement effects. NCs below the Bohr exciton radius, a_B, show a strong band-gap variation on further decreasing the physical dimension of the material. Thus, the semiconductor NCs show strongly size-dependent optoelectronic properties. For example, CdSe and CdS nanocrystals have been shown to exhibit size-dependent band-gap properties.[9,10] Magnetic nanoparticles exhibit superparamagnetism,[11,12] Au, and Ag metal nanoparticles show

shape-dependent surface plasmon resonance where changing the shape of the nanoparticles alters the energy of the plasmon resonance peak.[13,14] Hence the shape, size, and composition are the critical parameters in nanochemistry that control the electrical, optical, and magnetic properties of the system. Due to the tiny size of NCs, they have a large surface to volume ratio, which is desirable for catalytic applications.[15,16] It is well known that the surface atoms have unsaturated valencies or dangling bonds, their passivation with linker molecules provide a handle to modify the electronic states (mid-band-gap states), surface energy, and reactivity of these NCs system. Therefore makes them very useful in achieving the desired electronic properties.[17] Long-chain organic ligands typically used during the synthesis of NCs have higher energy gaps, acting as a barrier in the electronic coupling of the nearest neighboring NCs. This energy barrier can be suppressed by decreasing the ligand length, by replacing it with smaller inorganic/organic ligands[18–25] or by carefully choosing an organic ligand of a suitable bandgap.[24,26,27] Enhanced electronic interactions make NCs a promising candidate for their application in field-effect transistors (FETs), vapor sensors, and photonic devices.[28–34] CdSe nanocrystalline material is very well studied and easily synthesized & reproduced with very narrow size distribution. CdSe NCs have high absorption coefficients in the visible light range, making it a suitable candidate from an electronic and photoconductive application standpoint. Semiconducting CdSe has low dark current owing to its low intrinsic charge carrier density, which is desired for designing photonic devices such as a telecommunication device. A telecommunication device receives the photonic signal of a specific wavelength and converts it to an electrical signal. Thus, a material having a high on-off ratio in the telecommunication window is required. These specialties have brought this class of materials to the main spotlight of research. Recently, there has been a growing interest in exploiting the electronic properties of the NCs.

This work focuses on the optoelectronic properties of coupled organic-inorganic nanostructures (COINs) based on CdSe NCs and organic semiconductors (OSC), specifically Zn4APc and an aryleneethylene derivative. The CdSe NCs used in this thesis were prepared using a colloidal hot injection method, and OSCs were either commercially available or supplied by the University of Heidelberg as described in the respective chapters. Insulating native organic ligands were then exchanged with a small inorganic ligand, I^-, for easier subsequent exchange with OSC ligands. Then the electrical, optical, and photoconductive

properties of thin films of these conductive COIN systems were studied, and their results are presented here in this thesis.

1.2 Nanocrystals Synthesis

The synthesis of NCs is usually performed either by physical or chemical processes. The physical process of nanocrystals synthesis is the "top-down" process, which encompasses the size reduction of bulk precursor material to the desired nanocrystals size range, e.g., the scotch-tape method, mechanical processes like grinding and polishing steps. However, such methods are physically demanding, destructive, and difficult to reproduce.

The chemical process often follows the "bottom-up" approach for nanoparticle synthesis, be it the wet chemical process, sol-gel method, reverse micelle templating, or the hydrothermal method of synthesis. The three essential components required for the wet chemical method are precursors, organic surfactants, and solvents. Sometimes the solvent can also act as a surfactant. In a typical synthesis, the precursor is first turned into a more chemically active form atomic or molecular form called a monomer, either by swift addition into the reaction mixture or by attaining a certain temperature. Then the NCs are allowed to grow for a certain period of time, and then the reaction is quenched by an abrupt change in temperature or by the addition of quenching solvent. The following sections discuss the theoretical basis of any general colloidal synthesis consisting mainly of two steps: 1) nucleation and 2) growth of formed nuclei to synthesize NCs of the desired size. The nucleation process of nanocrystals is described by the classical nucleation theory (CNT), and its adaptation for nanocrystal systems (LaMer's theory, see section 1.2.1.3). The growth process of the formed nuclei, their kinetic and thermodynamic aspects may be used to form different shapes or sizes of NCs.

1.2.1 Classical Nucleation Theory

The classical nucleation theory (CNT) developed by Becker & Dönring originally described the phase transition from vapor to the liquid.[35] Later, this theory was adapted for other phase transitions, and LaMer further extended it for NCs synthesis as well.[36] CNT theory only describes the nucleation process. Nucleation is purely dependent on the thermodynamic stabilization, i.e., a decrease in the formed clusters' Gibbs free energy. The nuclei formation

can be described as a first-order phase transition. The subsequent sections will discuss the nucleation process in more detail. However, CNT does not explain the later stages or kinetics of NCs formation. Further NCs growth from nucleation can be described by the addition of monomers onto the nuclei, aggregation, or by Ostwald ripening. In this context, it is essential to distinguish between homogeneous nucleation, which is rapid, random & simultaneous and does not require nucleation sites, rather it requires a supersaturated monomer solution, whereas heterogenous nucleation requires a nucleation site which could be the phase boundaries or impurities.

1.2.1.1 Homogeneous Nucleation

The Gibb's free energy for the spherical cluster is given by equation (1):

$$\Delta G = -\frac{4}{3}\pi r^3 |\Delta G_v| + 4\pi r^2 \gamma \tag{1}$$

where r is the radius, $|\Delta G_v|$ is the difference of Gibbs free energies per unit volume, γ is surface energy per unit area. The overall Gibbs free energy depends on two competing factors: the negative term (first term, favorable) and positive term (second term, unfavorable). The negative term (favorable one) is the volume or bulk energy term, representing the bond formation between monomer and cluster or between two monomers. While the positive term (unfavorable one) is the surface energy due to the formation of the bond, as mentioned earlier **Figure 1-1a**. Therefore, a critical radius r_c is defined as $r_c = {}^{2\gamma}/_{|\Delta G_v|}$ by solving equation (1) for $d\Delta G/dr = 0$ below which the surface energy term dominates that restrict the growth process and promotes the dissolution. Above r_c, the bulk energy term dominates and growth is favorable.

1.2.1.2 Heterogeneous Nucleation

The heterogeneous nucleation occurs preferentially at the phase boundaries since the effective surface energy for the nucleation process is lower at surface boundaries. Once the nuclei are formed, further nucleation will occur, preferably on the already formed nuclei. Heterogeneous nucleation is often more probable; however, in NCs growth, both type of nucleation coincides.

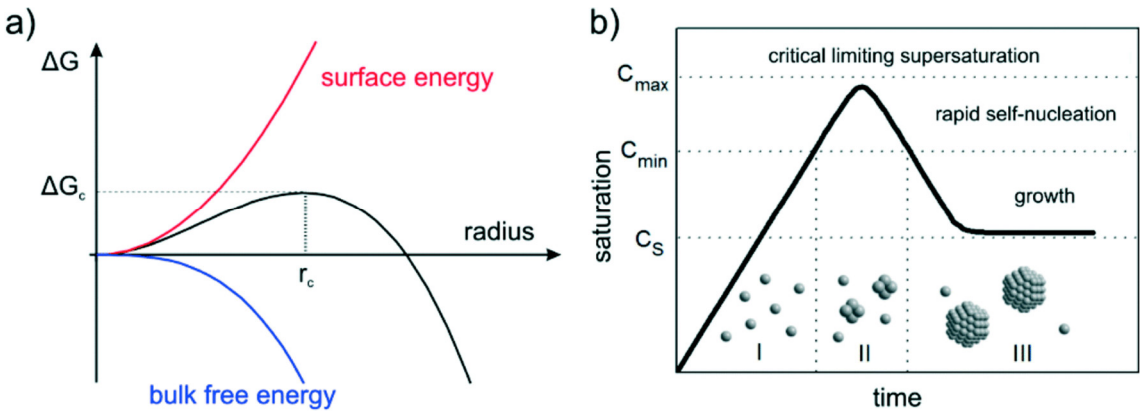

Figure 1-1 (a) Gibbs free energy change of a cluster with it's radius, r as given by CNT theory. (b) Time profile of concentration change during sulfur nucleation given by LaMer theory adapted from CNT theory. Adapted from ref.[37]. Copyright 2015 The Royal Society of Chemistry.

1.2.1.3 LaMer's Nucleation Theory

LaMer, in the 1950s, described the nucleation process of metal nanoparticle synthesis by burst nucleation through his pioneering work on oil aerosols and sulfur hydrosols.[36,38] LaMer's nanoparticle synthesis relies on the separation of nucleation and growth steps for narrow size distribution. **Figure 1-1b** outlines the mechanism of NCs formation. In phase I, the monomer concentration first increases rapidly, either by swift injection of the precursor or due to reaching a certain temperature to form monomers, and the monomer concentration attains its saturation concentration (C_s). However, for nucleation to occur, a particular energy barrier must be overcome just like in any other chemical process. In phase II, once the concentration exceeds a certain minimum concentration (C_{min}) to cross the activation energy barrier, the homogeneous nucleation burst occurs, marking the nucleation event, and the monomer concentration falls rapidly below the C_{min}. Further nucleation almost stops and the growth of nuclei starts, forming the NCs of required size in phase III.

LaMer's nucleation theory and its modifications are well-accepted theories for general nanoparticle synthesis. In principle, this model also helps to understand the size of the formed nanocrystals. A rapid increase in monomer concentration induces a burst of nucleation, allowing the formation of many small nuclei and fewer larger nuclei to be formed during the process, leading to smaller sizes of obtained NCs. Moreover, the principle of "seeded-growth" derived from classical nucleation (*i.e.,* slow addition of monomer) allows fewer nuclei formation and further growth on the already formed nuclei leading to larger sizes NCs. However, LaMer's theory does not comment on the nanoparticles' growth kinetics; instead, it

only describes the nucleation process. The kinetics of the colloidal semiconductor, especially for CdSe and InAs were investigated by Alivisatos and co-workers, observing the focusing and defocusing events in the nanoparticle synthesis.[39]

1.2.2 Non-Classical Nucleation Models

The CNT comprehensively describes a few aspects of NCs synthesis. However, CNT assumes a precise phase boundary between monomer and nuclei formation. It also defines an energy barrier to reach the homogeneous nucleation during synthesis. Furthermore, CNT assumes that γ and ΔG_v are independent of the size of the cluster and do not change during the synthesis process; however, this is not entirely the case. Two other models exist in the literature, namely the spinodal decomposition and the non-classical nucleation model. The spinodal decomposition model assumes that the surface free energy of the nuclei is negligible compared to the bulk free energy. So, practically there exists no energy barrier, and hence the process co-occurs with a phase difference throughout the synthesis. While the non-classical nucleation model assumes a situation in between the two extremes, *i.e.,* it considers γ, ΔG_v to be dependent on the size of the cluster. In principle, this assumption lowers the nucleation energy barrier depicted by CNT. It makes room for local minima in the energy landscape, which argues for the two-step nucleation process. At first, metastable amorphous nuclei are formed, which has the surface energy close to the supersaturated solution. After a specific size, the transition of amorphous nuclei to crystalline nuclei occurs when the bulk free energy takes over the surface energy. Model 2D crystallization studies have also favored this two-step nucleation process under low supersaturation.[40,41] Similar two-step process has also been observed experimentally in the colloidal crystallization of charge-stabilized polystyrene spheres and also CdSe NCs.[42,43]

1.2.3 Shape and Size Distribution

Many kinetic and thermodynamic factors play an essential role in determining the shape and size distribution of the NCs. Reports have shown control of shape and sizes by carefully monitoring the kinetic and thermodynamic aspects of NC during the synthesis.[44] Additionally, the monomer concentration has its influence on the shape of the NCs. CdSe, CdTe semiconductor NCs synthesis have been shown to form different shapes under different monomer concentrations.[45,46] Two crucial steps mainly govern the monomer concentration

influence on the shape: first, the deposition of a monomer onto pre-formed nuclei and second is the monomer's diffusion rate to a more stable thermodynamic site. For thermodynamically controlled growth, the rate of diffusion of the monomers to a more thermodynamically favored site should be faster than the rate of chemisorption of monomer. In contrast, the reverse would be the case for the kinetically controlled growth of NCs, thus leading to the formation of less thermodynamically stable shapes of NCs.

The equilibrium shape would have the lowest Gibbs free energy, as given by equation (1). Hence, the surface energy density (γ) corresponding to any given shape should be minimized over the entire surface area to reach the equilibrium shape of the NCs, provided that sufficient time is given for the growth of the NCs. If the surface energy is considered to be independent of the growth direction, then isotropic shape would have the lowest exposed surface area for any given volume. However, this is generally not the case for crystalline materials owing to their intrinsic atomic anisotropy present in the system. The surface energy is strongly dependent on the crystallographic orientation of the crystals and behaves differently for different crystal orientations, providing a tool for shape-controlled NCs synthesis.[44,47] In other words, entirely spherical nanocrystal formation is highly unfavorable as it requires the termination of many crystallographic planes, which cost significantly in terms of the surface energy of the particle. Also, surfactants can show different binding strengths to the crystal facets altering the shape of the NCs.[48–50] Kinetically; it means that the surfactant molecules could increase the activation energy barrier for chemisorption of monomers by binding to the preferred crystallographic direction, thus stopping further growth along that direction.

The detailed mechanism and theory describing the shape and size distribution of NCs synthesis have been summarized in literature and have been omitted from this thesis.[51] Through the interplay of these parameters, the growth of nanocrystals can be tuned to design novel materials for future applications.

1.3 Electronic Structure of Nanocrystals

Solid materials can be classified into three different categories: metal, semiconductor, and insulator categories, depending on the electronic structure of the system. Metal is the class of material which, at a microscopic level, has overlapping valence and conduction band facilitating the flow of electrons, thus allowing the charge conduction. Semiconductors have a

finite forbidden energy gap ($< 3\ eV$) between the filled valence and empty conduction band, thus requiring some extra energy to promote electrons from the valence to the conduction band. In contrast, insulators have a band-gap $> 4\ eV$, too large for electrons to jump to the conduction band. This electronic picture in metals is practically retained to all size ranges of the crystal domain. Semiconductors exhibit an exciting variation in electronic properties as the crystallite size is reduced to the nanometer-regime. For semiconductors below the Bohr exciton radius, a_B, the energy level spacing increases with further decreasing physical size of the material. Essentially, NCs can be treated as a particle-in-box like problem for energy state calculation. However, by definition, quantum dots have broken the translational symmetry (present in the bulk system), thereby preventing the simplification in terms of the Fourier-Transformation of real space into momentum space.[52] Hence, one would have to deal with the problem in real space, having a Hamiltonian matrix of dimensions equal to the number of mixing orbitals and thus escalating the resources needed. Accordingly, the problem with theoretical electronic structure calculations is that NCs are too big for the *ab initio* techniques (10^5 electrons) and too small to apply lattice periodicity simplifications. In literature, three methods have been used extensively to address this problem, namely, the effective mass approximation (EMA), the empirical pseudopotential method, and the tight-binding (TB) method.[52] These methods have their advantages and disadvantages. The effective mass approximation method is described in more detail in the following section.

1.3.1 Effective Mass Approximation (EMA)

Generally, the unit cell of nanocrystals stays the same as that of bulk material. Therefore, the molecular orbitals (MOs) of nanocrystals will evolve to Bloch type wavefunction (used in solving Schrödinger equation for bulk materials) with increasing nanocrystal size. Under these conditions, the effective mass approximation (EMA) can be used to calculate the electronic properties of NCs. Using EMA to describe the band-gap dependence on the size, one needs to solve the Schrödinger wave equation for electrons and holes of the nanocrystals, given in equation (2):

$$\left[-\frac{\hbar^2}{2m_e}\nabla_e^2 - \frac{\hbar^2}{2m_h}\nabla_h^2 - \frac{e^2}{4\pi\varepsilon_0\varepsilon r_{eh}} + V_0\right]\psi(r_e, r_h) = E\psi(r_e, r_h) \tag{2}$$

Here e, h subscripts stand for electron and hole with m, r being their masses and position vectors, respectively, and $r_{eh} = |r_e - r_h|$. The permittivity of free space is represented by ε_0 and ε is the dielectric medium.

For an infinite potential outside the box and zero potential inside the box, Efros and Efros,[53] Brus[7,54,55] and Kayanuma[56,57] proposed the following equation for the band-gap variation for nanocrystal of radius R:

$$E^* \approx E_g + \frac{\hbar^2\pi^2}{2R^2}\left[\frac{1}{m_e} + \frac{1}{m_h}\right] - \frac{1.786e^2}{\varepsilon R} - 0.248E^*_{Ry} \quad (3)$$

Here E_g is the bulk band-gap of the semiconducting material. The second term in the solution is the kinetic energy of the non-interacting electron and hole, whereas the third and fourth term corresponds to the Coulomb interaction and spatial correlation between electron and holes. E^*_{Ry} is given as:

$$E^*_{Ry} = \frac{e^4}{2\varepsilon^2\hbar^2(m_e^{*-1} + m_h^{*-1})} \quad (4)$$

Equation (3) describes the band-gap variation, as depicted in **Figure 1-2**. For nanocrystals of larger size, infinite potential (IP)-EMA is well suited for assessing the band-gap dependence on the size of the NCs and has been used to describe the system properties.[58] However, in smaller size regimes, this model vastly overestimates the band-gap energy change. Two limiting cases have been identified depending on the Bohr radius, a_B of the bulk solid. For $R/a_B \gg 1$, the exciton can easily be pictured as a particle moving inside the quantum dot with only a small energy change due to confinement effects. This is called the weak confinement regime. Another limiting case $R/a_B \ll 1$, in this regime the confinement effects dominate called the strong confinement regime. However, Kayanuma *et al.* observed that electrons and holes should be treated as individual particles due to the increased contribution of kinetic energy. They further noted that the strong confinement regime is not just limited to $R/a_B \ll 1$, rather it extends upto $R \approx 2a_B$.

The IP-EMA model considers infinite potential outside the box and hence does not include the tunneling of the wavefunction beyond the barrier. Therefore, it excludes the effect of the ligand sphere and the surrounding material. However, the IP-EMA model has been

modified and solved for a finite potential barrier to consider the effects of the surrounding material.[59] Also, the multiband EMA (MBEM) theory provides a substantial improvement over single band IP-EMA to address the effective mass of holes, which requires a larger number of bands. Such improvements in IP-EMA provide a good explanation of the experimental data.

Norris *et al.* has used EMA to theoretically model the narrow size distribution CdSe QDs in diameter range over 19 to 115 Å, including spin-orbit coupling, valence band degeneracy, and non-parabolicity of the conduction band.[60] They were able to model and assign up to ten transitions in CdSe QDs in the strong confinement regime, *i.e.,* having higher confinement energy than the coulombic interactions. The model overestimates the confinement energy with decreasing size, yet they were able to manage the error to a minimum level by considering only one excited electronic level ($1S_e$), which is generally all the lowest allowed transition includes.[60,61]

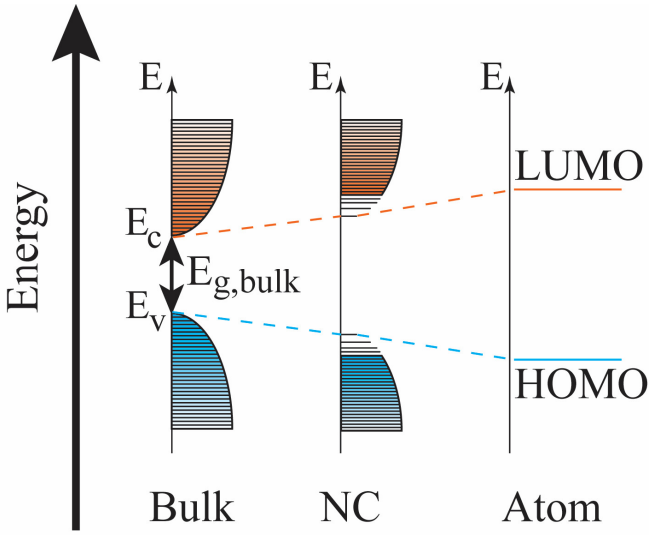

Figure 1-2 Schematic representation of increasing band-gap from bulk to individual atom.

1.4 Coupled Organic-Inorganic Nanocrystals

Organic ligands like oleic acid (OA), oleylamines (Olm), tri-octylphosphine oxide (TOPO), tri-octylphosphine (TOP) used during the synthesis of the NCs, play a crucial role in their shape and size determination. During self-assembly of the NCs, ligand-ligand interactions influence the ordering of NCs and their interparticle distance. Therefore, these ligands have a significant role in overall NCs properties. However, these ligands have high band-gaps between their HOMO-LUMO state, acting as an energy barrier in electronic interactions between the

neighboring NCs. Hence, as synthesized NCs usually have limited applications in electrical devices. For efficient electronic coupling between NCs, organic insulating ligands have been replaced with smaller inorganic ligands such as halides, sulfides, thiocyanate, metal chalcogenides, metal halides complexes, and oxalates. [18–21,62,63] These small inorganic ligands are attached to the NCs through Coulomb interactions and have a very weak or no covalent bonding interactions. Another way to increase the electronic interactions is by using organic semiconductor (OSC) ligands, either covalently bound or attached by weak van der Waals interactions. There is a large variety of OSCs available in the literature. OSCs having a suitable position of frontier orbitals could be used to fine-tune the NCs for desirable optoelectronic properties. A similar analogy of band alignment within inorganic core-shell systems can be used to understand interactions between NCs and organic ligands. Long-chain insulator organic ligands have a large energy gap and form a type I band alignment with most inorganic NCs and confine the exciton within the system. The inverted scenario of band positioning is called inverted type I, which leads to the leakage of the electron-hole wavefunction into the organic ligand, where eventually, the charge carriers will recombine. Bands closely spaced on energy landscape form type IIa or IIb and spatially separate the charge carriers due to their energy difference, increasing the recombination time.[64] This band positioning and its effect have been well studied in the literature on core-shell inorganic nano-heterostructures and coupled organic-inorganic nanocrystals (COINs).[65–67] CdSe NCs functionalized with tetrathiafulvalene

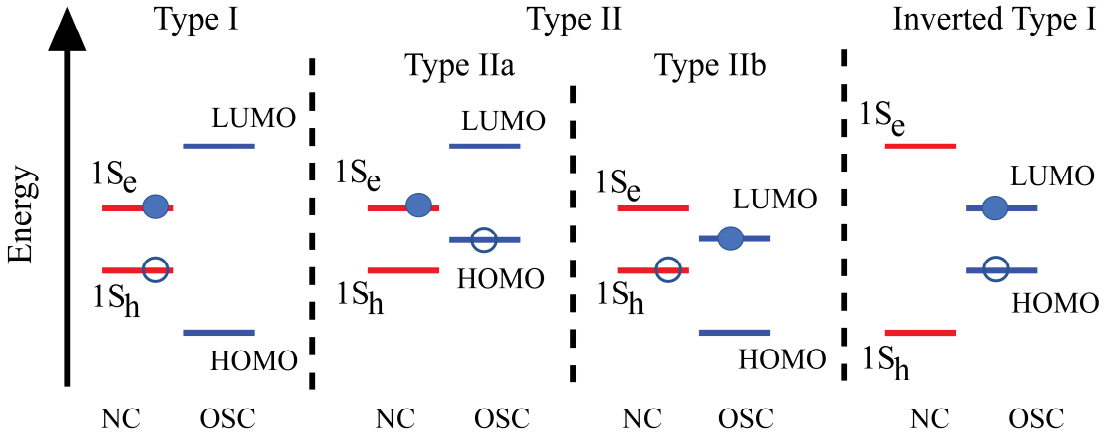

Figure 1-3 Schematic of energy band positions of NC and OSC to show different types of band-alignments. Type I (left), Type II (middle) have two possible alignments (Type IIa or Type IIb), and inverted Type I arrangement. Solid and empty circle, representing electrons and holes, respectively, show the likely residing positions in the arrangement.

tetrathiolate (TTF-S_4) can be considered to be the first report of COIN in 1993 by Majetich *et al.* [68]

1.5 Charge Transport in NCs assemblies

Another important aspect of these COIN systems is the charge transport studies in NCs composed of thin-films.[65,69] For inorganic semiconductor NCs, such as CdSe[70,71], PbS[26,27,71–74], ITO[24,75], CuS[76–78] functionalized with OSCs have been investigated for their *I-V* characteristics in literature. The charge transport in NCs assemblies mainly depends on two conditions: 1) the transfer integral (β) should be larger than the charging energy (E_c), *i.e.* energy required to add extra charge carrier in the neighboring nanocrystal, and 2) β should be larger than the average energetic fluctuations ($\Delta\alpha$) caused by disorder in the nanocrystal assemblies.

1.5.1 Coupling Energy (β)

The transfer integral or coupling energy is a measure of interactions between the NCs which depends on the tunneling rate of electrons from one NCs to neighboring one:

$$\beta \approx h\Gamma \tag{5}$$

where h is the Planck's constant, and Γ is the tunneling rate constant with an energy barrier ΔE of width Δx.

$$\Gamma \approx \exp\{-2(2m^* \Delta E/\hbar^2)^{1/2}\Delta x\} \tag{6}$$

As synthesized, NCs have long chain insulator ligands, which provide a large tunneling barrier to charge transfer as the tunneling rate varies exponentially with the barrier width Δx. To improve coupling between the NCs, the barrier height and width should be decreased by inserting shorter inorganic ligands or conjugated OSC ligands.

1.5.2 Charging energy and energetic disorder

The charging energy is the energy required to add an extra electron to the electronically neutral NCs. The charging energy depends on the self-capacitance (C_{self}) and mutual capacitance (C_m) of the NC. It is given by equation (7):[79]

$$E_c = \frac{e^2}{2\left(C_{self} + nC_m\right)} \tag{7}$$

Here n is the average number of nearest neighbors. The self-capacitance of spherical NCs of radius, r and dielectric constant (ε_{QD}) surrounded by a ligand matrix of dielectric constant (ε_{matrix}) is given by equation (8):[65]

$$\frac{1}{C_{self}} = \frac{1}{4\pi\varepsilon_0}\frac{\varepsilon_{QD} - \varepsilon_{matrix}}{\varepsilon_{QD} \times \varepsilon_{matrix}} + \frac{0.94}{4\pi\varepsilon_{QD}\varepsilon_0 r}\frac{\varepsilon_{QD} - \varepsilon_{matrix}}{\varepsilon_{QD} + \varepsilon_{matrix}} \tag{8}$$

The dielectric constant of the NC depends on its size, which can be described using the Penn model.[80,81] The mutual capacitance of the NCs with center-to-center distance (D) is given by equation (9):[25]

$$C_M \approx 2\pi\varepsilon_0 \frac{\varepsilon_{QD}\varepsilon_{matrix}}{\varepsilon_{QD} - \varepsilon_{matrix}} r\, ln\left(\frac{D + 2r}{D}\right) \tag{9}$$

Equations (7–9) show the dependence of the charging energy on the dielectric constants of the NC and the ligands as well as the distance D. It is also noteworthy that E_c always works against the transport of the electrons, *i.e.,* charging energy has to be paid twice for one electron to move from one NC to another. In the weak coupling regime or larger D, that is $\beta \ll k_B T$, there exist a Coulomb gap between the energy states of the NCs, which at low applied bias cannot be overcome by charge carriers, and the transport is blocked. Only at higher applied bias, this gap can be overcome and allowing the charge transport. This gap is called the Coulomb gap or the Hubbard gap (see **Figure 1-4**). As the distance D decreases, the charge carrier wavefunctions start to extend over several neighboring NCs. This is called the strong

coupling regime ($\beta > k_B T$) where a continuum of molecular-like bands would exist allowing the flow of charge carriers easily. This crossover point is called the Mott metal-insulator transition (**Figure 1-4**). This transition is characterized by a sudden change in the transport properties of the system as the temperature coefficient of the resistance is changing its sign from negative to positive. These phenomena have been studied in Ag NCs where the interparticle distance is decreased from 12 ± 2 Å to 5 ± 2 Å using Langmuir-Blodgett techniques as well as in Au NCs film capped with C_nS_2 ligand behaving as an insulator (n>5, *i.e.,* larger interparticle separation) & as metallic (n<5).[82,83]

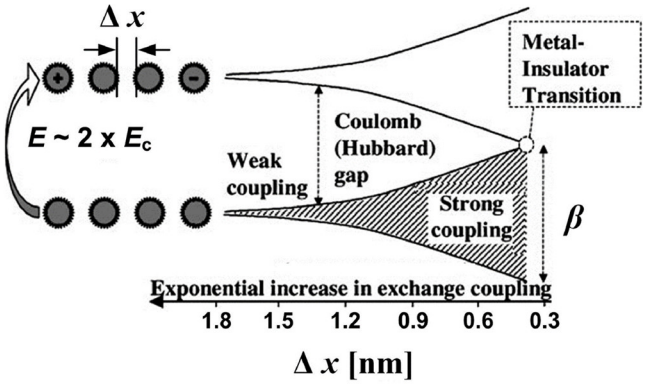

Figure 1-4 Effect of interparticle separation of NCs on electronic structure variation. Decreasing Δx will reduce the Coulomb gap and extending the charge carrier wavefunction over multiple NCs. Eventually, the film would cross the Mott metal-insulator transition point extending wavefunctions over entire NCs solid film. Taken from ref.[84]. Copyright 2000 Annual Reviews.

Another vital parameter to consider in the transport mechanism is the energetic disorder ($\Delta\alpha$). As it is almost impossible to synthesize atomically precise NCs, there will always exist a size distribution of the NCs. This size distribution and structural orientation lead to a significant energetic distribution in NCs states that hinders the transport of charge carriers. The interplay of β and $\Delta\alpha$ will lead to an essential Metal-insulator transition phenomenon, called Anderson localization, which physically refers to the separation of strongly coupled regimes from weakly coupled regimes in NC films.

1.6 Field-Effect Transistor

Field-effect transistor (FET) devices are the second-generation of bipolar junction transistors (BJT). In general, BJT devices are governed by diffusion mediated minority charge carriers. Specifically, FET devices are unipolar and governed by drifting of charge carriers

controlled by the applied gate potential. FET devices have several key advantages over simple BJT's such as simple operation, fabrication procedure, and smaller size, *i.e.,* a higher number of devices per given area of the chip. Therefore, at present, these devices are predominant in integrated circuits. FET devices (**Figure 1-5**) have three terminals, just like the BJTs. However, the terminology is somewhat different. FET devices have "source & drain" electrodes, and the area between them is called the "channel" being the semiconductor material. The source terminal acts as the source of charge carriers, which goes to the drain terminal with some conductance. The "gate" electrode influences the conductance or the carrier concentration. Such a FET device has been categorized as junction field-effect transistors (JFET or FET) and metal oxide semiconductor field-effect transistors (MOSFET). Two main characteristics describe FET devices: 1) Output characteristics, and 2) Transfer characteristics. The output characteristics are the drain current as a function of applied source-drain voltage at a constant gate potential. The transfer characteristics are the drain current as a function of gate potential at a constant source-drain potential.

The theory of FET was described by Shockley in 1952.[85] Briefly, as an electrical field (E_x) must be present when current flows in $+x$ direction, this requires a potential change along the channel length. At grounded gate potential, this change in applied reverse bias (W) is linear across the channel length (L), and this operational case of an FET is called the "gradual case". The current-voltage relationship in this condition can be written as

$$I \int dx = \int g(W) dW \tag{10}$$

Where g is the conductance as a function of given reverse bias W. Say W_s and W_d are the reverse bias at source and drain end of the terminal separated by length L, this gives

$$I = \frac{1}{L} \int_{W_s}^{W_d} g(W) dW \tag{11}$$

Equation (11) can be solved and expressed in terms of a one-variable function having dimensions of current J, gate voltage V_g, and drain voltage V_d as

$$I = \left[J(V_g - V_d) - J(V_g - V_s)\right]/L \tag{12}$$

Plotting equation (12), current *vs.* drain voltage, follows **Figure 1-5a** shown below, having parallelly translated curves (only the magnitude is taken to plot the graph in the first quadrant). An important detail to note here is that equation (12) only traces the curve until W_0 (pinch-off potential). Further elongation requires the consideration of another special case. However, analytically the "constant current beyond pinch-off potential" can be understood in such a way that the increased potential amounts to the increase in the area of contact of the space-charge region. Hence, current will not increase beyond this point, and the transistor is said to be operating in the saturation region.

Transfer characteristic measurements are another essential property of FETs (**Figure 1-5b**). The mobility of the charge carriers of a channel with dimension ($L \times d$) at a constant source-drain potential (V_{SD}) and capacitance of insulator material (C_{ox}) can be deduced using the gradual channel approximation,[86,87] assuming the potential varies gradually in the channel region, as

$$\mu_e = \left.\frac{\partial I_D}{\partial V_G}\right|_{V_{SD}=constant} \frac{L}{d}\frac{1}{C_{ox}\,V_{SD}} \tag{13}$$

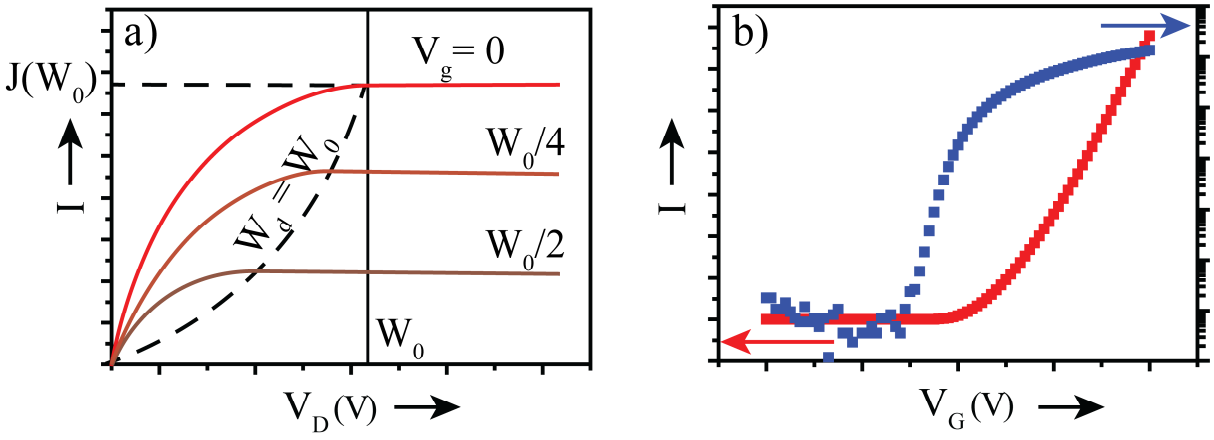

Figure 1-5 a) Variation of current with the applied drain potential. b) Transfer characteristics of a typical FET device.

1.7 Photoconductivity

FET devices use the electric field at the gate electrode to alter the conductivity of the device. A similar effect can also be induced by irradiation with photons of energy higher than the bandgap energy. These extra free charge carriers increase the conductivity of the device; it is known as the photochemical gating of the device. Various semiconductor NCs like PbS and PbSe have been explored for their photoconductivity effects.[88,89]

Semiconductor NCs have been explored to find their application as photodetectors. The coming sections briefly discuss the theory behind the process of photoexcitation. What happens when we shine photons of suitable energy on a photo-detecting device, and how are the energy levels populated and depopulated? We shall also look at the different figures of merits of a photodetector to compare them among themselves and with commercially available photodetectors.

1.7.1 Electronic Doping

A. Rose has discussed the dynamics of charge carrier formation and recombination in his book on photoconductivity.[90,91] Excitation of semiconductor material with suitable energy radiations acts similarly to the chemical doping process in terms of the addition of extra free charge carriers. This process of charge injection by light is called the electronic doping process. Laser illumination in a semiconductor excites electrons to the conduction band (CB), where they establish a thermal equilibrium between trap states (induced by defects) and the conduction band. Likewise, holes also distribute themselves in the valence band (VB). The respective charge carriers can again jump back to the CB or VB from the trap states as the thermal energy is sufficient enough to reshuffle, by definition. Additionally, charge carriers can also fall into recombination centers, which are far distant in energy, and the carriers cannot be re-excited from there. They would instead pick up the opposite charge carrier and recombine. The Fermi level for electrons E_{fn} can be defined to roughly differentiate between recombination centers and trap states as

$$n = N_c \exp\left[-\frac{|E_{fn},\ E_c|}{kT}\right] \tag{14}$$

where n is the density of excited charge carriers, N_c and E_c are the effective density of charge carriers in the conduction band and the energy of the conduction band, respectively. $|E_{fn}, E_C|$ is used to define the absolute energy interval between the two states. Similarly, E_{fp} is given by

$$p = N_v \exp\left[-\frac{|E_{fp},\ E_v|}{kT}\right] \tag{15}$$

Various states described above are shown in **Figure 1-6a**. The states lying between the hole fermi level and the valence band act as trap states for holes and likewise states lying between E_{fn} and E_C act as the trap states for electrons. The states between the two Fermi levels serve as the recombination centers. With increasing laser excitation, the two Fermi levels move apart from each other (as the population of states describes the fermi level position), leaving the states below, as recombination centers which were acting as trap states under low excitation (**Figure 1-6b**).

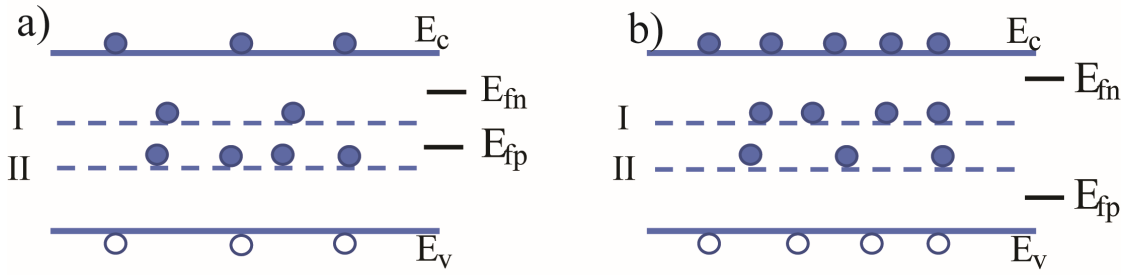

Figure 1-6 Electronic doping a) low excitation and b) intermediate excitation.

Electronic doping is a simple concept that can be used to understand the complex dependence of current on laser power and also helps to understand the infrared quenching of photodetectors.

1.7.2 Dependence of Photocurrent on Excitation Level

The photocurrent dependence on the photoexcitation level $I_{ph} \propto P^n$ is somewhat complicated, as the power exponent (n) varies between 0.5 to unity or the sublinear dependence, which is to be expected. Whereas in some cases, the power exponent goes over unity or the photocurrent shows supralinear dependence on laser power.

1.7.2.1 Sublinear Dependence

As described above, with increasing doping level, the Fermi level for electrons and holes (E_{fn}, E_{fp}) moves towards their respective bands, leaving the states which were acting as trap states before as recombination centers. To a good estimate, the density of empty recombination states (p_r) is equal to the trap states (N_t) lying between the original Fermi level (E_f) and the steady-state fermi level for electrons (E_{fn}). Analytically, the power exponent $n \leq 1$ refers to the decrease in the lifetime of electrons, which will indeed be the case as p_r states increases. Mathematically, assuming $n_r \gg p_r$ and capture cross-section $s_n \ll s_p$ with a continuous distribution of trap state, it is

$$p_r = \int_{E_f}^{E_{fn}} A\, exp\left[-\frac{|E_c, E_t|}{kT_1}\right] dE \tag{16}$$

Solving the above integral for n using the electronic doping effects induced by laser excitation gives:

$$n = \left[\frac{f N_c^{T/T_1}}{kT_1 A v s_n}\right]^{T_1/(T+T_1)} \tag{17}$$

T_1 is the characteristic temperature greater than T. Hence, the exponent varies between 0.5 to unity.

1.7.2.2 Supralinear Dependence

An exponent greater than unity cannot be accounted for by using only “one class” of states, meaning the same capture cross-sectional area of states for electrons and holes. To understand the supralinear behavior of a photoconductor, we first need to take a look at the sensitization of a photoconductor. A typical CdS photoconductor in itself has a lifetime of electron and holes of 10^{-6} and 10^{-8} s, respectively, and it is seen as a relatively insensitive photoconductor. The sensitivity of such a photoconductor can be increased by adding another class of recombination states in the system, i.e., recombination states that have different capture cross sections for electrons and holes. These additional states will increase the lifetime of one

type of charge carrier and, at the same time, decrease the lifetime of another carrier. Hence the sensitivity of the photoconductor will be increased. This process is called sensitization.

Supralinear behavior of a photodetector at low light illumination can be understood using the concept of electronic doping and sensitization. Let us assume a photoconductor with two classes of states where class I has the same capture cross-section for electrons and holes, whereas class II has a different cross-section for electrons and holes. The photoconductor should also have steady-state Fermi levels embracing only one type of class of the states (here class I), as shown by **Figure 1-7a**. When the light intensity increases, the two steady-state fermi levels start to move apart and embrace the class II states, as represented in **Figure 1-7b**. Hence, the class II states now start to act as the recombination centers having higher cross-sections for one type of charge carrier (say holes). Such a condition will sensitize the photodetector by capturing one type of charge carrier (holes in this case), thus leading to the power dependence greater than unity.

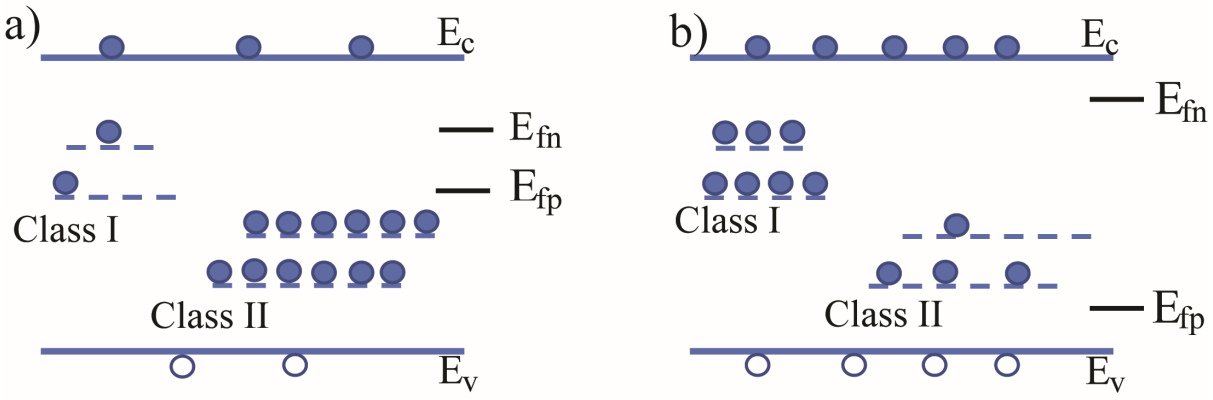

Figure 1-7 Schematic for supralinearity model a) weak illumination b) intermediate illumination.

Another factor that also plays a role in the shift of steady-states Fermi levels of electrons and holes is the temperature. The temperature has an inverse effect on electronic doping, *i.e.,* turns a sensitive photoconductor to an insensitive one. A similar effect can also be generated by shining infrared light as generated by increasing temperature. Thus, the interplay between these two factors can be used to tune the sensitivity of the photoconductor.

1.7.3 Figure of Merits of Photodetectors

The photocurrent flowing through any semiconductor is defined as the number of excess charge carriers flowing per absorbed light photon.[69,92]

$$i_{ph} = \eta e N_\lambda G_i \tag{18}$$

Here η is the quantum efficiency, e is the unit charge, N_λ is the number of photons of wavelength λ absorbed per unit time and G_i is the internal photoconductive gain. $G_i = {}^{\tau}/_{T_t}$ is given by the number of cycles a charge carrier completes before recombination. Gain can be engineered by manipulating the lifetime (τ) and the transit time (T_t). The former parameter is dependent on the trap states, whereas the latter depends on the geometry of the device and the material properties.

$$R_i(f, \lambda) = \frac{i_{ph}}{P_{in}} \tag{19}$$

Responsivity or sensitivity is defined as the photocurrent produced per unit input power (P_{in}). Responsivity is a function of modulation frequency f, and wavelength of the photon. For IR photodetectors, the responsivity typically increases with the increasing wavelength of the light and drops off to zero after a peak below the material's band-edge. In contrast, for NC based devices, it usually follows the absorption profile behavior.

$$D^*(f, \lambda) = \frac{R_i \sqrt{A\Delta f}}{i_n} \tag{20}$$

The area independent figure of merit of a photodetector is the specific detectivity (D^*) as given in equation (20). Where A is the area of the detector. Detectivity is measured in Jones ($1\ Jones\ = 1\ cm\ Hz^{1/2}\ W^{-1}$).

Response time or time constant (τ) is defined as the time taken by the photodetector to reach $(1 - e^{-1}) \approx 63\%$ of the steady-state photocurrent in responding to an optical signal. The response time is dependent on the frequency of modulation of the optical signal. For low modulation frequencies, the photodetector will be able to reach the maximum current and then fall to the dark current. Increasing the modulating frequency will give less and less time $(1/2t)$, and eventually, the photodetector's maximum current will not be reached. The modulating frequency at which the photocurrent reduced to $\left({}^{1}/_{\sqrt{2}}\right) \sim 0.707$ times the peak value is defined

as the cut-off frequency or 3dB bandwidth of the photodetector. In the same scenario, the rise time and decay time of a photodetector is defined as the time taken to reach from 10% to 90% of the maximum steady-state current upon illumination of the pulsed optical signal. It should be noted that the rise and decay time of a photodetector can be different and should be considered in determining the bandwidth.

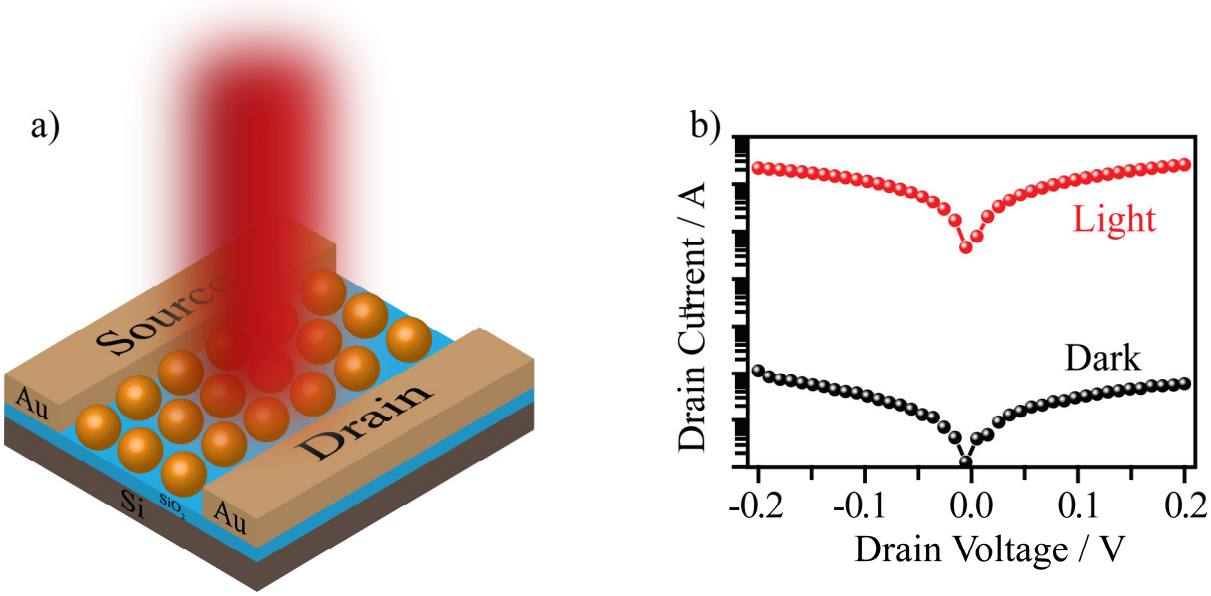

Figure 1-8 a) Schematic drawing to show a photodetector and b) typical response of such a device under the illuminated and dark state.

Specifically for NC-based photodetectors, it is also worth mentioning that a mere increase of the charge carrier concentration under light illumination is not widely assumed to be the cause of observed change in the photoconductivity. It is observed that light illumination easily increases the conductivity of NCs films over 2 to 3 orders of magnitude even under low illuminations, which barely generates single excitons per NCs.[22,88,93] These findings led Shabaev *et al.* to found out that the increased free charge carriers solely are unable to contribute to the changed conductance and suggest that the mobility of free carriers increases under the optical illumination.[94] The free carriers in dark conditions have a large energy barrier to overcome to tunnel to the next NCs. However, such boundary condition does not exist in an illuminated state as the Auger recombination is more probable than the radiative recombination in NCs. The energy released by Auger recombination can excite the nearby electrons residing in the conduction band, forming a band that has almost no energy barrier to overcome, making a band-like transport possible in such devices.

1.8 Self-Assembly of Nanocrystals

Self-assembly is a process of forming an ordered structure from the covalently non-bonded individual particles due to weak forces like van der-Waals forces or hydrogen bonding. Ordering of particles requires uniform shape and distribution. NCs synthesized with narrow size distribution can assemble themselves in an ordered superlattice when subject to a suitable environment such as evaporation of the solvent. Semiconductor and metallic NCs of various shapes and sizes have been self-assembled in literature.[95] Such a mesocrystalline structure of NC assembly could lead to new properties that are not exhibited by disordered arrays of NC, e.g., orientational ordering for fluorescent properties.[96] Ordered NC assemblies are also expected to have higher mobility than their disordered array. However, as synthesized NCs have organic surfactant layers of a few nanometer-size, which plays a crucial role in their self-assembly, but also acts as an energy barrier. Therefore hinders electronic interactions with neighbors, and the array acts as an isolated NCs. The ultimate goal of these NCs self-assembly efforts is to have a highly ordered assembly with overlapping electronic wavefunction to allow charge transport. In these terms, only short-range conductive mesocrystalline assemblies are possible until now.

1.8.1 Self-Assembly Preparation Methods

Nanoparticles are stabilized in solution as long as the pair potential is predominantly repulsive. Tethering ligands stabilize NCs due to steric interactions (organic surfactants or neutral polymers) or electrostatic repulsion (charged inorganic ligands). These ligands provide complimentary solubility in polar or in non-polar solvents. Aggregation can be induced, *e.g.,* by evaporation of the solvent, the addition of non-solvent, freezing the solvent, or by cross-linking the ligand matrix. Aggregation of NCs from solution changes the overall repulsive pair potential to attractive to allow the formation of assembled superlattices.

Self-assembly of NCs can be prepared by slow evaporation of the solvent, allowing the NCs to give sufficient time to arrange themselves in an ordered array. Rapid evaporation of solvent usually results in disordered or gel-like structure formation. The evaporation based self-assembly results in thin films at the end of evaporation when the NCs find themselves in highly concentrated environments. Self-assembly prepared using solvent destabilization methods usually results in platelet, polyhedral, or sphere-like structure, not like a thin film. This method

exploits the presence of attractive interaction between adjacent NCs, especially when the solvent mixing is unfavorable, promoting flocculation. For an organic ligand stabilized system, increasing the solvent polarity will push the formation of bundles of ligands packed in as predicted by molecular dynamic simulation and observed by vibrational spectroscopy to reduce the contact of ligands with the non-solvent.[97,98] Such bundles are more probable for longer saturated hydrocarbon chain ligands (C_{12}–C_{18}) tethered on the surface of larger NCs. Whereas in the case of evaporation-based self-assemblies, the ligand shell swells in the presence of the solvent molecules before NCs are initially crowded. As a result, non-solvent based assemblies have $\sim 25\%$ less nearest neighboring distance.[99] Another comparatively less used method of self-assembly is gravitational sedimentation. Thermal motion of defined particle size will be affected by the gravitational force, so for a larger enough particle $100-1000\,nm$ (equating thermal motion, $k_B T$ to gravitational potential energy mgd required to raise a particle of mass m by its own diameter d in earth gravity) or high-density containing elements, gravitationally assisted self-assembly of NCs is possible.[100] However, NCs studied for superlattice are usually well below the estimated range of size.

Self-assembly is a quite delicate process and depends on various factors like temperature, pressure, choice of starting material, solvent, interface type (solid or liquid), thermodynamic (facet energy, time given to assemble), and kinetic factors (nucleation sites, impurities present in the system).

1.8.2 Characterization of Nanocrystal Superlattices

Characterization of NCs assembly requires intensive instrumentation and analysis. Superlattice of NCs may be characterized in real space using a sophisticated electron microscopy technique and in reciprocal space using small-angle X-ray scattering by making use of synchrotron radiation.

In transmission electron microscopy (TEM), a high energy beam of focused electrons penetrates the thin film of NCs assembly and hits the detector. The signal generated by the detector is fed to the software, which produces a digital micrograph of that specimen. TEM generates a 2-D projection of a 3-D object, which can sometimes be hard to analyze from a single projection. To work around the problem, a TEM can look at multiple facets of the object. By rotating the sample holder, analyzing these projections can generate a tomographic view of

the object.[101] A highly magnified image provides localized information about the structure of any object. To get a statistical overview of NC assemblies, multiple 2-D images should be taken and analyzed using fast Fourier transformation (FFT) provided by image processing software. The FFT of any periodic array in real space generates spots in inverse space, each of which corresponds to a lattice spacing in real space. This same information can also be provided by electron diffraction of a periodic array of NCs. These methods are also used to distinguish very similar looking real space images. Electron microscopy (EM) is generally performed *ex-situ* on a conducting material and requires samples to be kept in a vacuum. Carbon-containing insulating organic ligands present on the surface of NCs are often undetected and get charged during the measurement, obstructing the image capturing of the instrument. Also, the contrast of an EM micrograph depends on the interaction of the electron beam with the material. Therefore, heavy atoms provide better contrast, thereby providing a clearer image. Usually, EM characterization can only be performed at the final stage of the assembly process (after drying of the sample), often leaving out the kinetic understanding of the phenomena. However, recently liquid cell TEM techniques have been developed to analyze *in-situ* processes as well.[102,103] EM in scanning mode using secondary and backscattered electrons also provides relevant information about the surface morphology of the self-assembled NCs films. Thus, electron microscopy offers more in-depth insights into the self-assembly process of NCs.

Another powerful tool for the study of self-assembly is small-angle X-ray scattering (SAXS). X-rays can penetrate deep inside any material, thereby making it a prominent tool to determine the internal structure of the system. X-ray diffraction (XRD) has long been used in material and biological science to determine the internal structure of a system, *e.g.,* for studying crystalline structures or the human skeleton. SAXS essentially works on the same diffraction principle as XRD. However, this technique requires a high brilliance source of X-ray incident at a very low angle (0.1–10°) on the sample allowing observation of nanometer-scale spatial patterns of the material. If the incident X-ray beam hits the sample at an angle below the critical angle (grazing-incidence small-angle X-ray scattering, GISAXS), it experiences total external reflection. Only the evanescent component of X-ray penetrates inside the material allowing to determine structural features of a few nanometer thick film material. X-ray scattering provides reciprocal or Q-space transformation of a much larger real space lattice, thereby providing an excellent statistical overview with intricate structure details. The scattering wave vector ($\vec{Q}$)

and the phase difference ($\Delta\,\phi$) of the wave vector ($\vec{k}$) are defined for an idealized scattering event (see **Figure 1-9**) in far-field approximation as

$$Q = \left|\vec{Q}\right| = k_f - k_i. \tag{21}$$

The magnitude of the scattering vector in terms of the scattering angle is given by

$$Q = \frac{4\pi}{\lambda} sin\theta \tag{22}$$

and the phase difference between the two singly scattering wave vector is

$$\Delta\phi = 2\pi \cdot \left(\frac{\Delta s_2 - \Delta s_1}{\lambda}\right) = k_f \cdot r - k_i \cdot r = Q \cdot r \tag{23}$$

Using the above relation in equation (23)(27) and the Bragg's relation ($n\lambda = 2dsin\theta$), the interparticle distance can be correlated to the coreelation length as

$$Q = \frac{2\pi}{d}. \tag{24}$$

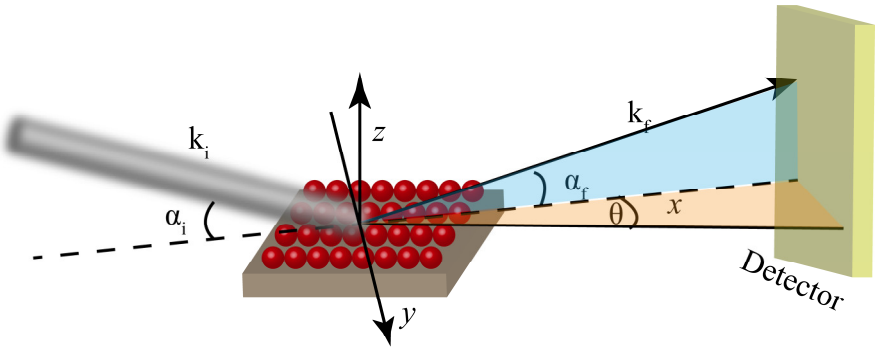

Figure 1-9 Schematic illustrating the geometry of the grazing-incidence small-angle X-ray scattering.

A limitation of SAXS is that the size of the studied object must be comparable to the incident wavelength since the technique relies on interference effects. Another one is that small-angle scattering only considers single elastic scattering events. Any inelastic or multiple scattering information will be lost. So thin film materials are well suited for this technique. The

finite detector area and coherence volume of the sample also need to be considered. Despite these limitations, small-angle scattering is used to determine the structure and study the intermediate steps taken to reach the final assembly structure. These real-time monitoring capabilities, along with parameters such as temperature and lateral pressure influence, helps to increase our understanding of the physics behind self-assembly.

2 Material and Methods

2.1 CdSe Nanocrystals Synthesis

The synthesis of CdSe NCs was adapted from a well-established procedure.[62,104] Chemicals used in the synthesis were cadmium oxide (CdO, 99.99%, Aldrich), oleic acid (OA, 90%, Aldrich), trioctylphosphine (TOP, 97%, Abcr), trioctylphosphine oxide (TOPO, 99%, Aldrich), hexadecylamine (HDA, 90%, Aldrich), 1-octadecene (ODE, 90%, Acros Organics), selenium pellet (Se, 99.999%, Aldrich), ammonium iodide (99.999%, Aldrich), N-methylformamide (NMF, 99%, Aldrich), hexane (Extra Dry, 96%, Acros Organics), ethanol (Extra Dry, 99.5%, Acros Organics), acetone (Extra Dry, 99.8%, Acros Organics), dimethyl sulfoxide (DMSO, 99.7%, Acros Organics), and acetonitrile (Extra Dry, 99.9%, Acros Organics). All chemicals were used as obtained from their respective source without further purification. Synthesis of NCs was carried out in a controlled, oxygen, and moisture-free atmosphere, provided by a Schlenk line. The glasswares were cleaned thoroughly with the base bath solution and then rinsing with soap water and deionized water several times.

For the wurtzite, CdSe NCs synthesis, 176.7 mg CdO, 8 g TOPO, 8 g HDA, 2.2 mL OA, and 45.8 mL ODE were taken into a three-neck round-bottom flask. The mixture was kept under vacuum for 2 h ($\sim 10^{-2}$ mbar). Then the mixture was heated in a nitrogen atmosphere at 300 °C until the solution became clear. The solution was then cooled down to 275 °C and kept for 30 min. In another glass vial, 1 M TOPSe was prepared by heating a mixture of 130 mg of Se pellets in 1.6 mL of TOP at 120 °C with constant stirring. The thus prepared TOPSe solution was added to the reaction mixture together with 6.4 mL of TOP and 8.0 mL of ODE. Then the entire mixture was heated at 280 °C for 25 min. The reaction was quenched by submerging the flask in a water tank. Then the reaction mixture was transferred to a nitrogen-filled glove-box. For purification, the reaction mixture was divided into five parts and precipitated with ethanol and centrifuged at 4000 rpm. The above step was repeated twice with acetone and ethanol, and the precipitate was dispersed in toluene. Finally, the NCs were purified by adding methanol, and the CdSe NCs were dispersed in hexane.

Synthesis of zinc-blende CdSe NCs was taken from literature.[105] Briefly 22.5 mg of CdO, 80 mg myristic acid were taken in 5 mL of ODE in a three-neck round bottom flask. The mixture was kept under vacuum for 2 h at 10^{-2} mbar. For dissolution, the mixture was heated

to 240 °C for 5 min and then cooled down to 60 C for injection of 1 mL cadmium acetate and 19 mg of SeO2 in 12 mL ODE. After the addition, the temperature was again raised to 240 °C, and 3 mL of 1:2 OA/ODE mixture was also added. The reaction was quenched after 1 h by dipping the reaction flask into water. The NCs were purified in a nitrogen-filled glove box using toluene-acetone and toluene-methanol solvent-antisolvent combination. Thus obtained NCs were further washed with DCM-ethanol mixture, and finally, the oily residue was washed with acetone and centrifuged at 12000 rpm for 10 min. The NCs were then dispersed in hexane for further use.

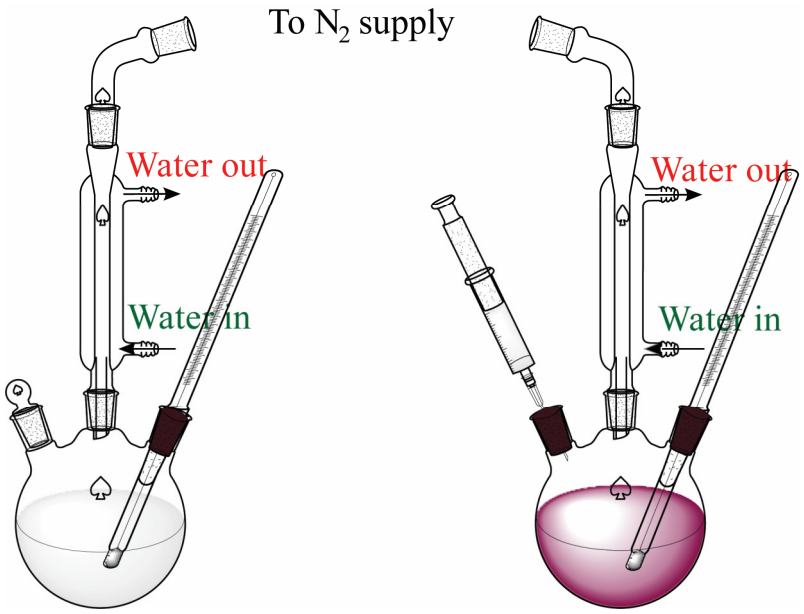

Figure 2-1 Schematic representation of the reaction assembly for the synthesis of CdSe NCs.

2.2 Iodide Ligand Exchange

Long-chain insulating ligands have an end to end length of approx. 2.5 nm hampering the electronic coupling of the neighboring NCs in the solid-state. This ligand sphere is replaced with Iodide ligand to enhance the transport properties of NCs thin film.

The ligand-exchange[62,104] was performed in a nitrogen-filled glovebox. 300 µL of 1 M NH_4I solution in NMF diluted with adding 2.7 mL of acetone was taken in a vial. CdSe NCs (5 mL) having a concentration of ~10 mg/mL in hexane was added to the above vial and stirred continuously until the hexane layer became completely colorless. The aggregate was centrifuged, the mixture was decanted, and the precipitate was washed several times with hexane to remove organic linkers left, if any. The precipitate was dissolved in 3 mL of NMF

and centrifuged using a hexane/acetone (1/2) mixture and dissolved in NMF. These NCs were used in further ligand exchange with OSC and device preparations.

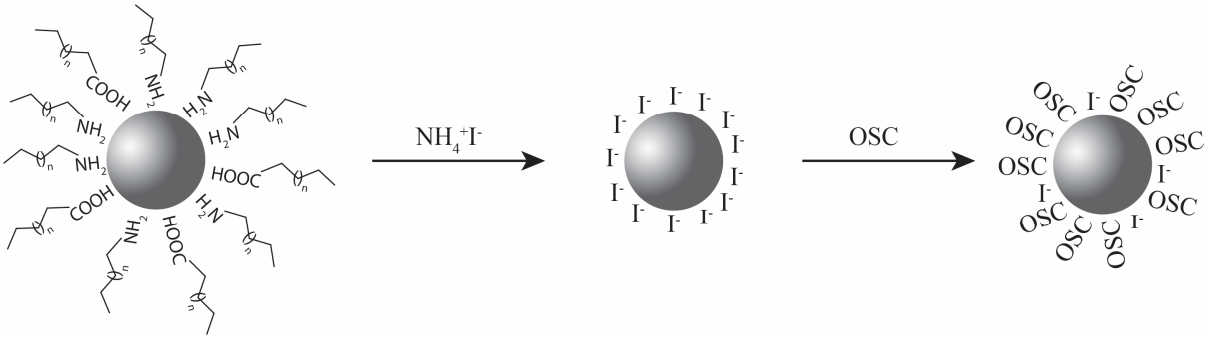

Figure 2-2 Iodide ligand exchange reaction and subsequent exchange with OSC.

2.3 Device Preparation

A commercially available bottom-gate, bottom-contact transistor substrate (n-doped silicon ($n = 3 \times 10^{17}\ cm^{-3}$) with 230 nm thermal oxide as a dielectric layer from Fraunhofer Institute for Photonic Microsystems, Dresden, Germany) with interdigitated Au electrodes of 10 mm width and varying channel lengths ($2.5, 5, 10, \& 20\ \mu m$) was used for the preparation of the FETs. In a typical film preparation, CdSe/I⁻ NCs (~60−100 mg/mL) were spin-coated onto the substrate at 35 rps and dried at 80 rps. The film was annealed at 190 °C for 30 min. For devices composed of OSC exchanged particle films, a solution of CdSe/I⁻ NCs in NMF was deposited onto the FET substrate together with ~30 µL of a saturated solution of OSC in polar solvents like DMF/DMSO. The mixture was left undisturbed for a sufficient amount of time to react to form a CdSe/I⁻/OSC film, after which the remaining solvent was spun-off the substrate to leave a continuous film. The as-prepared film was washed with acetonitrile to remove excess and unbound OSC. Finally, the film was annealed at 190 °C for 30 min.

For spectroscopic analysis, thin glass cover slides were used instead of FET substrates to deposit the NC film while keeping the rest of the procedure similar.

Self-assembled thin films of NCs were prepared using a drop-casting method. For a typical self-assembled thin film preparation, CdSe NCs of roughly $10^{-6}\ M$ were deposited on a Si substrate or Si_3N_4 window supported by Si frame, and the solvent was allowed to evaporate undisturbed in a semi-closed container. For ligand exchange, on a pre-assembled & dried thin film, Zn4APc was added and left overnight and washed with acetonitrile the next day. Thus obtained dried films were used for X-ray scattering experiments.

2.4 Characterization

2.4.1 Absorption Spectroscopy

The quantum confinement effect in the CdSe NCs manifests as a blue shift of the lowest energy excitation peak in absorption spectroscopy. Absorption measurements were performed on a Cary 5000 series UV-Vis-NIR spectrophotometer. The dependence of the first excitonic peak on the size of the NCs has been empirically determined by Yu *et al.* for different cadmium based NCs.[106]

$$D = (1.66122 \times 10^{-9})\lambda^4 - (2.6575 \times 10^{-6})\lambda^3 + (1.6242 \times 10^{-3})\lambda^2 - (0.4277)\lambda + 41.57 \quad (25)$$

Here D is the size of the NCs in nm having a first excitonic maximum at $\lambda\ nm$. They also reported the dependence of the extinction coefficient (ϵ) on the size of the NCs, which was generally thought to be size-independent. The relationship is given as

$$\epsilon = 5857 \times (D)^{2.67} \quad (26)$$

This establishes the size and extinction coefficient of the particles, and by using Beer-Lambert's law, one can find out the concentration of NCs.

$$A = \epsilon c l \quad (27)$$

Here, A is the absorbance of light passing through a cuvette of length, l, having a solution of concentration, c in mol/L.

2.4.2 Raman Spectroscopy

Raman spectroscopy generally determines the vibrational state of the system. Excitation of a COIN system with monochromatic light, e.g., by a laser, results in elastic (Rayleigh scattering) and inelastic (Raman) scattering. The monochromatic light excites the molecule to a virtual state. From there, the light can either be scattered with lower energy,

called the stokes shift, or with higher energy than the incident light, called the anti-stokes shift. The later phenomena result from the interaction of light to an already excited vibrational state electron. The excited electron relaxes itself to the ground state by imparting its energy to the light photon, thereby scattering a high energy photon. Thus, Raman spectroscopy can be used for determining the vibrational fingerprint of an organic molecule.

Raman spectra presented in this thesis work were acquired using a Horiba Jobin Yvon Labram HR 800 spectrometer in the group of Prof. Dr. Frank Schreiber. The scattered light was detected by a CCD-1024 × 256-OPEN-3S9 detector. A He:Ne laser 633 & 532 nm laser excitation were used to excite the sample.

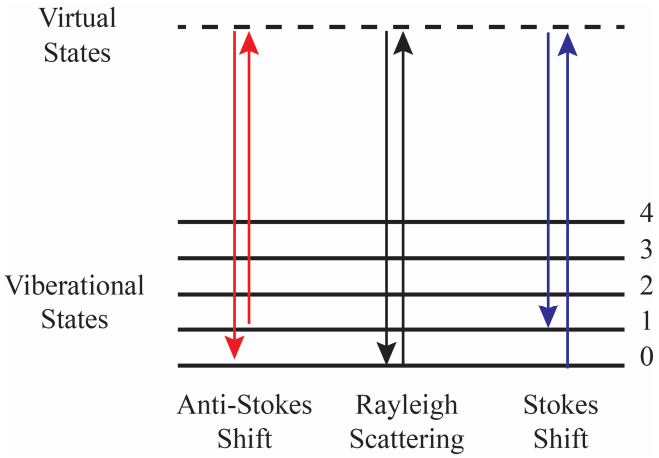

Figure 2-3 Energy levels to show different forms of light scattering from a molecule.

2.4.3 Nuclear Magnetic Resonance Spectroscopy

Nuclear magnetic resonance (NMR) spectroscopy is used to detect NMR active nuclei (having a magnetic moment of ½ or its odd multiple). Nuclei, such as ^{1}H or ^{13}C, absorb radiofrequency waves when placed in a magnetic field and resonate with different frequency radio waves depending on their chemical environment. Thus, NMR spectroscopy offers a quantitative and qualitative method to characterize such NMR active molecules. NMR spectroscopy can be used to characterize the nature of surface ligand containing olefinic hydrogens.

The NMR measurements of CdSe NCs were carried out in d8-toluene solvent using a 400 MHz Bruker instrument at the NMR facility of the Department of Chemistry, University of Tuebingen.

2.4.4 Steady-State Photoluminescence

Emission spectra are obtained when light excites a fluorophore from the ground state to the higher excited states, and the electrons and holes combine radiatively. The characteristics of the emission spectra is that a low energy light is emitted, and the loss of energy is regarded as the stokes shift. Generally, the electron-hole pair recombine radiatively from the first excited state of the molecule to the ground state, *i.e.,* the fluorescence spectrum is the mirror image of the first excitonic absorption band. However, some fluorophores like perylene also exhibit emission from the first excited state to excited vibrational states of the ground electronic state band as well. In that case, the emission spectrum is a mirror image of the entire absorption spectra. There is also an exception to the mirror image rule when there is a chemical reaction or charge transfer between the molecules in the excited state, *e.g.,* 1-hydroxypyrene-3,6,8-trisulfonate fluorescence at different pH or excimer formation in pyrenes.

Steady-state photoluminescence (SSPL) has been widely used to characterize the quality of synthesized NCs in terms of their fluorescence quantum yield. Fluorescence spectra of NCs are also dependent on the ligand sphere on the surface of the NCs as insulating organic ligands (Type I band-alignment) passivate the surface completely and confine the excitons to individual NCs, increasing the radiative recombination probability. Therefore, this technique has also been used to qualitatively monitor ligand exchange strategies, which are often needed for device applications.[62,107,108] The removal of insulating ligands around the NCs is accompanied by a decrease in the fluorescence quantum yield and introduces lower energy emission, which originates from localized surface trap states. Thus, fluorescence spectroscopy is the primary tool to not only characterize NCs qualitatively but also to give insight into the electronic structure of the NCs.

The SSPL measurements at room temperature were carried out by Jonas Hiller, a master's student in the group of Prof. Dr. Alfred Meixner, using a homebuilt inverted confocal laser scanning microscope equipped with a 488 nm TOPTICA Photonics iBeam smart diode laser.[109] The laser intensity of the gaussian smeared out laser in diffraction-limited focus was estimated to be 10^7 W/cm^2. For most SSPL experiments, this laser was operated at 30-60% of maximum power. The Laser was focused on the sample, and the emitted light was collecting using an oil immersion objective (NA = 1.25). The spectral data were recorded using an Acton SpectraPro 2300i spectrometer with a grating of 300/mm and a detector temperature of -45 °C.

Photoluminescence and scattering images were acquired by scanning the area of interest while utilizing two separate avalanche photodiodes (APDs) as detectors.

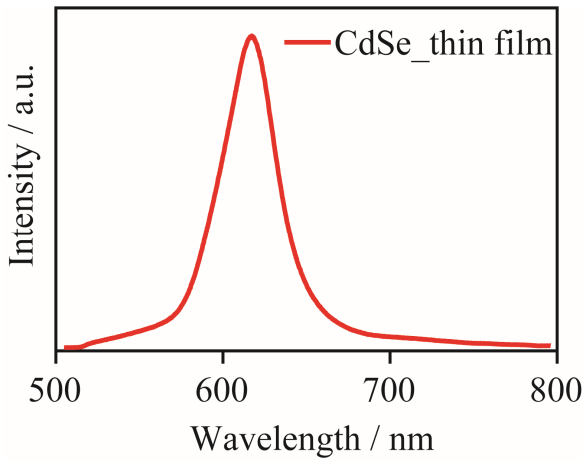

Figure 2-4 Typical fluorescence profile of CdSe NCs.

2.4.5 Low-Temperature Steady-State Photoluminescence

Room temperature SSPL from colloidal NCs sample shows broad fluorescence bands in the spectra and makes it difficult to understand the origin of the band, specifically in a hybrid system like COINs. Cooling down the sample to cryogenic temperatures freezes some of the energetic processes involved as the available energy decreases leaving the sharpening of the bands and easier deconvolution of individual peaks.

Low-temperature SSPL data were recorded by Saeed Nusrati, a doctoral student in the group of Prof. Dr. Alfred J. Meixner. A home-built confocal microscope mounted on a damped optical table was used to measure low-temperature fluorescence. The sample was mounted and scanned using a piezoelectric stage. A LakeShore temperature controller unit was used to monitor the sample temperature during the experiment. A 488 nm laser diode was used to excite the sample with a maximum power density of $7.52 \times 10^5\ \mathrm{W/cm^2}$ at the focus point, focused using a 60x air objective. The collected fluorescence signal was detected by single-photon counting avalanche photodiode. The signal was integrated for 1 s.

2.4.6 Time-Resolved Photoluminescence Spectroscopy

The intensity decay profile of a luminescence spectrum represents the lifetime of the excited state, defined as the average time spent by a molecule in the excited state before

reaching the ground-state. The lifetime of an excited state in CdSe NCs is roughly on the order of 10 ns. The lifetime of fluorophore shown in **Figure 2-5** are given by

$$\tau = \frac{1}{\Gamma + k_{nr}} \tag{28}$$

k_{nr} is the non-radiative decay constant conveniently used to sum up all the non-radiative decay processes, and Γ is the radiative decay constant. The lifetime of a fluorophore in the absence of non-radiative pathways is termed the natural lifetime, which gives the maximum lifetime as

$$\tau_n = \frac{1}{\Gamma} \tag{29}$$

The instrumentation for measuring time-resolved photoluminescence (TRPL) is significantly more complex than the SSPL measurements, and the SSPL is the averaged TRPL. So, the question arises what does this increased complexity in instruments have to reveal in terms of the molecular information? As it turns out, essential molecular information is lost during the averaging process. The fluorescence of a macromolecule is sometimes complex and shape-dependent, such that only the intensity decay profile has the shape information, which will be lost during averaging. Macromolecules can also exist in more than one conformation; thereby, the time probe of fluorescence could reveal any conformation-dependent decay profiles, *i.e.,* different decay times associated with different conformations. In the case of energy transfer, TRPL spectroscopy can reveal the arrangement of the acceptor molecules in space around the donor molecules. Fluorescence decay profiles can also reveal the nature of quenching, *i.e.,* whether quenching is due to diffusion or complex formation with ground-state molecules.

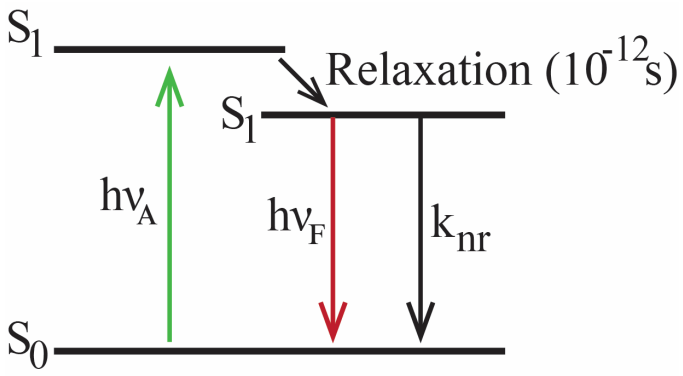

Figure 2-5 Simplified Jablonski diagram to show the meaning of lifetime. A&F subscript for absorption and fluorescence.

Quan Liu and Tim Rammler recorded TRPL measurements, both doctoral students associated with the group of Prof. Dr. Alfred J. Meixner using a home-built confocal microscope. A 488 nm laser (200 µW, 20 MHz) was used to excite the sample, and the data collection was performed by a single-photon avalanche photodiode connected to a time-correlated single-photon counting detector (TCSP, HydraHarp 400). Decay curves were fitted and analyzed using SymPhoTime 64.

2.4.7 Transient Absorption Spectroscopy

Transient absorption spectroscopy (TAS) has been a prominent tool to determine the excited state of a fluorophore. TAS probes the short-lived ultrafast processes and gives information about the energy transfer process occurring in a system. A high-intensity pump pulse excites the area of interest of a sample followed by a less intense probe pulse with delay time τ, and a differential absorption spectrum (absorption of the molecule in excited state minus the absorption from the ground state) is calculated at variable decay times.

Samples for TAS were prepared by drop-casting on a quartz plate (Eso Optics). Dr. Jannika Lauth, a post-doctoral fellow at the Delft University of Technology, Netherlands, performed the TA experiments on a set-up described previously.[110,111] A 180 fs laser pulse, generated in a Yb:KGW oscillator of wavelength 1028 nm, was split to form the probe and pump pulse. The pump beam formed from most of the fundamental laser pulse was passed through a nonlinear frequency mixer in an optical parametric amplifier (OPA) and second harmonics generation (Light Conversion, Orpheus) to generate light in the range of 310–1500 nm. A broadband probe spectrum was generated by focusing the 1028 nm laser light onto

a sapphire (500−1500 nm) or a CaF_2 (400−600 nm) crystal by nonlinear processes. Delay times of maximum 3 ns can be obtained between the pump and probe pulse using an automatic delay stage. Both the pulses had an offset of ~8° angle on the sample hitting area. The pump pulse was dumped after the photoexcitation of the sample, while the probe pulse led to a detector fiber suitable for the probe spectrum selected (Helios, Ultrafast Systems). A generated 2-D map showed the differential absorption of the COIN sample with the wavelength.

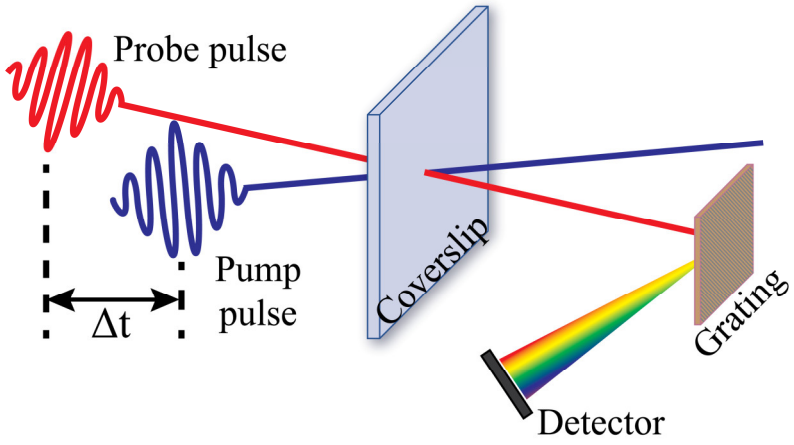

Figure 2-6 Simplified schematic of transient absorption spectroscopy.

2.4.8 Electron Microscopy

Another method for size determination of the NCs is by taking scanning electron microscopic SEM images of the sample and manually sampling many particles to get good statics for the size of the particles.

SEM samples were prepared on Si or Si/SiO_x substrate and micro-graphed by Elke Nadler from the group of Prof. Dr. Thomas Chassé and Andre Maier, a doctoral student in our group, using a HITACHI model SU8030 at 30kV equipped with three detectors. The sample preparation for NC characterization is relatively simple. However, the sample of interest can sometimes create issues with the electron beam, *e.g.,* due to organic material. The ligand material used during the synthesis of NCs, if present in excess, will reduce the signal-to-noise ratio due to charging effects. To mitigate such effect, washing the sample rigorously before inserting it into the SEM to reduce the unnecessary and unbounded ligands and grounding the conducting sample reduces the noise. An electron beam in transmission mode is also used to get a clearer micrograph of thin films.

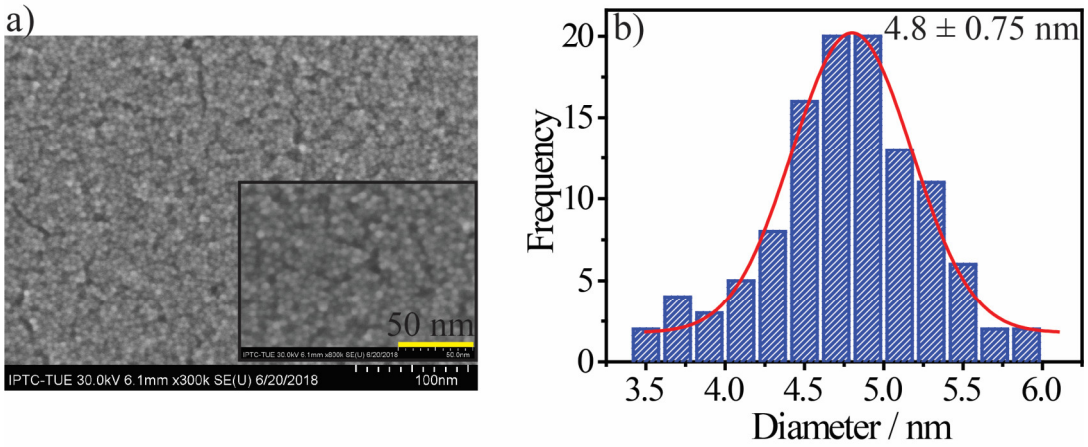

Figure 2-7 a) SEM image of CdSe NCs inset higher magnification, b) Particle size estimation, and Gaussian fit to represent the size distribution.

2.4.9 Room Temperature and Low-Temperature Electrical Measurements

To determine the FET properties of COINs at room temperature, the output characteristics and transfer characteristic properties were measured in a nitrogen-filled glove-box using a Keithley 2634B source meter. All low-temperature measurements were performed at low pressure ($10^{-5} - 10^{-6}\ mbar$) inside a cryogenic probe station CRX-6.5K (LakeShore Desert). The sample temperature was controlled by using a LakeShore temperature controller unit. The Gradual-channel approximation was used to determine the mobility at various temperatures in the linear regime, $V_{sd} \leq 5\ V$.

For optical gating of the transistor, single-mode fiber-pigtailed three laser diodes from Thorlabs having $488, 637, 847\ nm$ and operated by a CLD1010 diode controller were used. The maximum output of the three lasers was different and reported with the experimental data.

2.4.10 Time-Resolved Photocurrent Measurements

Time-resolved photocurrent measurements were performed by Christine A. Schedel, a doctoral student in our group. These measurements were performed in a vacuum chamber, maintaining a pressure of $10^{-5}\ mbar$ throughout the measurements. Thin films of hybrid material were prepared on a FET device, as described in the device preparation section. The impulse response of the device was measured by exciting the samples with 636 & $779\ nm$

pulsed lasers of pulse length $< 500\ ps$, operated by a picosecond laser driver Taiko PDL M1 from PicoQuant. These measurements were performed with $600\ \mu W$ output power and $300\ MHz$ repetition rate. The square pulse response of the films was determined by using a nanosecond diode laser driver (FSL500 from PicoQuant). The laser has a rise time of $< 0.5\ ns$ and $100\ ns$ width having $12\ mW$ laser output subjected to losses due to scattering, beam decollimation, and inefficient coupling of the fibers before hitting the sample. These measurements were performed with $300\ MHz$ repetition rate. The photo-response generated by the film was preamplified with a FEMTO HAS-Y-1–60 1 GHz high-speed amplifier and measured with a UHFLI lock-in amplifier from Zurich Instruments. The overall time resolution of the instrument is $600\ MHz$ due to the signal input of the lock-in amplifier.

2.4.11 Grazing Incidence / Small Angle X-ray Scattering

Structural characterization of CdSe NCs ordering was performed with a laboratory Xenuss 2.0 *Genix*^{3D} setup in grazing incidence mode. The X-ray radiation source used in the instrument was a Cu ULD using Cu K_α emission at 1.5406 Å wavelength having an energy of $8.04\ eV$. Two slit pairs in high resolution collimated the beam to $0.5 \times 0.5\ mm$. The scattered beam was recorded using a Pilatus 300 K detector. In house measurements were performed by Dr. Santanu Maiti, Dr. Martin Hodas, and our intern student Konstantin Tyulyunov in the group of Prof. Dr. Frank Schreiber.

Small-angle X-ray scattering measurements were performed in collaboration with the group of Prof. Dr. Ivan Vartaniants and Dr. Martin Hodas at PETRA III synchrotron DESY, Hamburg at P10, using a coherent beam of energy $13.8\ KeV$ and a GINIX setup. A nano-focussed beam having $400\ nm$ diameter achieved using KB mirrors was used to scan a sample from $10 \times 10\ \mu m^2$ to $30 \times 30 \mu m^2$ with step size ranging from $0.2\ \mu m$ to $1\ \mu m$. The beam exposure time was kept to $0.3 - 0.5\ s$ to get a good signal to noise ratio and avoiding beam damage to the sample. The scattered beam was recorded with an Eiger 4M detector positioned $370\ mm$ downstream to record a larger q-range (SAXS &WAXS patterns). An optical microscope was used to roughly position the interesting areas of the films.

Publication 1

3 Fast, Infrared-Active Optical Transistors Based on Dye-Sensitized CdSe Nanocrystals

Krishan Kumar[1], Quan Liu[1,2], Jonas Hiller[1], Christine Schedel[1], Andre Maier[1], Alfred Meixner[1,3], Kai Braun[1], Jannika Lauth[4,5], Marcus Scheele[1,3,]*

[1] Institute for Physical and Theoretical Chemistry, University of Tübingen, Auf der Morgenstelle 18, 72076 Tübingen, Germany.

[2] Charles Delaunay Institute, CNRS Light, Nanomaterials, Nanotechnologies (L2n, former "LNIO") University of Technology of Troyes, 12 rue Marie Curie – CS 42060, 10004 Troyes Cedex, France

[3] Center for Light-Matter Interaction, Sensors & Analytics LISA+, University of Tübingen, Auf der Morgenstelle 15, 72076 Tübingen, Germany

[4] Institute for Physical Chemistry and Electrochemistry, Universität Hannover, Callinstr. 3A, 30167, Hannover, Germany

[5] Cluster of Excellence PhoenixD (Photonics, Optics, and Engineering – Innovation Across Disciplines), D-30167 Hannover, Germany.

Abstract

We report an optically gated transistor composed of CdSe nanocrystals (NCs), sensitized with the dye Zinc β-tetraaminophthalocyanine for operation in the first telecom window. This device shows a high ON/OFF ratio of six orders of magnitude in the red spectral region and an unprecedented 4.5 orders of magnitude at $847\,nm$. By transient absorption spectroscopy, we reveal that this unexpected infrared sensitivity is due to electron transfer from the dye to the CdSe NCs within $5\,ps$. We show by time-resolved photocurrent measurements that this enables fast rise times during near-infrared optical gating of 74 ± 11 ns. Electronic coupling and accelerated nonradiative recombination of charge carriers at the interface between

the dye and the CdSe NCs are further corroborated by steady-state and time-resolved photoluminescence measurements. Field-effect transistor measurements indicate that the increase in photocurrent upon laser illumination is mainly due to the increase in the carrier concentration while the mobility remains unchanged. Our results illustrate that organic dyes as ligands for NCs invoke new optoelectronic functionalities, such as fast optical gating at sub-bandgap optical excitation energies.

Introduction

Optical transistors are key components in optical data communication, where they convert an incoming pulse of optical information into an electrical data output.[112,113] Light pulses in the first telecommunication window ($800-900\,nm$) are useful for specialized communication systems over short distances where the rather large dispersion at these wavelengths is irrelevant.[114] The band-edge absorption and excellent compatibility with standard CMOS technology of silicon are in principal well-suited for it to serve as the active material in an optical transistor; however its indirect bandgap and intrinsically limited optical sensitivity have moved other materials, such as GaAs, SiGe or graphene, into the spotlight.[115–117] Inorganic semiconductor nanocrystals (NCs) are considered as alternative materials for optical transistors due to their exceptionally large extinction coefficients and absorption cross sections.[118–121] In particular, InAs and PbS NCs have been successfully explored in highly sensitive photodetectors, although often with a rather slow operation time, which is not attractive for optical transistors and fast data communication.[122–128] CdSe is the technologically most mature example for this material class, and electro-optical conversion with CdSe NCs has been studied for over two decades.[129,130] Tailoring the surface chemistry has mitigated the effect of frequent surface defects, crystal grain boundaries, and barriers to charge-carrier injection in thin films of CdSe NCs, enabling charge carrier mobilities that are comparable to those in silicon.[131,132] A large tolerance for a wide range of substrates, including flexible and bendable materials, as well as photolithographic techniques to pattern CdSe NC-based devices with high fidelity render this material class increasingly competitive with established bulk inorganic semiconductors for electro-optical applications.[133,134] However, the band-edge absorption in bulk CdSe is limited to $< 730\,nm$, which is reduced further to $< 650\,nm$ for typical CdSe NCs due to quantum confinement. Below these wavelengths, CdSe NCs have demonstrated excellent optical transistor properties with ON/OFF ratios of 6 orders of

magnitude and detectivities of $> 10^{13}$ $Jones$.[135,136] However, due to the lack of absorbance at telecommunication wavelengths, the application of CdSe NCs in optical transistors is unattractive. This hampers the exploration of electro-optical communication units (optical transceivers) based entirely on CdSe NCs despite their otherwise attractive optoelectronic performance. A possible solution for this shortcoming is the design of hybrid materials, for instance by mixing CdSe NCs with graphene, black phosphorous or transition-metal dichalcogenides.[137–139] However, the relatively long lifetimes of separated charges at the interface of these hybrid materials invoke rise and fall times between 60 ms and 2.8 s, which so far prevent fast data communication.

Here, we demonstrate as to how tethering the organic dye Zinc β-tetraaminophthalocyanine (Zn4APc) to the surface of iodide-capped CdSe NCs expands the electro-optical response of thin films of this hybrid material into the first telecommunication window. At 847 nm photoexcitation, we obtain an ON/OFF ratio of 4.5 orders of magnitude and a rise time of 74 ns. With transient absorption spectroscopy (TAS), we show that the mechanism behind this action is a photoexcitation of singlet excitons in the dye, followed by charge-carrier separation and electron transfer onto the n-type NCs. Elevated electron mobilities within the network of iodide-capped CdSe NCs enable fast transfer of the photoexcited charge carriers to the terminals of an optical transistor, which merely consists of two contacts, a light source and a thin layer of the hybrid nanomaterial. This work details as to how modifying the ligand sphere of NCs with organic π-systems generates new optical properties without compromising the electronic performance of the material. This provides attractive application perspectives, for instance for optical communication technologies.

Results

Characterization of Ligand Exchange and effect on electric transconductance

Ligand exchange of 5.5 nm wurtzite CdSe NCs is monitored by optical absorption and Raman spectroscopy of thin, solid-state films in **Figure 1a,b**. As-synthesized CdSe NCs capped with a mixture of hexadecylamine (HDA) and oleic acid (OA) exhibit an excitonic transition at 621 nm (**Fig. 1a, red curve**). Surface modification with NH_4I (**Fig. 1a, blue curve**), followed by further ligand exchange with Zn4APc (**Fig. 1a, orange curve**) invokes a red shift of the excitonic transition by 2– 3 and 10 nm, respectively. We attribute this either to the change in the dielectric environment of the NCs or possibly to the reduced quantum

confinement due to improved interparticle coupling.[140,141] The appearance of two additional absorption bands at 710 and 850 nm after ligand exchange with Zn4APc is supporting evidence for a successful surface modification of the CdSe NCs.[142] For a comparison, we display the absorption spectrum of pure Zn4APc in the solid state in **Figure 1a** (**black curve**) but note that the details of the spectral absorbance are strongly influenced by the types of aggregates formed in the solid state. These are not necessarily identical in the NC/dye film. The Raman spectra in **Figure 1b** further corroborate this: HDA/OA-capped CdSe NCs (**red curve**) are weakly Raman active and mainly show the bands of the silicon substrates at 520 and 940– 985 cm^{-1}. After surface modification with NH_4I (**blue curve**), we observe strong bands at 207, 415, and 621 cm^{-1} which we interpret as the longitudinal optical phonon (1LO) and overtone (2LO, 3LO) modes of CdSe in reasonable agreement with previous reports.[143,144] In addition to these bands, the Raman spectrum of the CdSe/I^-/Zn4APc film exhibits additional bands beyond 688 cm^{-1}, which we attribute to the presence of Zn4APc upon comparison with the spectrum of pure Zn4APc (**black curve**).[145] Based on the applied amounts of NCs and dye, we gauge the ratio of Zn4APc to CdSe NCs as 4: 1 in the hybrid material.

Sayevich *et al.* have shown that initially insulating CdSe NCs capped with HDA/OA can be converted into n-type field-effect transistors upon surface modification with NH_4I and ON/OFF ratios of 5 orders of magnitude.[62] Our transconductance measurements of the CdSe/I^- NC thin films in **Figure 1c** confirm these properties. Although we were not successful in fabricating similar transistors by direct ligand exchange of HDA/OA-capped CdSe NCs with Zn4APc, we find in **Figure 1d** that a consecutive surface modification into CdSe/I^-/Zn4APc films leads to n-type transistors and an ON/OFF-ratio of 4 orders of magnitude. For a characterization of the morphologies of the film, see **Figure S5** in the Supporting Information. A comparison of **Figure 1c** with **1d** illustrates that the slightly inferior ON-OFF ratio after Zn4APc modification is mainly due to a larger threshold voltage and hysteresis. We anticipate that charge-carrier transport in CdSe/I^-/Zn4APc films most likely manifests without the aid of molecular orbitals of Zn4APc. In this scenario, the increased hysteresis in the hybrid film probably originates from burying the conductive CdSe/I^- layer within a matrix of Zn4APc.

We determine the field-effect mobilities (μ) in the dark and under 637 nm excitation by applying the gradual channel approximation and extract the charge-carrier concentration (n). On average, we find $\mu = 2.8 \times 10^{-3}\ cm^2/Vs$ and $n = 3.0 \times 10^{11}\ cm^{-3}$ in the dark which compares to $\mu = 5.2 \times 10^{-3}\ cm^2/Vs$ and $n = 2.4 \times 10^{16}\ cm^{-3}$ under 35 μW

incident optical power. For a comparison, we verified whether films of pure Zn4APc without the addition of CdSe NCs are insulating (**Figure S6**).

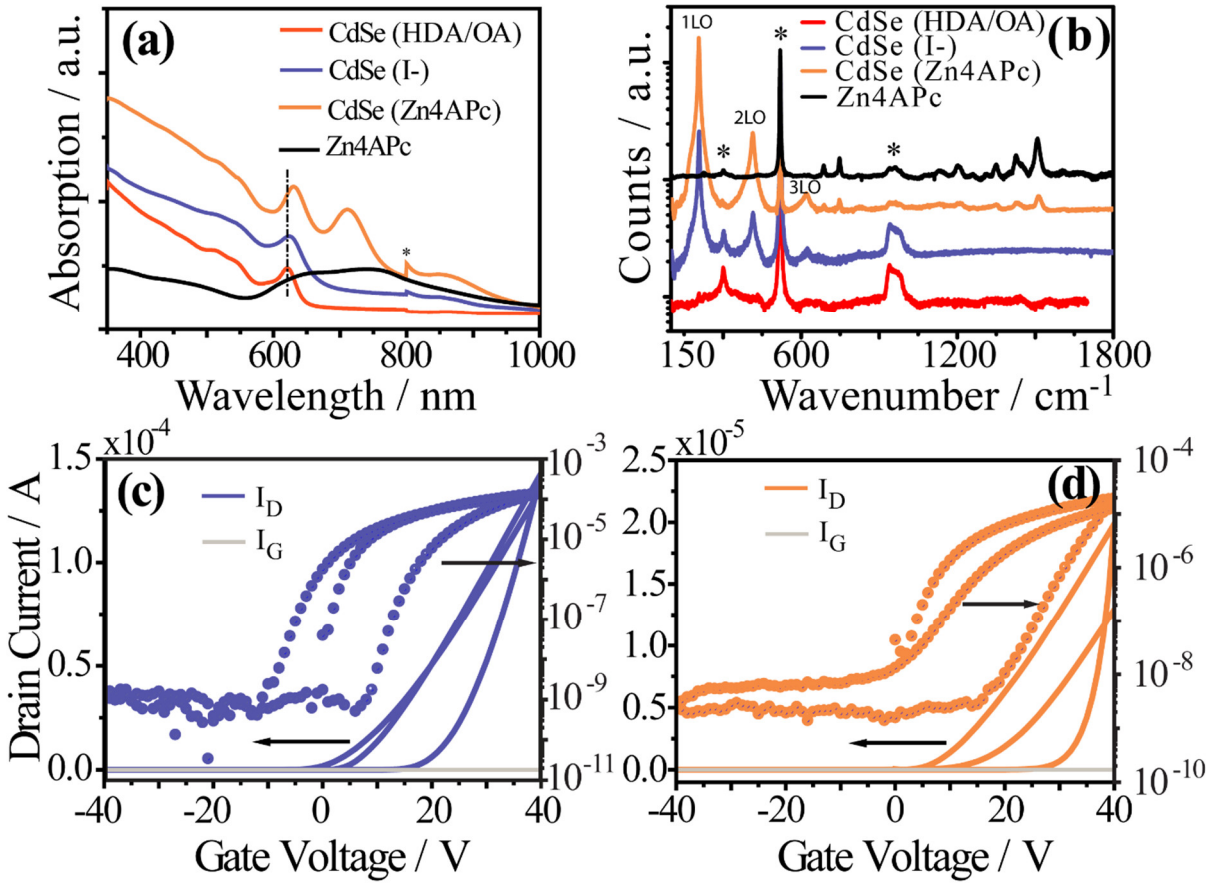

Figure 3-1 (a) Absorption profile of thin films on glass substrates of CdSe NCs with different capping ligands as well as pure Zn4APc as specified in the legend. **(b)** Raman spectra on Si/SiO_x substrates of CdSe NCs with different capping ligands as specified in the legend as well as pure Zn4APc ligand (black). Raman peaks of the Si substrate are indicated by asterisks. **(c)** Transfer characteristics of a field-effect transistor ($V_{SD} = 5\ V$) with a thin film of CdSe/I^- NCs and **(d)** with CdSe/I^-/Zn4APc. In (c) and (d), data plotted with dots are shown on a logarithmic scale, while data plotted with solid lines are displayed on a linear scale. Gray lines represent the gate leakage in both devices.

Optical Transistors

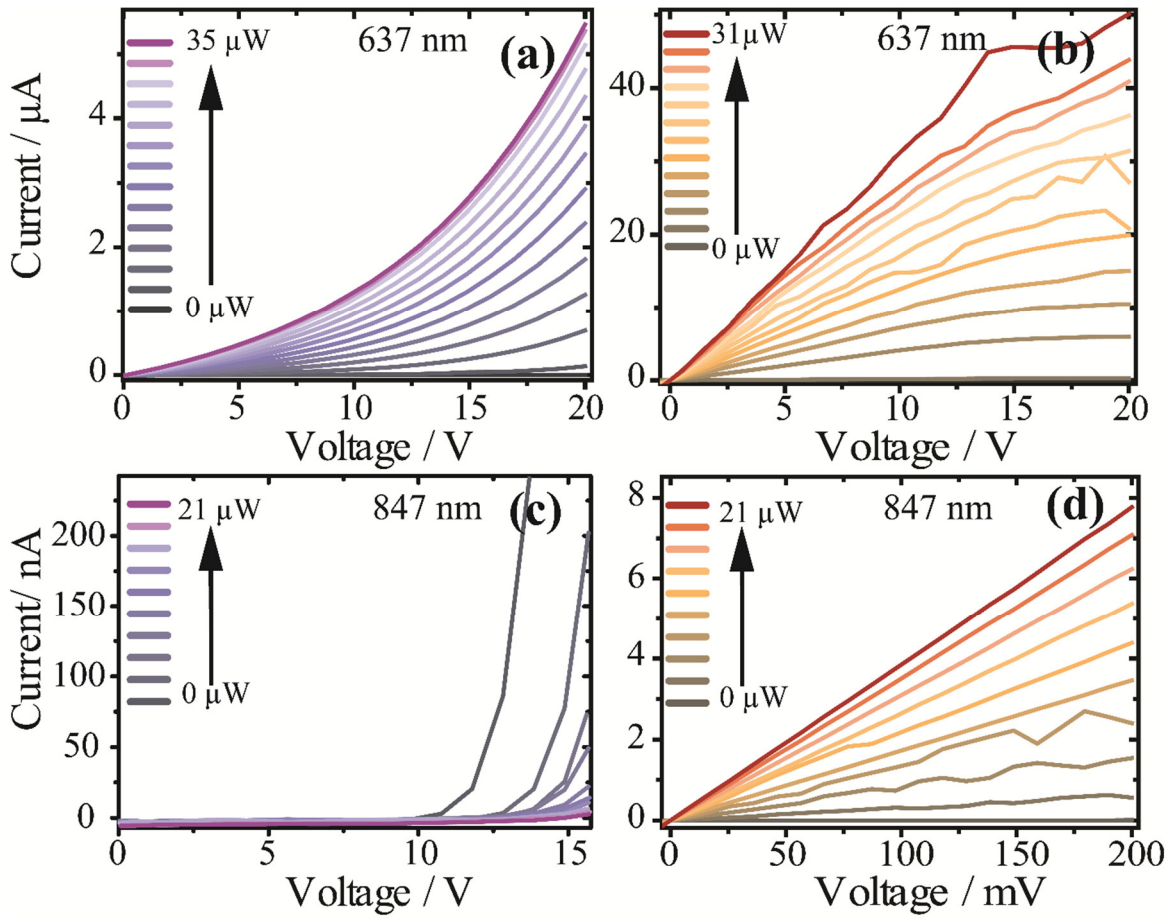

Figure 3-2 Optical gating of **(a)** CdSe/I⁻ NCs at 637 nm and an incident optical power of 0–35 µW; **(b)** CdSe/I⁻/Zn4APc NCs with 637 nm and 0–31 µW, **(c)** CdSe/I⁻ NCs with 847 nm and 0–21 µW, and **(d)** CdSe/I⁻/Zn4APc NCs with 847 nm and 0–21 µW at 0 V gate potential.

We hypothesized that rather than in field-effect transistors where the concentration of free charge carriers is modulated through a thin dielectric, the hybrid CdSe/I⁻/Zn4APc NC film may be more promising for application in optical transistors. In such a device, charge-carrier modulation is provided by an optical gate, that is, the photoexcitation is by an external light source. **Figure 2** compares the performance of the CdSe/I⁻ NC films (**Figure 2a,c**) with that of CdSe/I⁻/Zn4APc NC films (**Figure 2b,d**) under optical gating with 637 and 847 nm, respectively. Under near-resonant excitation of the CdSe NCs with 637 nm (**Figure 2a,b**), we observe a strong optical modulation of the current output for both materials. Without Zn4APc, the *I/V*-characteristics are mostly still in the linear regime (**Figure 2a**), while after additional surface functionalization with phathalocyanine, the ON-currents are 1 order of magnitude higher at an otherwise same excitation power and the *I/V*-characteristics approach the saturation regime (**Fig. 2b**). We argue that this may be the result of the additional absorption

of Zn4APc at 637 nm, resulting in a larger photocurrent and a more efficient photogeneration of free charge carriers.

A vastly different behavior of CdSe/I$^-$ vs CdSe/I$^-$/Zn4APc is observed under optical gating with 847 nm (**Fig. 2c,d**). CdSe NCs show a very weak absorption by in-gap defect states at this wavelength and, consequently, the expected photocurrent is small. Below a source–drain voltage (V_{SD}) of 10 V, there is no clear trend of the photocurrent with increasing excitation power, and the ON-current indeed largely equals the OFF-current (**Figure 2c**). For large electric fields, for example, $V_{SD} > 10\,V$, the *I/V*-characteristics show a non-ohmic behavior and an OFF-current exceeding the ON-current, that is, a negative photoeffect. Such an effect is sometimes observed at a sub-bandgap excitation of semiconductors with a significant number of shallow in-gap states.[146] Briefly, for an n-type semiconductor with in-gap states near the conduction band edge, the OFF- or dark-current results from free electrons in the conduction band donated by the shallow in-gap state. Under sub-bandgap optical excitation, electrons are excited from the valence band edge into the (empty) in-gap state. This leaves trapped electrons in the in-gap states, free electrons in the conduction band, and free holes in the valence band. If fast recombination of the free electron/hole pair is possible, the ON-current in this material will be smaller than the OFF-current, resulting in a seemingly negative photoeffect as shown in **Figure 2c**. In contrast, after functionalization with Zn4APc the photoeffect under 847 nm excitation is strongly positive (**Figure 2d**). At this wavelength, only phthalocyanine shows considerable absorption, and we suggest that Zn4APc acts as a sensitizer to activate the CdSe/I$^-$ network for photoconduction and operation as an optical transistor.

Wavelength-Dependent ON/OFF Properties

A key property of an optical transistor is its ability to distinguish between a poorly conductive OFF-state and a highly conductive ON-state. In **Figure 3**, we investigate the ON/OFF properties of CdSe/I$^-$ NCs with (**orange curve**) and without (**blue curve**) sensitization with Zn4APc under optical gating with 637 nm (**Figure 3a**) and 847 nm (**Figure 3b**) at a bias of 200 mV. At 637 nm and an incident optical power of 35 µW, the Zn4APc-sensitized CdSe/I$^-$ film outperforms the same NCs without the organic π-system with an ON/OFF-ratio of 6 orders of magnitude vs 4.6 orders of magnitude. We gauge the corresponding responsivity under these conditions as 20 mAW^{-1} with the dye and 1 mAW^{-1} without the dye. At 847 nm and 21 µW absorbed optical power, the sensitizing effect of

Zn4APc has the highest impact with an ON/OFF ratio of 4.5 orders of magnitude. The corresponding responsivity is roughly $1.5\,mAW^{-1}$. For comparison, the CdSe/I⁻ NC film without the dye exhibits an ON/OFF ratio < 2 orders of magnitude and a responsivity of only 10 µAW^{-1}. We note again that the small photosensitivity of the CdSe/I⁻ NCs is most likely due to in-gap states because of surface defects, which could be reduced even further by better passivation. This view is supported by the higher OFF-current after the first optical excitation cycle, which indicates residual charging of the film. Moreover, the observation of a negative photoeffect (**Figure 2c**) is typical for the presence of in-gap states. The ON/OFF characteristics in **Figure 3** are in good agreement with the optical gating measurements in **Figure 2** in that sensitization with Zn4APc invokes improved optical switching at 637 nm and especially 847 nm by an additional 2.5 orders of magnitude. We note that the 10^6 ON/OFF ratio at 637 nm is among the highest for this material, which is otherwise only achieved for single nanowires and rather sophisticated device architectures.[135,136,147–150] The large sensitivity at 847 nm is unprecedented for CdSe NCs due to its large bandgap and usually requires alloying, for example, with CdTe, to achieve a significant absorption in the near-infrared region.[151]

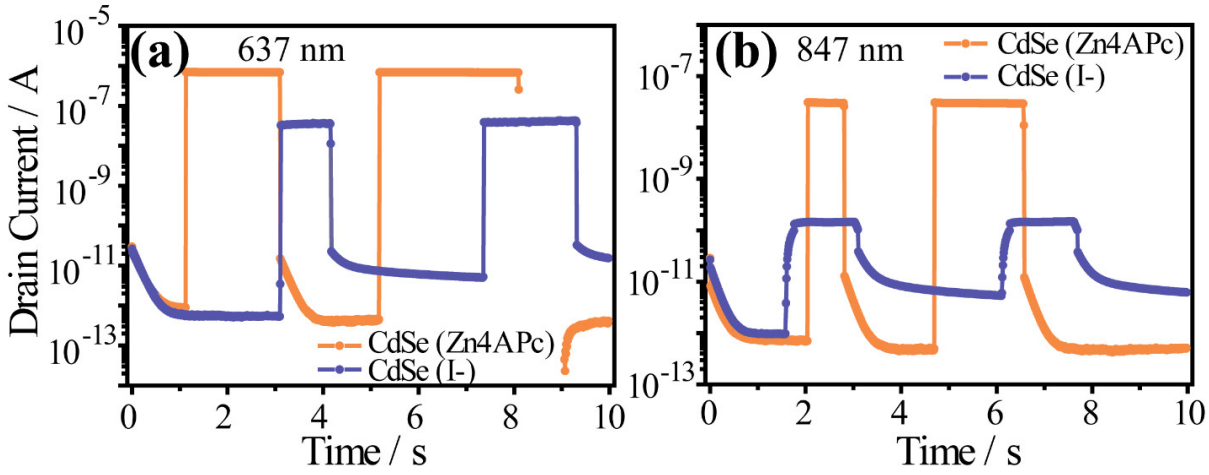

Figure 3-3 ON/OFF properties of optical transistors at $V_{sd} = 0.2\,V$ of thin films of CdSe/I⁻ NCs (blue) and CdSe/I⁻/Zn4APc NCs (orange). In **(a)**, the excitation source is provided by 35 µW of 637 nm incident light and in **(b)** by 21 µW of 847 nm light. The time resolution in both experiments is 10 ms per step, which is the integration time of the current measurement unit.

Transient Absorption Spectroscopy (TAS)

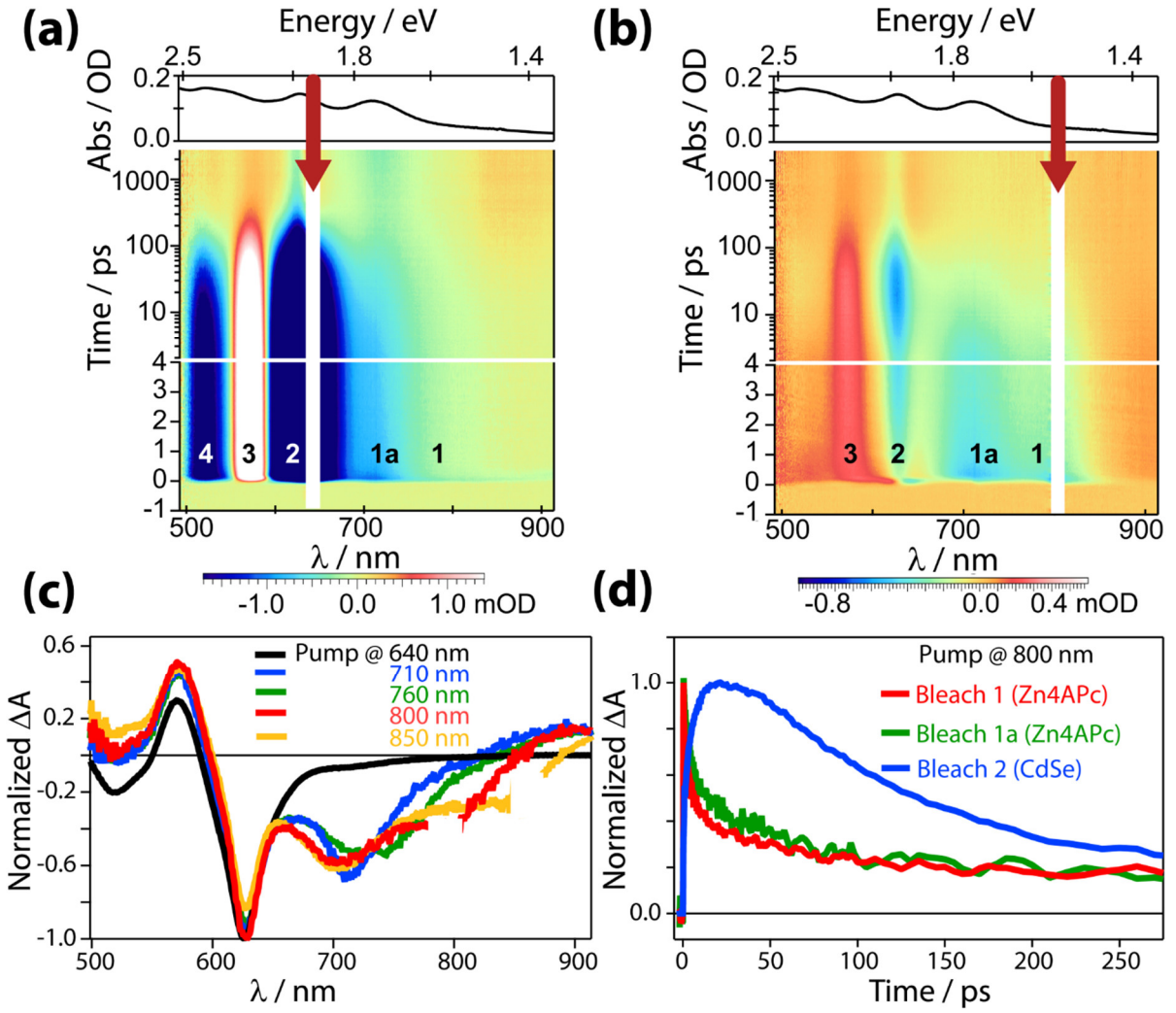

Figure 3-4 Two-dimensional-TA spectra of a CdSe/I–/Zn4APc film. (a) Near-resonant direct photoexcitation of CdSe NCs at 640 nm mainly leads to bleach features from the CdSe NCs and only a weak contribution from the Zn4APc. (b) Photoexcitation near the Zn4APc optical transition at 800 nm leads to charge transfer from the Zn4APc to the CdSe NCs visible by an indirect bleach of the CdSe transitions and visible by the rise of bleach feature 2 with the same time constants as the decay of bleach feature 1 as discussed in the text. (c) Spectral slices of the CdSe/I–/Zn4APc film photoexcited at different wavelengths and the associated increased contribution of the Zn4APc molecule at higher wavelengths and considerable Zn4APc absorption. (d) Temporal slices of band 1 (red, 785 nm), band 1a (green, 710 nm) and band 2 (blue, 621 nm) with an ultrafast rise in the first 25 ps of the measurement. The red and blue curves exhibit almost equal time constants as discussed in the text.

To understand the sensitization mechanism exerted by the organic π-system onto the NCs, we study optically thick films of CdSe/I^- cross-linked with Zn4APc by TAS. The samples are photoexcited with short laser pulses (~180 fs) of different wavelengths (640–850 nm, 1.9–

1.5 eV), and the differential change in absorption is examined by broadband probe pulses between 500 and 900 nm.[142,152] The color-coded two-dimensional (2D) TA spectrum obtained under near-resonant excitation of the CdSe NCs (pump at 640 nm or 1.94 eV) is displayed in **Figure 4a** and exhibits five bands, labeled 1, 1a, 2, 3 and 4. We attribute the weak bands 1 and 1a (710–780 nm or 1.75–1.59 eV) to the convoluted bleach of the Davydov-split highest occupied molecular orbital (HOMO)–lowest unoccupied molecular orbital (LUMO) transition of Zn4APc and note that such a splitting is often observed for aggregates of these molecules.[142,153–155] We assign the strong bleach in band 2 (625 nm or 1.96 eV) to the $1S_h$–$1S_e$ transition of the CdSe NCs. Similarly, the induced absorption band 3 (580 nm or 2.14 eV) and the bleach in band 4 (520 nm or 2.38 eV) most likely originate from a biexcitonic shift and the $1P_h$–$1P_e$ transition in the CdSe NCs as detailed previously.[156]

The TA spectrum changes significantly under near-resonant excitation of the HOMO–LUMO transition of Zn4APc (pump at 800 nm or 1.55 eV, **Figure 4b**). Bands 1 and 1a are now very prominent, supporting our assignment as the Davydov-split Q-band (the $S_0 \rightarrow S_{11}$ and $S_0 \rightarrow S_{12}$ transitions) of Zn4APc.[153] This is further detailed by the normalized line cuts at delay times of $\geq$ 7 ps in **Figure 4c** (black line: pump at 640 nm; red line: pump at 800 nm). Most importantly, we observe bands 2 and 3, although a direct excitation of these CdSe-related transitions is not possible at 800 nm. We hypothesize that a transfer of photoexcited charges from the π-system onto the NCs is responsible for this finding. To test this hypothesis, we analyze the decay of the transient bands 1/1a and 2 toward a possible time correlation in **Figure. 4d**. Indeed, we find the decay time of the bleach in band 1 matching the rise time of the bleach feature in band 2 at early times of the measurement (25 ps), before bleach 2 starts decaying again. The decay dynamics of the Zn4APc-associated bleach feature 1 and the correlated indirect bleaching of the CdSe feature 2 are fitted with a double-exponential ($\tau_1 = 330 \pm 25$ fs, $\tau_2 = 5.8 \pm 0.2$ ps and $\tau_1 = 300 \pm 34$ fs, $\tau_2 = 4.7 \pm 0.1$ ps, see **Fig. 4d**) and almost the same time constants. Note that when studying the decay dynamics of bleaches in bands 1/1a and 2 at a direct photoexcitation of the CdSe at 640 nm, the bleach feature 2 rises instantly (see **Figure S1** and, for further details, **Figure S2** and **S3**).

Time-Resolved Photocurrent Measurements

A crucial figure of merit of an optical transistor is its rise time under optical excitation with a square pulse signal. The typical time-resolved response of a CdSe/I^-/Zn4APc-based

device with an active area of 2.5 µm × 1000 µm on Si/SiO_2 is presented in **Figure 5**. We first measure the impulse response of the device toward 636 nm (**Figure 5a**) delta function laser pulses (< 500 ps pulse length, 3 MHz repetition rate) under varying bias of 0.2–10 V. Trapezoidal integration of this impulse response in the time domain yields the first half of the corresponding square pulse response and allows the determination of the rise time (**Figure 5b**, red lines). To verify this evaluation, we also measure the time-resolved photocurrent of the same device to a 635 nm square pulse with 100 ns pulse length and 3 MHz repetition rate in **Figure 5b** (gray lines). We find excellent agreement in the onset of the time-resolved photocurrent obtained with these two independent measurements for all applied biases. This suggests that the integration of the impulse response to a 779 nm delta pulse (**Figure 5c**, < 500 ps pulse length, 3 MHz repetition rate) will also allow a reliable measurement of the rise time. The rise time, defined as the time elapsed for the integrated photocurrent to rise from 10 % to 90 % of its maximum value, at 0.2 V is 45 ± 20 ns under 636 nm laser excitation and 74 ± 11 ns under 779 nm laser illumination. Increasing the applied bias to 10 V not only increases the photocurrent but also the rise times to 128 ± 80 ns and 153 ± 51 ns under 636 and 779 nm laser excitation, respectively. While the former is the expected effect of an increased electric field, the latter indicates the population and/or formation of deep traps under high-field conditions.

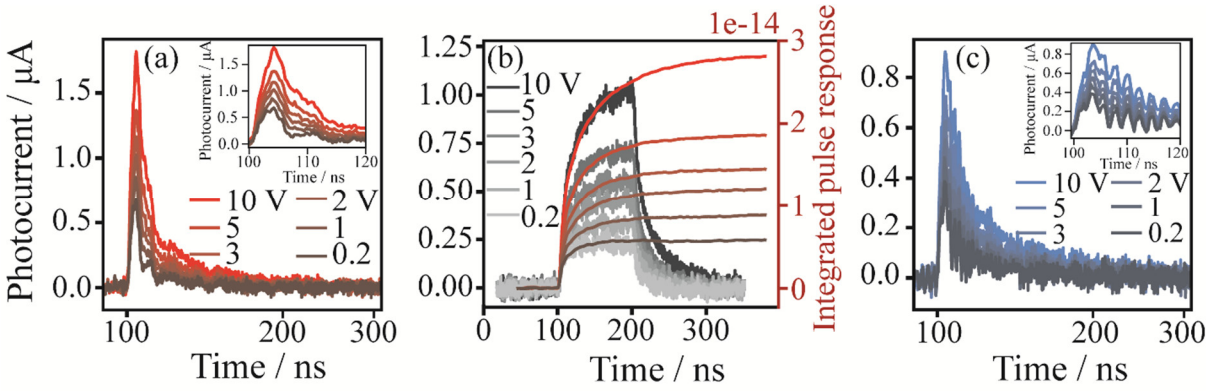

Figure 3-5 (a) Impulse photocurrent response of CdSe/I^-/Zn4APc thin films toward 636 nm delta function pulses (< 500 ps), 600 µW optical power, 3 MHz repetition rate and a varying bias of 0.2–10 V. **(b)** Trapezoidal integration of the impulse response in (a) (red lines) as well as the measured photocurrent response to a square pulsed 635 nm excitation with 100 ns pulse length (< 12 mW optical power, 3 MHz) and a varying bias of 0.2–10 V (gray lines). **(c)** Impulse photocurrent response of the same device towards 779 nm delta function pulses (< 500 ps, 600 µW, 3 MHz) and a varying bias of 0.2–10 V.

Fluorescence (Lifetime) Measurements

To investigate the radiative excited-state decay of the CdSe/I^-/Zn4APc films, we perform fluorescence lifetime measurements upon excitation with 488 nm in **Figure 6** (orange). For a comparison, we also display the fluorescence properties of thin films of CdSe/I^- NCs without Zn4APc (blue). A fluorescence spectrum of pure Zn4APc is provided in the Supporting Information. Since we observe that the fluorescence spectra and particularly the decay kinetics exhibit a substantial dependence on the substrate coverage and film thickness, we depict the same measurements for sub-monolayers (**Figure 6a,b**) as well as multilayers (roughly four layers, **Figure 6c,d**). For sub-monolayer coverage, the CdSe/I^- NC film displays a single fluorescence band with a maximum at 617 nm, while the Zn4APc-capped film shows a similar signal at 631 nm and additional broad bands at 731 nm as well as 570 nm (**Figure 6a**). We assign the bands at 617 and 631 nm, respectively, to the (red-shifted) band-edge fluorescence of the NCs and tentatively attribute the 731 nm signal to the singlet fluorescence of the organic π-system. For multilayers of the CdSe/I^-/Zn4APc films, we find peaks at 657 and 745 nm, which we attribute again to the further red-shifted CdSe band-edge and the Zn4APc singlet fluorescence, respectively (**Figure 6c**). The third band at 570 nm is still visible but substantially weakened. Multilayers of CdSe/I^- NCs show the same steady-state fluorescence as sub-monolayers.

For time-resolved fluorescence decay measurements, the fluorescence signal is integrated over the full visible regime and therefore contains contributions from the NCs as well as the organic π-system. For sub-monolayers (**Figure 6b**), all decay curves are well-fitted with biexponentials, exhibiting slow and fast decay components with time constants τ_1 and τ_2, respectively. For CdSe/I^-, we observe τ_1 = 6.1 ns and τ_2 = 1.4 ns. After cross-linking with Zn4APc, the radiative decay is significantly faster, with τ_1 = 3.1 ns and τ_2 = 0.62 ns. The time constants for the CdSe/I^- NCs are consistent with earlier results on single CdSe/CdS NCs passivated with inorganic ions in the solid state, but significantly smaller than those obtained for CdSe/I^- NCs in solution.[104,157] For multilayers, the fluorescence decay is substantially faster (**Figure 6d**). Without Zn4APc, we now find τ_1 = 5.3 ns and τ_2 = 0.86 ns, while for Zn4APc tethering, the decay is too fast to be distinguished from the instrument response function of our measurement set-up, such that no kinetic parameters can be extracted.

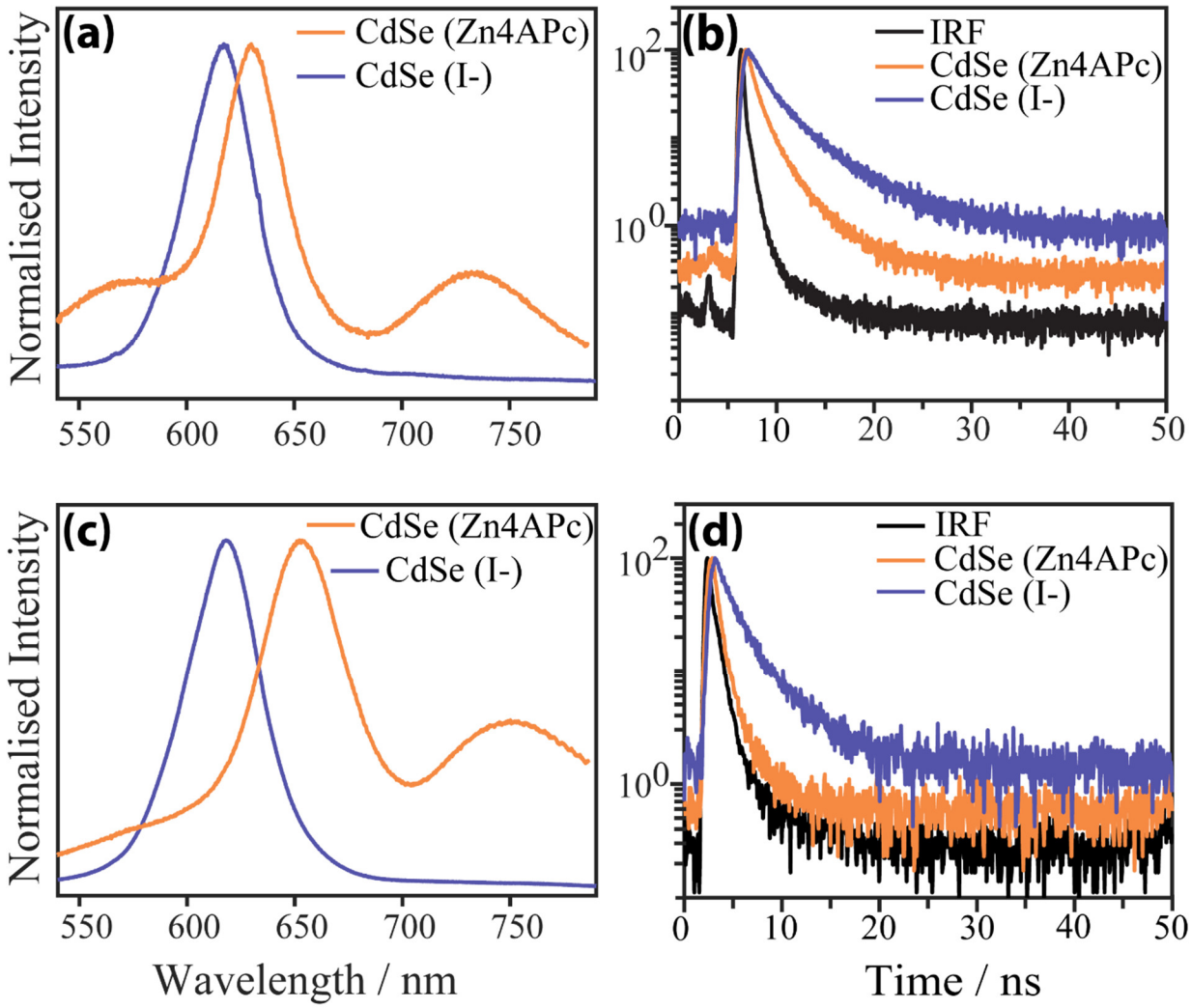

Figure 3-6 (a) Steady-state fluorescence of a (sub-)monolayer of CdSe/I⁻ NCs (purple) and CdSe/I⁻ NCs capped with Zn4APc (orange). **(b)** Time-resolved fluorescence decay of a similar (sub-)monolayer of CdSe/I⁻ NCs without (purple) and with (orange) Zn4APc. The instrument response function is depicted in black. **(c,d)** Steady-state and time-resolved fluorescence decay of multilayers of the same two materials. In all cases, the excitation wavelength is 488 nm.

Discussion

CdSe NCs are well-known for their high performance in field-effect transistors with low threshold voltage, fast switching times, printability, and lithographic processability.[132,134,158,159] Our results suggest that they are also excellently suited for application as optical transistors.[136,160,161] Large extinction coefficients ($\varepsilon = 2.7 \times 10^5\ L/mol$)[162] and small intrinsic carrier concentrations of the order of 10^{11} cm^{-3} invoke high ON/OFF ratios of up to 6 orders of magnitude for optical transistors with a relatively simple

light source. Particularly noteworthy is the ON/OFF ratio of 4.5 orders of magnitude at 847 nm illumination, which is not only unprecedented for CdSe, but also challenging to realize with other intrinsic IR absorbers, such as lead or mercury chalcogenides. Typical ON/OFF ratios for PbSe or PbS NCs are in the range of 3 orders of magnitude and often require additional electric gating because of the higher intrinsic carrier concentrations (10^{16} cm^{-3}).[152,163,164] For HgTe quantum wells with an absorption at 900 nm and an intrinsic carrier concentration of $10^{12}\ cm^{-3}$, an ON/OFF ratio of 2 orders of magnitude at room temperature was reported.[165] We explain the favorable performance of Zn4APc-functionalized CdSe NCs in this regard with the sensitization of the NCs by an organic dye ($\varepsilon(711\ nm) \approx 3.6 \times 10^4\ L/mol$)[166], enabling near-infrared absorption and harvesting of additional photons. Electronically, the dye marginally reduces the dark current and increases the threshold voltage (compare **Figure 1c/d**) toward electric gating. This indicates that charge-carrier transport proceeds mostly across a conductive network of iodide-capped NCs, including the carriers that were originally photoexcited in the organic dye. The largely identical field-effect mobilities extracted in the dark and under full optical excitation (0.0028 vs 0.0052 $cm^2/(Vs)$) demonstrate that photoexcited charge carriers use the same transport channels as in the dark. This is in contradiction to photocurrent measurements on PbS and PbSe NC films, which displayed increased mobilities under photoexcitation.[89,163,167] We note, however, that the excitation power densities in those studies were substantially smaller than in the present case (50 $\mu W/cm^2$ vs ~100 mW/cm^2).

The benefit of the dye-sensitization approach presented here is further illustrated by the favorable time-resolved response to optical gating. While the rise time of the pure CdSe/I^- film with 160 ms is slow at sub-bandgap excitation (**Figure 3b**), optical transistors made of Zn4APc-sensitized CdSe/I^- NCs are over one million times faster with 74 ± 11 ns under 779 nm excitation (**Figure 5c**). Other materials with strong absorption in this spectral regime, such as HgTe–CdS nanoplatelets or PbSe NC nanojunctions, have shown comparably slower rise times of 10 µs and 300 ns, respectively.[168,169] Recent time-resolved photocurrent measurements on lead halide perovskite photodetectors have reported response times as fast as 1.8 ns, but these were limited to excitation at 532 nm.[170] We suggest that the dye-sensitization concept outlined here may allow expansion of the spectral window for optical gating with perovskites similar to what we have demonstrated with CdSe NCs to reward even faster NIR optical transistors.

Scheme 1. Idealized Schematics of the Structural Composition and Working Mechanism of the Optical Switch Under Near-IR Excitation.[a]

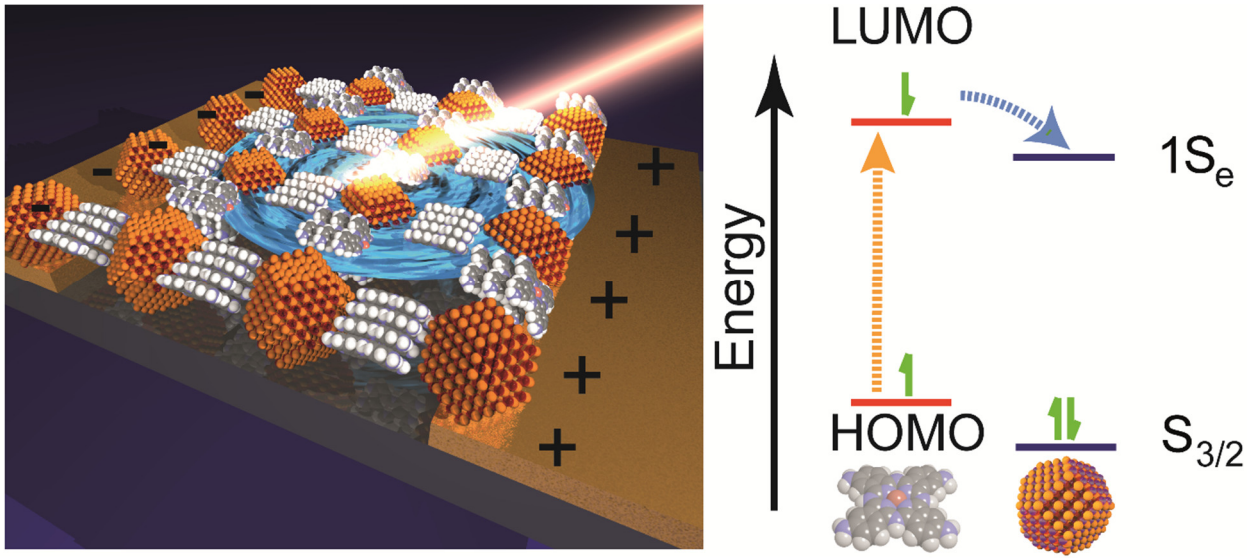

[a]Direct photoexcitation of the HOMO–LUMO transition of the organic dye is followed by electron transfer into the 1Se state of the NCs, from where the electrons are shuttled to the electrodes under a small bias.

At the heart of this concept is charge transfer from the dye to the NCs, which is evident from the transient absorption data in **Figure 4b,c** at various excitation wavelengths between 710 and 850 nm. The essentially identical time constants for the biexponential decay of the photobleach of the singlet transition of Zn4APc compared to the biexponential rise of the excitonic photobleach of CdSe are a strong hint for such a mechanism (**Figure 4d**). The slower decay/rise component as the rate-limiting step of charge transfer ($\tau \approx 5$ ps) illustrates that optical switching at this hybrid interface is many orders of magnitude faster than that in other hybrid CdSe NC-based materials.[137–139] On the other hand, resonant excitation of the NCs at 640 nm exhibits no comparable signs of charge transfer in the opposite direction (**Figure 4a**). From this, we can draw two conclusions: (I) While an unambiguous distinction between charge and energy transfer is challenging, charge transfer seems to be the more plausible mechanism here. This follows from the fact that energy transfer requires a large overlap between the absorption of the acceptor and the fluorescence of the donor. Thus, energy transfer from the NCs onto the molecule should be much more favorable than in the reverse direction; however, we only observe the latter. (II) The frontier orbital energies of Zn4APc are such that electron

transfer into the $1S_e$ state of CdSe is thermodynamically favorable. Electrochemical studies suggest that the LUMO of Zn4APc is indeed approx. 0.5 eV above the $1S_e$ state of CdSe, rendering electron transfer feasible.[171] In contrast, the HOMO of Zn4APc is positioned approx. 0.4 eV above the $1S_h$ state, which speaks against hole transfer toward the NCs. Overall, we therefore attribute the large photocurrent under 847 nm excitation of Zn4APc/CdSe NCs to the singlet absorption of Zn4APc, splitting of the exciton and transfer of electrons to CdSe, which is schematically detailed in **Scheme 1**. This view is also consistent with the finding that transient photobleaching of the excitonic transition in CdSe is predominantly caused by electrons.[172] Electrons are the majority carriers in films of iodide-capped CdSe NCs, such that they are swept quickly to the electrodes. Holes remain either trapped in the dye, recombine at the organic/inorganic interface with excess electrons in the NCs, or are shuttled (slowly) to the electrodes by hopping between adjacent dye molecules. To this end, the time-resolved fluorescence data in **Figure 6b,d** enable valuable insights into the recombination mechanism of the charge carriers. The experimental lifetime τ is correlated to the radiative and nonradiative rates, k_r and k_{nr}, as $\tau = \frac{1}{k_r + k_{nr}}$. Thus, the substantial decrease of τ upon functionalization of $CdSe/I^-$ with Zn4APc indicates an increase of either the radiative recombination or a nonradiative pathway. Since it is difficult to imagine how any of the afore-mentioned scenarios for the fate of the holes could lead to additional radiative recombination, we suspect that the shortened lifetime is due to accelerated nonradiative recombination, presumably due to trapped holes at the organic/inorganic interface and their interaction with excitons in the NCs. The same scenario could also explain the red-shifted fluorescence of $CdSe/I^-$ NC films after surface functionalization with Zn4APc: If electrons reside predominantly in the NCs and holes in the organic dye, a "type-II" radiative recombination at the organic–inorganic interface would be possible.[173] This emission should be red-shifted compared to the pure CdSe band-edge recombination, since the Zn4APc HOMO lies energetically above the CdSe $1S_h$ state. The red-shifted absorption and fluorescence (**Figures 1a and 6a, c**) support this view. In contradiction, a type-II fluorescence at a semiconductor interface is typically accompanied by a substantially increased radiative lifetime, since electrons and holes are spatially separated. Our finding of a drastically reduced lifetime does not support this scenario. However, it is also possible that a potential increase in the radiative lifetime is accompanied by an increase of nonradiative recombination with the result of an overall shorter experimental lifetime. In this context, we note that the rise time upon resonant excitation of the dye (74 ± 11 ns) is only marginally

longer compared to resonant excitation of the NCs (45 ± 20 ns). Considering that photoexcited charges in the dye need to be shuttled to the NCs before they can contribute to the photocurrent, this implies that trapping at the organic/inorganic interface in CdSe/I^-/Zn4APc is relatively short-lived.

Conclusions

Iodide-capped, n-type CdSe nanocrystals are surface-functionalized with the organic π-system Zn β-tetraaminophthalocyanine and assembled into a thin-film optical transistor. Optical gating with a 637 nm light source yields excellent current modulation by 6 orders of magnitude, near-saturation behavior, and a rise time of 45 ± 20 ns. Under near-infrared excitation, the modulation exhibits 4.5 orders of magnitude and rise times of 74 ± 11 ns, which is unprecedented for CdSe nanocrystals due to their intrinsically poor sensitivity to infrared light. We show that this is enabled by the harvesting of infrared photons by the organic dye, singlet exciton splitting, and electron transfer onto the nanocrystals with a lifetime of ~5 ps. Such dye-sensitized nanocrystals combine the well-developed electronic properties of CdSe nanocrystals with high optical sensitivity in the near-infrared region, which is attractive for application in optical transceivers operating in the first telecommunication window.

Experimental Methods

Chemicals used were cadmium oxide (CdO, 99.99%, Aldrich), oleic acid (OA, 90%, Aldrich), trioctylphosphine (TOP, 97%, Abcr), trioctylphosphine oxide (TOPO, 99%, Aldrich), hexadecylamine (HDA, 90%, Aldrich), 1-octadecene (ODE, 90%, Acros Organics), selenium pellet (Se, 99.999%, Aldrich), ammonium iodide (99.999%, Aldrich), N-methylformamide (NMF, 99%, Aldrich), hexane (Extra Dry, 96%, Acros Organics), ethanol (Extra Dry, 99.5%, Acros Organics), acetone (Extra Dry, 99.8%, Acros Organics), dimethyl sulfoxide (DMSO, 99.7%, Acros Organics), and acetonitrile (Extra Dry, 99.9%, Acros Organics). All chemicals, except those used in CdSe NC synthesis, were stored and used inside a nitrogen-filled glovebox.

CdSe NC Synthesis.

Wurtzite 5.5 nm CdSe NCs were synthesized using a previously reported literature procedure.[174] Briefly, 176.7 mg CdO, 8 g TOPO, 8 g HDA, 2.2 mL OA, and 45.8 mL ODE were weighed into a three-neck round-bottom flask and kept under vacuum for 2 h (~10−2

mbar). It was heated under a nitrogen atmosphere to 300 °C until the solution became clear. The solution was cooled down to 275 °C and kept for 30 min. In a glass vial, 1 M TOPSe was prepared by heating 130 mg of Se in 1.6 mL of TOP at 120 °C under constant stirring. Together with this TOPSe solution, 6.4 mL of TOP and 8.0 mL of ODE were added to the flask, and the temperature was increased to 280 °C. After that, the mixture was kept for about 25 min to grow CdSe NCs. The reaction was quenched by a sudden decrease in the temperature. For purification, the reaction mixture was precipitated with ethanol, centrifuged, and redispersed in hexane. For further purification, this procedure was repeated twice with acetone and ethanol, and the precipitate was redispersed in toluene in both cases. Finally, the NCs were purified by adding methanol and redispersing in hexane.

Ligand Exchange.

The ligand-exchange procedure was adopted from the literature and performed in a nitrogen-filled glovebox.[174,175] Briefly, 300 μLof1M NH4I solution and 2.7 mL of acetone were added to 5 mL of CdSe NCs (concn ∼10 mg/mL) in hexane and stirred continuously until the hexane layer became completely colorless. The aggregate was centrifuged, washed with hexane, and centrifuged again. The precipitate was dissolved in 3 mL of NMF and centrifuged using a hexane/acetone (1/2) mixture and finally dissolved in NMF. NCs prepared in this way are referred to as CdSe/I^- NCs in this manuscript.

Device Preparation.

Device fabrication was performed in a nitrogen-filled glovebox. A commercially available bottom-gate, bottom-contact transistor substrate (n-doped silicon ($n = 3 \times 10^{17}\ cm^{-3}$) with 230 nm thermal oxide, Fraunhofer Institute for Photonic Microsystems, Dresden, Germany) with interdigitated Au electrodes of 10 mm width and varying channel lengths (2.5, 5, 10, and 20 μm) was used for the preparation of the FETs. In a typical film preparation, CdSe/I^- NCs (∼60−100 mg/mL) were spin-coated onto the substrate at 35 rps and dried at 80 rps. The film was annealed at 190 °C for 30 min. For devices composed of CdSe/I^-/Zn4APc films, a solution of CdSe/I^- NCs in NMF was deposited onto the FET substrate together with ∼30 μL of a saturated Zn4APc solution in DMSO. The mixture was left undisturbed for a sufficient amount of time to react to form a CdSe/I^-/Zn4APc film, after which the remaining solvent was spun-off the substrate to leave a continuous film. The as-prepared

film was washed with acetonitrile to remove excess and unbound Zn4APc. Finally, the film was annealed at 190 °C for 30 min.

Electrical and Optical Measurements.

Electrical measurements were carried out under nitrogen by using a Keithley 2634B Source Meter. The charge-carrier mobility (μ) was extracted using the gradual channel approximation in the linear regime:

$$\mu = \left.\frac{\partial I_D}{\partial V_G}\right|_{V_{sd}} \times \frac{L}{W} \times \frac{t_{ox}}{\varepsilon_{ox} \times V_{sd}}$$

where $\left.\frac{\partial I_D}{\partial V_G}\right|_{V_{sd}}$ is the slope of the curve drain current vs gate voltage, L is the length of the channel, W is the width of the channel, t_{ox} and ε_{ox} are the thickness and permittivity of the oxide layer, respectively, and V_{sd} is the source−drain voltage applied ($\leq 5\ V$).

The carrier concentration (n) was measured as follows

$$n = \frac{\sigma}{e \times \mu}$$

where σ is the conductivity, e is an elementary charge, and μ is mobility of the charge carrier.

Photocurrent Measurements.

Photocurrent measurements were performed in a cryogenic probe station CRX-6.5K (Lake Shore Desert) at room temperature and a pressure of $5 \times 10^{-6}\ mbar$. For this, the film on the bottom-gate bottom-contact transistor substrate was transferred into the probe station under minimal exposure to air. The samples were contacted in a two-point probe fashion. Data were recorded using a 2634B SYSTEM SourceMeter from Keithley Instruments operated by the software test script processor (TSP) express. As an excitation source, single-mode fiber-pigtailed laser diodes from Thorlabs operated by a compact laser diode controller CLD1010 by Thorlabs were used: a 637 nm laser diode with a maximal output power of 70 mW and a 847 nm laser diode with a maximal output power of 30 mW. Losses to this theoretical optical power output due to scattering, inefficient coupling into the optical fiber, decollimation of the beam, etc., were determined by a calibration sample and an optical power meter to obtain the total incident optical power at the sample surface.

Transient Absorption Measurements.

Transient absorptions of thin films of CdSe/I⁻/Zn4APc NCs were studied by broadband pump-probe spectroscopy in a set-up described previously and discussed here briefly.[142,176] The samples were drop-cast on quartz plates (Eso Optics), yielding thin optically dense films of varying thicknesses. Laser pulses of $180\ fs$, generated in a Yb:KGW oscillator at $1028\ nm$, are split-off to generate a pump and a probe beam. The pump beam energy was varied by nonlinear frequency mixing in an optical parametric amplifier (OPA) and second harmonics generation (Light Conversion, Orpheus). A broadband probe spectrum was generated by focusing the $1028\ nm$ laser light onto a sapphire ($500 - 1500\ nm$) or a CaF_2 ($400 - 600\ nm$) crystal by nonlinear processes. The probe pulse can be delayed up to $3\ ns$ by an automated delay stage. The majority of the $1028\ nm$ fundamental laser beam is used as the pump pulse for photoexciting the sample (wavelengths $310 - 1500\ nm$) after nonlinear frequency mixing in an optical parametric amplifier (OPA) and second harmonics module (Light Conversion, Orpheus). The pump and the probe pulse overlap at the sample position in an ~8° angle. The pump pulse is dumped after the photoexcitation of the sample, while the probe light is led to a detector fiber suitable for the probe spectrum selected (Helios, Ultrafast Systems).

Time-Resolved Photocurrent Measurements.

Time-resolved photocurrent measurements were performed at room temperature under vacuum ($1.5 \times 10^{-5}\ mbar$) and the devices were kept under vacuum for at least $2\ h$ before starting any measurements. Pulse- response measurements were performed using a picosecond pulsed laser driver (Taiko PDL M1, PicoQuant) together with laser heads for $636\ nm$ (pulse length $<\ 500\ ps$) and $779\ nm$ (pulse length $< 500\ ps$) operation. A repetition rate of $3\ MHz$ was selected with an output power of approximately $600\ \mu W$. For the step function measurements, a nanosecond diode laser driver (FSL500, PicoQuant) with a laser rise time of $< 0.5\ ns$ in conjunction with a $635\ nm$ laser diode operated at $3\ MHz$ with a pulse width of $100\ ns$ and an average output power of $\leq 12\ mW$ was used. This laser power is subjected to further losses due to scattering, inefficient coupling into the optical fiber, decollimation of the beam, etc. The current was preamplified with a FEMTO HSA- Y-1−60 1 GHz high-speed amplifier and measured with a Zurich Instruments UHFLI lock-in amplifier with the Boxcar Averager Function, which averages the signal from 33.6 M samples. The signals were

background-corrected. The time resolution was limited to 600 MHz due to the signal input of the lock-in amplifier.

Steady-State Photoluminescence Measurements.

Steady-state photoluminescence measurements were performed using an inverted confocal microscope equipped with an oil-immersion microscope objective ($NA = 1.25$). The samples were placed in an ambient atmosphere and excited using a 488 nm (optical power on sample 1 mW) laser diode manufactured by TOPTICA iBEAM- SMART-488. The photoluminescence data were recorded using an Acton SpectraPro2300i spectrometer at a detector temperature of $-40\ °C$ and an acquisition time of 4 s.

Time-Resolved Photoluminescence Decay Measurements.

The fluorescence lifetimes of CdSe/I$^-$ and CdSe/I$^-$/Zn4APc were measured using a home-built scanning confocal microscope.[177] A 488 nm pulse laser (200 $\mu W, 20\ MHz$) illuminated the sample using a high numerical aperture ($NA = 1.46$) oil objective. The fluorescence was collected by the same objective and then sent via a beam splitter to a single-photon avalanche photodiode, which was connected to a time-correlated single-photon counting detector (TCSP, HydraHarp 400). Decay curves were fitted and analyzed by SymPhoTime 64.

ASSOCIATED CONTENT

Supporting Information.

Transients of CdSe/I$^-$/Zn4APc after 640 nm pump pulses, CdSe/I$^-$/Zn4APc after 800 nm pump pulses, and CdSe/I$^-$/Zn4APc after 710 nm pump pulses; solid-state fluorescence of a thin film of pure Zn4APc; scanning electron micrographs of typical CdSe NC films; and current/voltage transport characterization of pure Zn4APc films.

AUTHOR INFORMATION

Corresponding Author

*Email: marcus.scheele@uni-tuebingen.de

Author Contributions

This manuscript was written through contributions of all authors. All authors have given approval to the final version of the manuscript.

ACKNOWLEDGMENT

The authors acknowledge the DFG for support under Grant SCHE1905/3 and under Germany's Excellence Strategy within the Cluster of Excellence PhoenixD (EXC 2122, Project ID 390833453). The time-resolved photocurrent measurements have been funded by the European Research Council (ERC) under the European Union's Horizon 2020 research and innovation program (grant agreement No 802822).

Publication 2 *(in review)*

4 Periodic Fluorescence Variations of CdSe Quantum Dots Coupled to Aryleneethynylenes with Aggregation Induced Emission

Krishan Kumar[1], Jonas Hiller[1], Markus Bender[2], Saeed Nosrati[1], Quan Liu[1,3], Frank Wackenhut[1], Alfred J. Meixner[1,4], Kai Braun[1], Uwe H. F. Bunz[2,], Marcus Scheele[1,4,*]*

[1] Institute for Physical and Theoretical Chemistry, University of Tübingen, Auf der Morgenstelle 18, 72076 Tübingen, Germany.

[2] Organisch-Chemisches Institut and Centre for Advanced Materials, Ruprecht-Karls-Universität Heidelberg, Im Neuenheimer Feld 270, 69120 Heidelberg, Germany

[3] Charles Delaunay Institute, CNRS Light, nanomaterials, nanotechnologies (L2n, former "LNIO") University of Technology of Troyes, 12 rue Marie Curie - CS 42060, 10004 Troyes Cedex, France

[4] Center for Light-Matter Interaction, Sensors & Analytics LISA+, University of Tübingen, Auf der Morgenstelle 15, 72076 Tübingen, Germany

KEYWORDS
Quantum Dots, Organic π-Systems, Aggregation Induced Emission, Energy Transfer

Abstract

CdSe nanocrystals and aggregates of an aryleneethynylene derivative are assembled into a hybrid thin film with dual fluorescence from both fluorophores. Under continuous excitation, the nanocrystals and the molecules exhibit anti-correlated fluorescence intensity variations, which become periodic at low temperature. We attribute this to a structure-dependent aggregation induced emission of the aryleneethynylene derivative, which impacts the rate of excitation energy transfer between the molecules and nanocrystals. Energy transfer

also affects the electric transport properties of the hybrid material under optical excitation. This work highlights that combining semiconductor nanocrystals with molecular aggregates, which exhibit aggregation induced emission, can result in unprecedented emerging optical properties.

Introduction

Aggregation induced emission (AIE) refers to enhanced and often redshifted fluorescence of luminophores upon formation of aggregates from solution.[178] The prototypical example are organic π-systems with a large degree of structural twisting in the ground state, e.g. tetraphenylethylenes[179] or aryleneethynylenes[180], which exhibit high torsion angles between the central C=C or C≡C bond and the sterically demanding phenyl-substituents. Photoexcitation weakens the double or triple bond and reduces the torsion angles with the phenyl rings.[181–183] Relaxation from this state occurs via three pathways: 1) radiative recombination, 2) intramolecular motion (mostly de-twisting of the C=C or C≡C bond) or 3) photochemical reaction to an intermediate. AIE occurs if pathways 2)+3) are significantly inhibited in the aggregates due to restriction of intramolecular motion.[184] The degree of this restriction depends on the solid-state structure and, thus, on temperature-induced structural transitions.[182,185,186] These transitions may be triggered photothermally via sufficiently strong photoexcitation and the concomitant rise in temperature.[187,188] The photoexcitation can occur either directly via resonant excitation of the aggregates or indirectly by excitation energy transfer (EET) via a sensitizer.[189,190] Inorganic semiconductor nanocrystals (NCs) are ideal as sensitizers as they exhibit much larger extinction coefficients than most organic dyes and strong absorption at above-band gap photon energies.[191] EET between NCs and organic π-systems has been extensively investigated in both: solution and solid state. However, to the best of our knowledge, no research has been committed specifically towards involving AIE molecules.[192–198]

Here, we combine aggregates of the aryleneethynylene derivative AE **1** (**Figure 1a**) with pronounced AIE together with CdSe NCs into a hybrid nanocomposite. We show that EET between the NCs and the molecular aggregates in combination with photothermally induced structural changes lead to temporal fluctuations of the NC fluorescence and the degree of AIE in the aggregates, which are anticorrelated to each other. At low temperature, these

intensity fluctuations become periodic. EET plays a role in charge carrier transport during photocurrent experiments.

Results

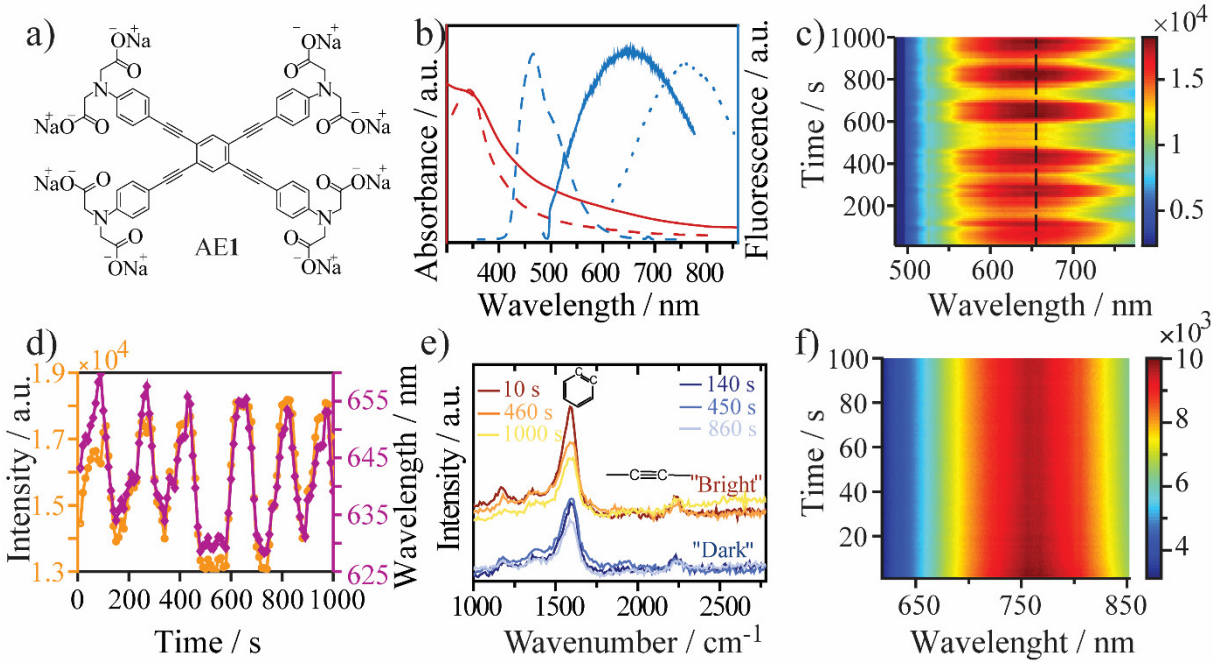

Figure 4-1 a) Structural formula of the arylenephenylene derivative AE **1**. **b)** Optical properties of AE **1**. Absorption in methanol (red dashed line), thin-film absorption (red solid line), fluorescence in methanol (blue dashed line, excitation at 350 nm), thin-film fluorescence (blue solid line, 488 nm excitation) and thin-film fluorescence at 160 K (blue dotted line, 488 nm excitation). **c)** Thin-film fluorescence during 1000 s of continuous excitation at 488 nm with a binning time of 1 s. **d)** Line profile (orange solid) and wavelength maxima position (purple) of c) extracted by fitting gaussian functions. **e)** Raman spectra taken during "bright" periods (at 10, 460 and 1000 s) and "dark" periods (at 140, 450 and 860 s). Bands attributed to the phenyl-C=C breathing and the C≡C stretching mode are indicated. **f**) Thin film fluorescence at 160 K during 100 s of continuous excitation at 488 nm.

In methanolic solution, AE **1** shows broad absorption with a maximum at 350 nm, including a weak low-energy tail, and narrow, dim emission at 480 nm (**Figure 1b, red and blue dashed lines, respectively**). In the solid state, aggregates of AE **1** exhibit pronounced low-energy tailing of the absorption as well as broad, enhanced emission with a maximum at 650 nm and a lifetime (τ) of 0.8 ns (**Figure 1b, red and blue solid lines**). At 160 K, the fluorescence maximum is further red-shifted to 750 nm (**Figure 1b, dotted line**). These optical properties are typical for molecules with AIE and are consistent with other, similar

aryleneethynylenes.[183,185,199,200] Absorption and fluorescence of AE **1** are strongly dependent on the extent of conjugation of the π-electron cloud, for which the torsion angles of the five phenyl rings are an important measure.[201] For torsion angles close to 0 °, the molecule is fully planarized, the degree of π-conjugation is maximized and the energy of this rotamer is minimized.[202] In the ground state, the energy difference between rotamers of different torsion angles is low (< 4 KJ/mol) and a wide range of rotational states are populated.[203] This leads to the broad absorption feature in **Figure 1b**. In the excited state, the torsion-angle dependent energy profile of the rotamers becomes much steeper ($\Delta E \approx 30$ KJ/mol)[204] and, an unhindered rotation provided, radiative emission will occur from a narrow range of rotational states with relatively small torsion angles.[203] This narrows and red-shifts the fluorescence compared to the absorption. In the solid state, structural rigidity favors rotamers with small torsion angles and enforces a higher degree of planarization. This invokes the low-energy tailing of the absorption and the red-shift of the fluorescence in **Figure 1b**. Kinetic arrest of high energy rotamers due to the structural rigidity prevents the fluorescence line narrowing observed in solution and leads to a broad fluorescence feature. At low temperature, structural order and, thus, the degree of planarization, are enhanced further, which shifts the fluorescence to even lower energies.[205,206]

Continuous excitation at 488 nm under nitrogen atmosphere leads to substantial fluctuations (± 20 %) in the fluorescence intensity emitted by the AE **1** aggregates (**Figure 1c,d**). The timescale of seconds for the transition between an intensity maximum and minimum suggests that a macroscopic process, and not an electronic transition, is responsible for the fluctuations. Within the theory of AIE, this process needs to affect either the restriction of intramolecular motion or the rate of formation of a photochemical intermediate to result in fluorescence intensity fluctuations.[181] Photothermally induced local structural changes are a likely cause for less restricted intramolecular motion and faster non-radiative recombination. Indeed, we observe significant local changes in the optical scattering and luminescence images of AE **1** aggregates after laser excitation, indicating an altered morphology (see **Figure S1**). Furthermore, we find a strong correlation between the intensity and the peak wavelength of the fluorescence, in that a lower intensity coincides with a blue-shifted fluorescence peak (**Figure 1d**). This is consistent with a transformation from a more planarized structure with high fluorescence quantum yield to a less-planarized structure with fast non-radiative recombination. To test for the formation of a photochemical intermediate as an alternative cause for the intensity fluctuations, we compare the Raman bands of AE **1** appearing together

with the fluorescence signals of different intensity (**Figure 1e**). We find a strong band at 1590 cm^{-1} and a weak signal at 2230 cm^{-1}, which we assign to the phenyl-C=C breathing and the C≡C stretching mode in agreement with earlier reports.[206,207] There are no substantial differences between Raman spectra taken during periods of fluorescence intensity minima vs. maxima, suggesting that chemical transformations of AE **1** are not responsible for the fluorescence intensity fluctuations. Over the course of 1000 s of continuous excitation, the intensity of the phenyl-C=C breathing mode decreases in comparison with that of the C≡C stretching mode. However, this evolution progresses within periods of low and high fluorescence intensity alike.

We conclude that the fluorescence intensity fluctuations of AE **1** under continuous 488 nm laser excitation are probably caused by a photothermally induced order/disorder transition. This transition locally increases the non-radiative recombination rate due to bond rotation and decreases the fluorescence quantum yield. In the disordered, "solution-like" state, the absorption of AE **1** at 488 nm is weakened (**Figure 1b**), which now decreases the rate of photothermal heating and allows for a recovery of the initial optical properties of the AE **1** aggregates. At 160 K, the fluorescence fluctuations disappear (**Figure 1f**). We suspect that photothermal heating may not be sufficient at this temperature to invoke the same structural changes that lead to the random fluorescence fluctuations in **Figure 1c**.

In **Figure 2**, we analyze the solid-state fluorescence of AE **1** aggregates coupled to the surface of iodide-capped CdSe nanocrystals (CdSe/I^- NCs) at room temperature. The NCs were chosen based on the large spectral overlap between their fluorescence (**Figure 2a, blue solid line**) with the absorption of AE **1** aggregates (**Figure 2a, red dashed line**) to enable efficient EET. The absorption spectrum of the hybrid material (CdSe/I^-/AE **1**) is dominated by the absorption of the CdSe NCs (**purple dashed line**), while the fluorescence spectrum bears two well-resolved, narrow bands at 636 nm and 734 nm (**purple solid line**). Wavelength-selective fluorescence lifetime measurements of these bands reveal τ = 0.8 ns at 734 nm and a longer lifetime at 636 nm with τ = 1.5 ns (**Figure 2b**). Based on this, we assign the band at 636 nm to the CdSe/I^- NCs and the band at 734 nm to AE **1**.

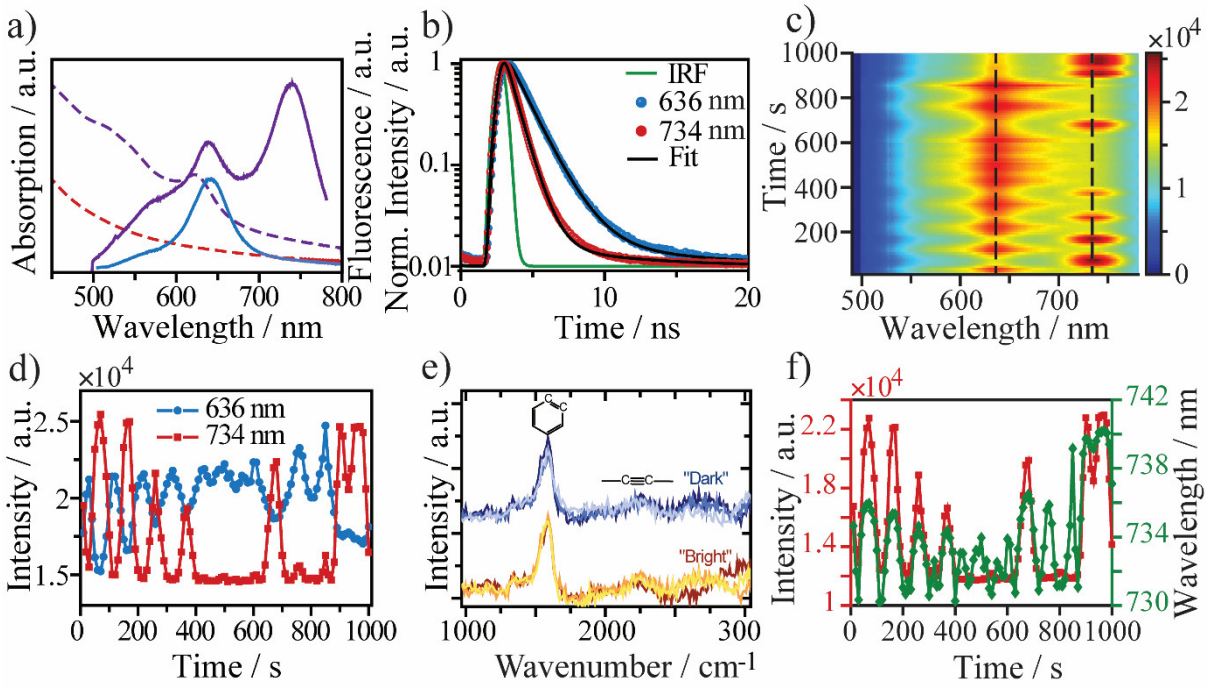

Figure 4-2 a) Thin-film absorption (purple dashed line) and thin-film fluorescence (purple solid line) of CdSe/I$^-$/AE **1**. Excitation at 488 nm. For comparison, the fluorescence of the CdSe/I$^-$ NCs (blue solid line) and the absorption of pure AE **1** (red dashed line) are also displayed. **b)** Fluorescence lifetime measurements of the CdSe/I$^-$/AE **1** bands centered around 636 nm (blue) and 734 nm (red) and their fit (black). The instrument response function (IRF) is displayed in green. **c)** Thin-film fluorescence of CdSe/I$^-$/AE **1** during 1000 s of continuous excitation at 488 nm with a binning time of 1 s. **d)** Line profile of c) cut at 636 nm and 734 nm. **e)** Raman spectra taken during "bright" and "dark" periods. **f)** Peak position of the low energy band in c) (green) compared with the intensity of the same band (red).

Continuous excitation at 488 nm with 1 to 10 MW/cm^{-2} and nitrogen atmosphere of CdSe/I$^-$/AE **1** results in the temporal fluctuations in the fluorescence spectrum depicted in **Figure 2c**. The fluctuations occur gradually over a timescale of 10 – 30 s with ON/OFF-periods of similar duration. Most notably, the ON/OFF periods of the bands at 636 nm and 734 nm are mostly anti-correlated, that is, an increase of the NC fluorescence occurs together with a decrease of the AE **1** emission and vice versa (**Figure 2d**). We verify that CdSe/I$^-$ NCs without AE **1** do not exhibit similar fluorescence fluctuations (**Figure S2**). Similar to pure AE **1**, we find the same Raman signals at 1590 cm^{-1} and 2230 cm^{-1}, which do not change significantly during relative ON or OFF periods (**Figure 2e**). Here however, the intensity of the phenyl-C=C breathing mode remains constant, indicating a higher photostability of the hybrid composite compared to pure AE **1**. Another similarity between CdSe/I$^-$/AE **1** and the pure molecule is the strong correlation of the intensity (red) and peak wavelength position

(green) of the fluorescence of AE **1** (**Figure 2f**). In contrast, the peak wavelength position of the CdSe/I^- fluorescence remains constant throughout the fluctuations.

At 160 K and helium atmosphere, the temporal fluorescence fluctuations of CdSe/I^-/AE **1** become periodic (**Figure 3)**. At 45 kW/cm^2 excitation power density, the two fluorescence bands of the CdSe/I^- NCs and the AE **1** aggregates are quasi-continuous over a timescale of 200 s (**Figure 3a)**. Increasing the excitation power density to 615 kW/cm^2 induces periodic oscillations of the intensity of both fluorescence bands by ± 20 %, which remain exactly anti-correlated (**Figure 3b-e**). The peak wavelength position of AE **1** (**Figure 3d, purple**) follows the intensity fluctuations (**Figure 3d, blue**) almost perfectly, however, the variations are significantly smaller compared to room temperature (**Figure 2f**). The periodicity of the fluctuations depends on the excitation power density and varies with a period of 115 s at 80 kW/cm^2 to 26 s at 620 kW/cm^2 (**Figure 3f**) as determined from the sine fits shown in **Figure 3e**.

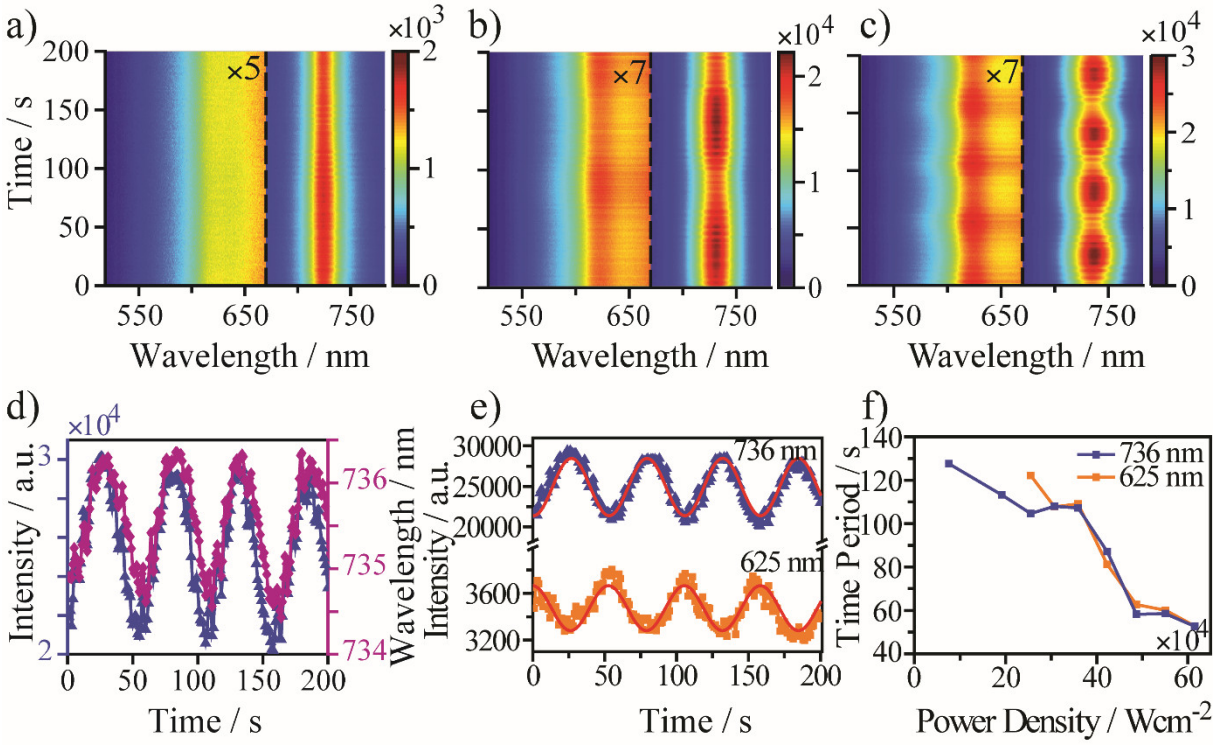

Figure 4-3 Thin-film fluorescence at 160 K of CdSe/I⁻/AE **1** during 200 s of continuous excitation at 488 nm with a binning time of 1 s and varying laser power. **a)** 45 kW/cm^2, **b)** 360 kW/cm^{2}and **c)** 615 kW/cm^2. **d)** Peak position of the low energy band in c) (purple) compared with the intensity of the same band (blue). **e)** Line profile of c) cut at 625 nm and 736 nm. **f**) Correlation between the laser power and the period of one complete oscillation in e) for the fluorescence bands at 620 nm (blue) and 725 nm (orange).

Since thin films of CdSe/I⁻ NCs exhibit a strong field-effect and photocurrent response, we now explore the effect of including AE **1** into such devices.[70] **Figure 4a** compares the electric conductivity (σ) in the dark of CdSe/I⁻ NCs before (**blue**) and after (**orange**) functionalization with AE **1** between 8 – 300 K. The dark conductivities are mostly identical apart from a window of intermediate temperatures (100-200 K), where the presence of AE **1** invokes an increase in σ. Under optical excitation with λ = 408 nm, the conductivities with AE **1** are much higher than for the bare CdSe/I⁻ NCs at all temperatures (**Figure 4b**). However, the corresponding field-effect mobilities under optical excitation (**Figure 4c & Figure S3**) are the same for both materials. Thus, the effect of AE **1** is mainly an increase of the free carrier concentration (n) in the NC ensemble under optical excitation, since $\sigma = \mu \cdot e \cdot n$, with the elemental charge e. Comparing the field-effect mobilities for CdSe/I⁻/AE **1** NCs in the dark (**Figure 4d, blue**) *vs.* the excited state (**orange**) reveals that transport under optical excitation

becomes exceedingly more efficient than in the dark as the temperature decreases. This indicates the importance of the population of trap states: At low temperature, these states may only be populated through photoexcitation as thermalization is not sufficient anymore.

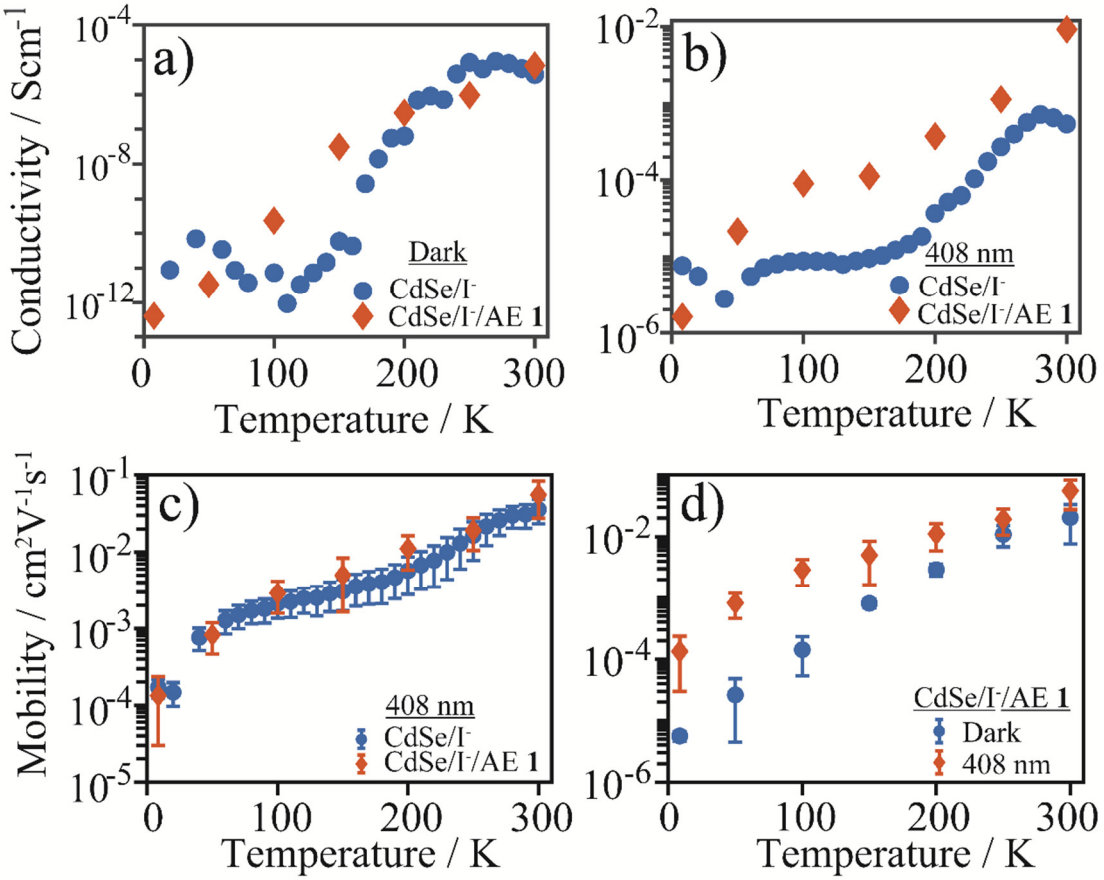

Figure 4-4 Temperature-dependent electric conductivity in the dark (**a**) and under 408 nm excitation (**b**) of thin films of CdSe/I$^-$ NCs (blue) and CdSe/I-/AE **1** (orange). (**c**) Temperature dependence under 408 nm excitation of the field-effect mobility of the same thin films. (**d**) Comparison of the dark (blue) and excited-state field-effect mobility (orange) of CdSe/I-/AE **1** thin films.

Discussion

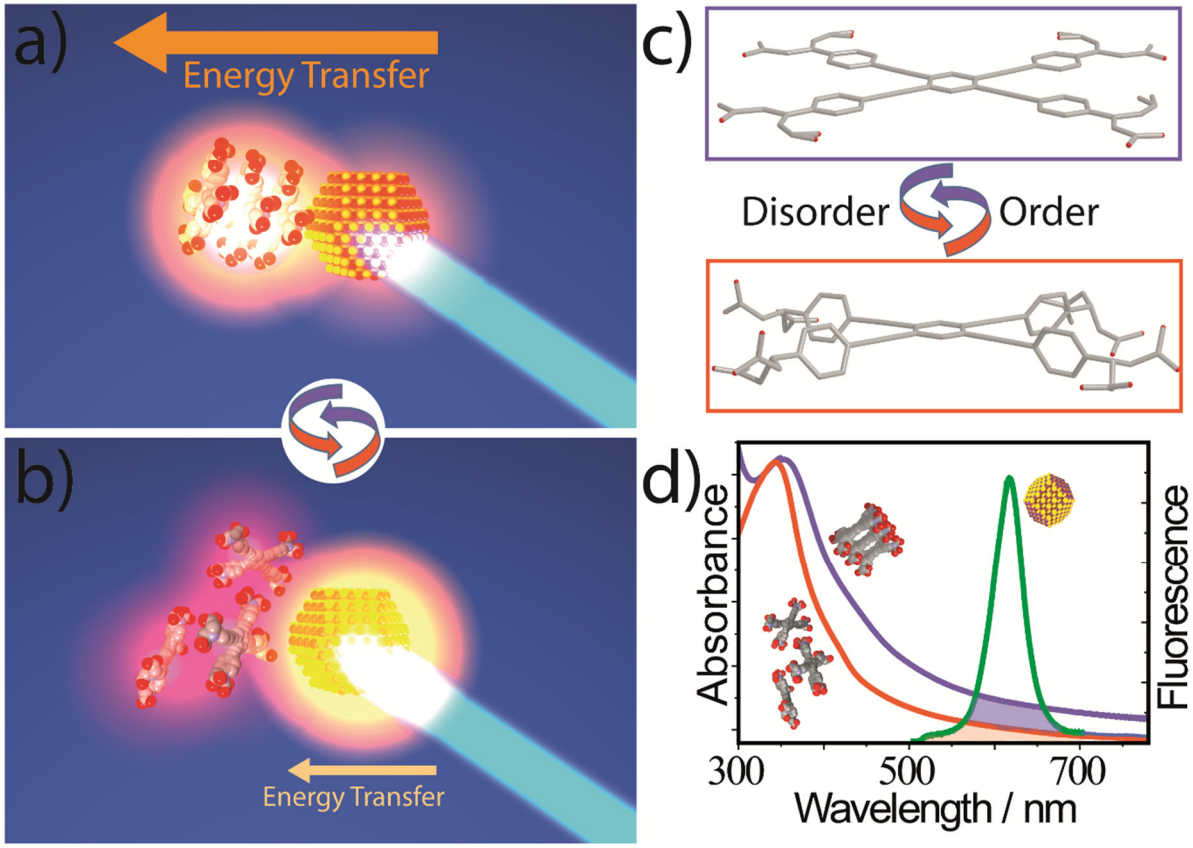

Scheme 2 a-b). Idealized schematic of the two structural scenarios proposed for CdSe/I$^-$/AE **1** composites with different energy transfer efficiency. **c)** Qualitative description of the proposed order/disorder transition. **d)** Spectral overlap between NC emission (green) and AE **1** absorption in the ordered (blue) and disordered (red) state.

We suggest that changes in the EET efficiency from excited CdSe/I$^-$ NCs to aggregates of AE **1** are responsible for the anticorrelated fluctuations in the CdSe/I$^-$/AE **1** nanocomposite (**Scheme 1a,b**). Under 488 nm excitation, most of the light is absorbed by the inorganic NCs as reflected by the absorption spectrum in **Figure 2a**, which mimics that of the pure NCs. The NC fluorescence overlaps with the absorption of AE **1**, resulting in efficient EET, which weakens the CdSe fluorescence signal and strengthens the molecular fluorescence. In **Figure 3e**, this scenario applies when the fluorescence band at 736 nm is at a maximum and the band at 625 nm is at a minimum, e.g. after 25 s. Simultaneously, this EET invokes photothermal heating of the AE **1** aggregates, eventually triggering an order/disorder transition to break up the aggregates. The result of this transition is a reduced degree of planarization (**Scheme 1c**), which blueshifts the absorption spectrum, decreases the overlap with the NC fluorescence (**Scheme 1d**), weakens the efficiency of EET, diminishes the molecular fluorescence and

brightens the emission of the NCs. In **Figure 3e**, this scenario applies when the fluorescence band at 736 nm is at a minimum and the band at 625 nm is at a maximum, e.g. after 55 s. In the disordered state, EET is slow and photothermal heating is weak, such that new aggregates of AE **1** may form and the initial state with efficient EET from the NCs to the aggregates is restored. An illustration of the different absorption and emission pathways underlying this picture are provided in **Scheme S2** in the Supporting Information.

The overall interpretation in **Scheme 1** is consistent with the laser power-dependent period for one complete cycle (**Figure 3f**) as increasing the number of photons will increase the rate of heat transfer, which should shorten the cycle period. It is furthermore supported by the fluorescence fluctuations of pure AE **1** in **Figure 1**, which are likely due to a similar order/disorder transition of the aggregates. Relaxing the structural rigidity in molecular emitters with AIE increases the rate of non-radiative recombination and decreases the fluorescence intensity.[181] The higher stability of the Phenyl-C=C moiety in the nanocomposite (**Figure 2e**) compared to the pure molecule (**Figure 1e**) is consistent with mostly indirect excitation of AE **1** in the nanocomposite by EET *vs.* direct excitation of the pure molecule leading to photodegradation. EET as the main electronic interaction between the CdSe NCs and AE **1** is also consistent with the fluorescence lifetime data in **Figure 2b**. The essentially unchanged fluorescence lifetimes of the NCs and the molecular aggregates after combination into the hybrid material implies localized excitons, either on the NCs or the molecules. In particular, there are no indications for transfer of single charges and the formation of an interfacial exciton, for which one would expect much longer fluorescence lifetimes similar to those in type II core/shell NCs.[173]

The mobility data (**Figure 4c**) suggests that AE **1** does not enhance electronic coupling between the CdSe/I^- NCs. Transport occurs via hopping between adjacent NCs, irrespective of the presence of AE **1**. The increase in the carrier concentration with AE **1** under optical excitation (**Figure 4b**) implies that excitons dissociate into locally trapped charge carriers before they reach the electrodes, which mainly increases the free charge carrier density and not the field-effect mobility. A large trap state density is indicated by the differences in the dark vs. excited state mobilities at low temperature (**Figure 4d**). We suggest that reducing the density of trap states should increase the exciton diffusion lengths in CdSe/I^-/AE **1** NC thin films with the potential to exploit EET as an additional means of charge carrier transport. This

may enable similar periodic fluctuations in the electric transport properties as those demonstrated for the fluorescence.

Conclusion

Coupling organic π-systems that exhibit aggregation induced emission to a second fluorophore can result in emergent optical properties, such as dual fluorescence with oscillating intensity fluctuations. This is realized in a hybrid thin film consisting of CdSe nanocrystals coupled to aggregates of an aryleneethynylene derivative with fluorescence from both fluorophores, which establish a feedback loop: excitation energy transfer from the nanocrystals to the aggregates leads to photothermal heating and an order/disorder transition in the aggregates. This transition weakens the fluorescence intensity of the organic π-system and the rate of energy transfer, which strengthens the nanocrystal fluorescence. Simultaneously, the slower energy transfer rate reduces photothermal heating, which gradually restores the initial structure and optical properties of the molecular aggregates. This closes the feedback loop and initiates the next cycle. The resulting optical oscillations and their temperature dependence may be of interest for application in nanothermometry.

Supporting Information.

(Figure S1) Luminescence and scattering images of pure linker and CdSe/I-/AE 1, **(Figure S2)** Fluorescence of CdSe/I-, **(Figure S3)** Gate sweeps of CdSe/I- and CdSe/I-/AE 1. **(Scheme S1)** Schematic of time-resolved photoluminescence instrument. Experimental details and methods. (**Scheme S2**) Schematic of the absorption and emission pathways in CdSe/I-/AE 1 NC thin films in the ordered as well as the disordered state.

Corresponding Author

*Email: marcus.scheele@uni-tuebingen.de and uwe.bunz@oci.uni-heidelberg.de

Author Contributions

The manuscript was written through contributions of all authors. All authors have given approval to the final version of the manuscript.

Acknowledgements

Financial support of this work has been provided by the Emmy Noether program of the DFG under grant SCHE1905/3-1 and ME 1600/13-3.

Publication 3 *(Draft)*

5 Influence of the Ligand Density on Self-Assembly of CdSe Nanocrystals

Introduction

The various forces and parameters acting on nanocrystals during self-assembly, which ultimately may lead to a highly ordered NC superlattice, have been subject of intense research efforts.[208] Moreover, the self-assembly of semiconductor NCs is also interesting for their application in electronic devices as the control over the long-range order of the conductive NCs assembly provides a means to significantly improve the properties of the superlattices in electric devices.[209–211]

Lead salt NCs (PbX; X=S, Se) are the most-widely studied materials for self-assembly as they are easily prepared, allowing the assessment of parameters like solvents/evaporation rate[212–214], temperature[215,216], surface coverage[217], free ligand influence[218], *etc*. The self-organization of CdSe NCs was first shown by Bawendi and coworkers.[219] However, since this seminal work, similar follow-up studies for CdSe NCs have been surprisingly scarce despite their significance for electronic and optical devices.[62,70,220–223] In particular, X-ray based structural studies of CdSe NC superlattices are rare. Interestingly, the self-assembly of anisotropic CdSe NCs (e.g. nanorods or -platelets) is comparatively more explored than that of spherical NCs.[224–226] Covalently necked honeycomb superlattices of CdSe NCs have also been reported by Vanmaekelbergh *et al.*[227] However, the CdSe honeycomb structure was prepared by cation exchange from a preformed PbSe honeycomb structure.

In this work, we have synthesized CdSe NCs in the wurtzite and zinc-blende crystalline phase. By using 1H NMR spectroscopy, we quantify the unbound and bound ligand densities on the CdSe NCs to reveal their influence on the self-assembly into superlattices. By applying small-angle X-ray scattering (SAXS) in transmission as well as grazing incidence small-angle X-ray scattering (GISAXS), we show that the degree of long-range order as well as the superlattice cell parameter can be tuned via the ligand densities.

Results and Discussion

Absorption spectroscopy and Wide-angle X-ray scattering

The crystalline phases of the two sets of CdSe NC samples were verified by optical spectroscopy and wide-angle X-ray scattering (WAXS) as shown in **Figure 5-1**. In absorption spectroscopy, the wurtzite and zinc-blende phase have been shown to exhibit distinctive relative positions of the first two excitonic peaks owing to the different electronic structure of the respective phase.[228–230] The absorption spectra presented in **Figure 5-1a gray solid line** shows ~0.096 eV difference in the first two excitonic peak energies for wurtzite. For the zinc blende phase (**Figure 5-1a blue solid line**), the difference is ~0.11 eV, which agrees with the above literature reports. We calculated the sizes of the NCs as 4.8 and 5.3 nm, respectively, using the empirical relationship between the NC diameter and the first excitonic peak of CdSe NCs. [106]

The WAXS characterization of the two crystalline phases is displayed in **Figure 5-1b**. Line broadening of the Bragg peaks due to the small crystalline domains renders the two scattering patterns quite similar. However, there are still notable differences present to distinguish the two phases. The supposedly zinc blende structure (blue data) exhibits three prominent peaks, which we assign to the <111>, <220> and <311> Bragg reflections. In contrast, the supposedly wurtzite sample (gray data) contains a significantly broadened peak centered at 1.76 $Å^{-1}$ which likely originates from three Bragg peaks, namely the <100>, <002> and <101> families. Two weak additional reflections are present at 2.5 $Å^{-1}$ and 3.2 $Å^{-1}$, which we attribute to the <102> and <103> planes, confirming the presence of the wurtzite phase.

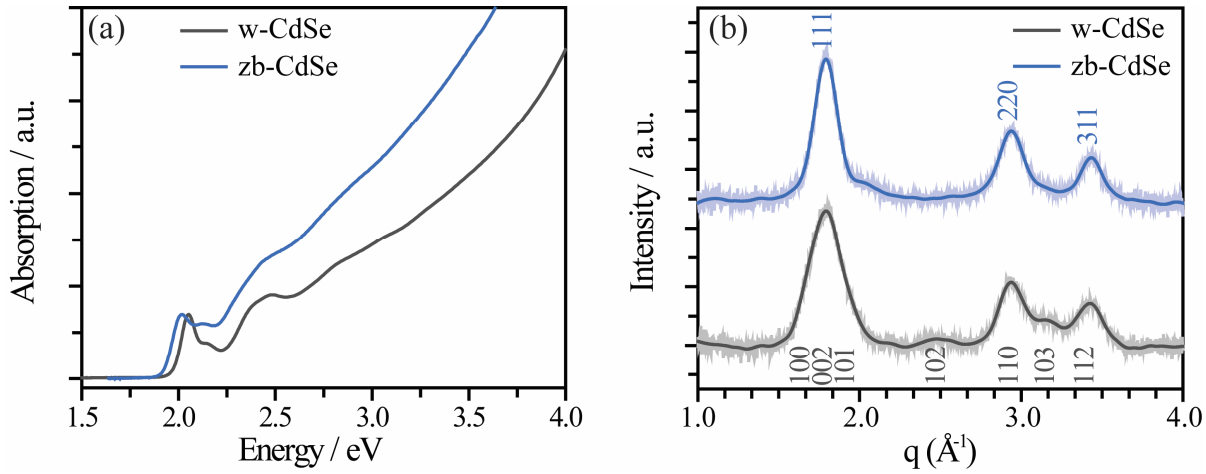

Figure 5-1 Characterization of two different phases of CdSe NCs. (a) Absorption spectra of CdSe NCs in the wurtzite (gray) and zinc blende (blue) phase. (b) Wide-angle X-ray scattering of the wurtzite (gray solid line) and zinc blende (solid blue line) NCs.

NMR Spectroscopy

NMR spectroscopy can be used to distinguish between free and bound ligands in colloidal CdSe NC samples due to differences in the diffusion constant and, thus, relaxation kinetics.[107,231] To this end, the olefinic protons of oleic acid have been used as spectroscopic reporters to determine the ligand concentration against a known concentration of ethylene carbonate dissolved in toluene-d_8. The standard peak of ethylene carbonate (3.09 ppm) is well separated from the olefinic proton region (5.4–5.7 ppm) and does not interfere with the quantification. We use a similar procedure to record the NMR data for 4.8 nm wurtzite shown in **Figure 5-2**. Thoroughly cleaned particles (**Figure 5-2a**) were dissolved in d_8-toluene for NMR data acquisition. Subsequently, free oleic acid was added in a step by step manner (**Figure 5-2b & c**). The sharp peaks at 5.73 & 5.9 ppm are unidentified and have been ignored for the area under the curve calculations. The NMR data show a density of 0.48 OA/nm^2 bound to the NC surface for no addition of oleic acid (**Figure 5-2a**), 0.65 OA/nm^2 (**Figure 5-2b**) and 0.89 OA/nm^2 (**Figure 5-2c**) for 23.7 and 47.4 µL addition of oleic acid. These values fall in the lower range of values reported in literature (1.2– 4.6 OA/nm^2).[107,231,232] However, it should be noted that unaccounted ligands like trioctylphosphine oxide (TOPO) and hexadecylamine (HDA) could also be present. The free ligand fraction is estimated as $N_f/(N_b + N_f)$, where N_f and N_b are the number of free and bound oleic acid per NCs. The

calculated free ligand fraction is 0, 0.97, and 0.98 for no oleic acid addition and two further additions respectively.

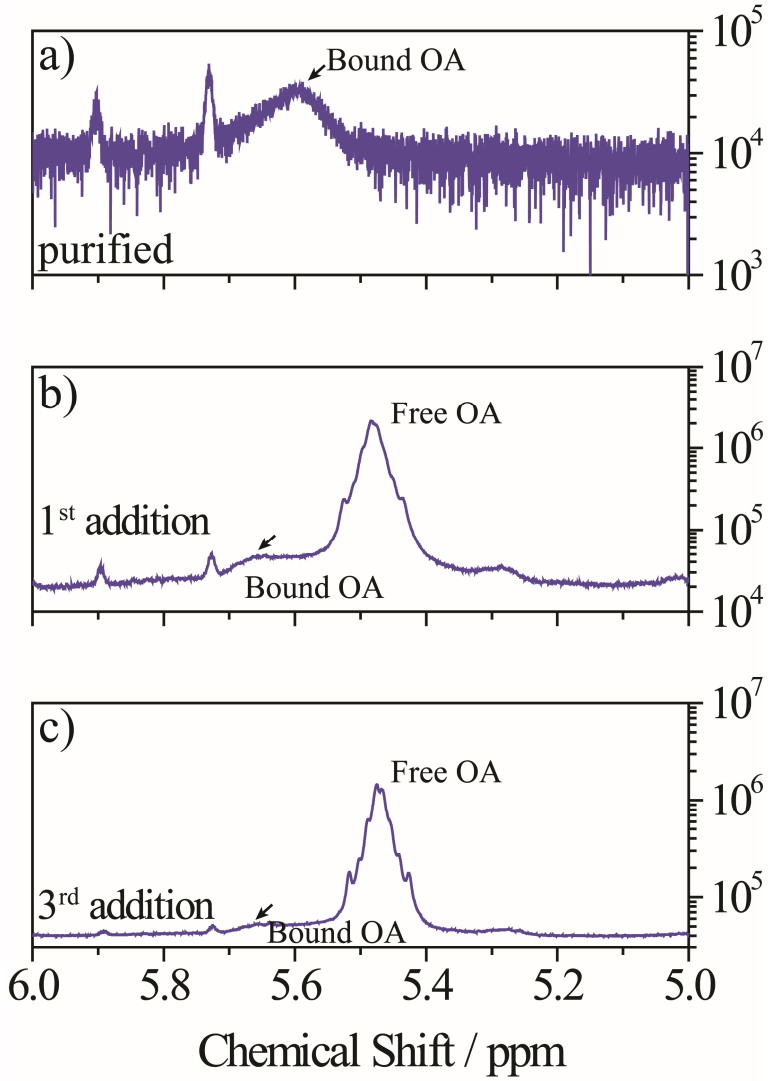

Figure 5-2 Determination of the free and bound ligand concentration using NMR spectroscopy. a) Olefinic region of the cleaned particles. b & c) graph corresponds to the subsequent addition of free oleic acid in wurtzite CdSe NCs solution. OA stands for oleic acid.

Small-angle X-ray Scattering

To quantify the effect of excess ligand concentration on the CdSe NC self-assembly, we used small-angle X-ray scattering (SAXS) in **Figure 5-3**. We did not observe any scattering patterns showing long-range order in the self-assembled thin-film of the as purified NCs. Purified CdSe wurtzite NCs of 4.8 nm diameter (**Figure 5-3a**) showed an amorphous ring pattern with the nearest neighbor distance (NND) of $7.7 \pm 0.1\ nm$. The subsequent addition of

free OA to the NC solution altered the NND in the amorphous regions of the NC film to $7.4 \pm 0.3\ nm$ and $8.4 \pm 0.5\ nm$, respectively. Upon this addition, we also observe the emergence of ordered domains in the film, manifesting in six-fold scattering patterns (**Figure 5-3b,c**), which we tentatively attribute to a hexagonal close-packed structure (hcp) with unit cell parameters $a = 7.1 \pm 1.5\ nm$ and $7.5 \pm 0.2\ nm$, respectively. Since a = NND in a hexagonal cell, we note that the NNDs in the ordered domains of the superlattice are shorter than in the amorphous domains for the same amount of added OA (compare **Figure 5-3d vs. h**).

A similar behavior is also shown by the zinc-blende (ZB) phase of 5.3 nm CdSe NCs system as presented in **Figure 5-3e–g**. Thoroughly washed ZB NCs do not show any long-range ordering (**Figure 5-3e**), but rather an amorphous arrangement of NCs with an NND of $7.8 \pm 0.1\ nm$. The NND increased to $8.0 \pm 0.3\ nm$ and $9.0 \pm 0.3\ nm$ with addition of free ligand, respectively (**Figure 5-3f,g**). Again, we begin to observe a six-fold scattering pattern with the first addition of free oleic acid and more prominently with the second addition. This indicates the formation of some ordered domains aside the already described amorphous regions. Similar to the wz-NC data, we tentatively attribute the ordered domains to an hcp structure and derive the lattice parameters $a = 7.6 \pm 0.3\ nm$ (**Figure 5-3f**) and $8.5 \pm 0.2\ nm$ (**Figure 5-3g**), respectively.

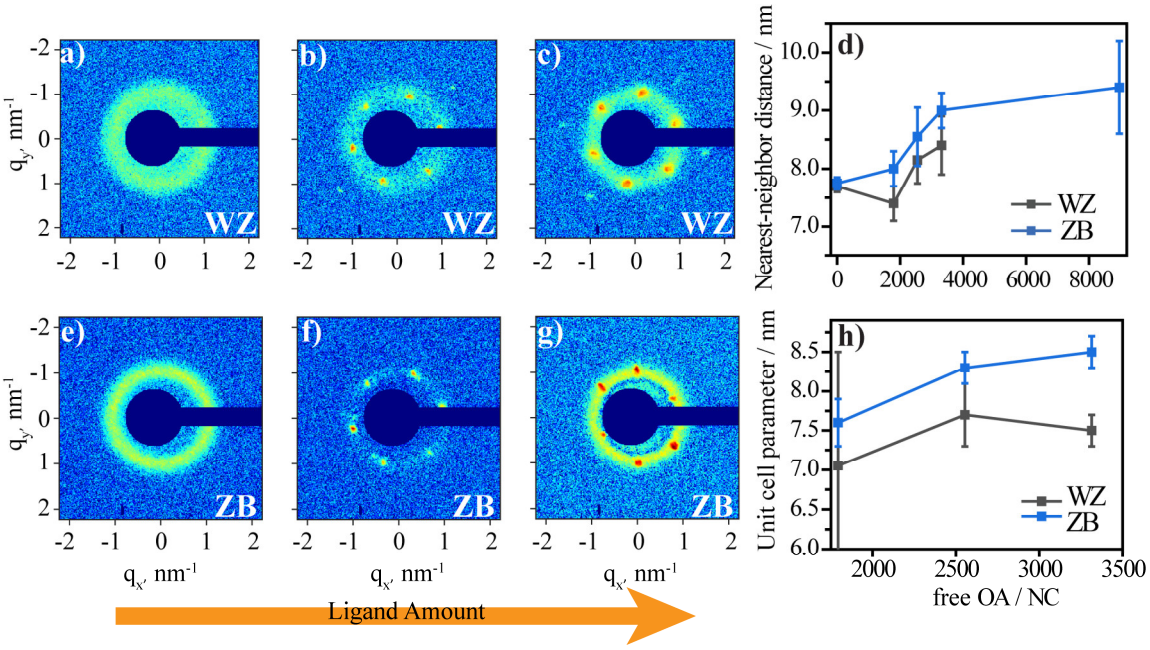

Figure 5-3 Small-angle X-ray scattering of the wurtzite (a-c) and zinc blende (e-g) CdSe NCs with increasing free ligand amount. The appearance of an ordered structure in both samples with the addition of free ligand becomes apparent. The effect of increasing the amount of oleic acid on the nearest neighboring distance (d) of the amorphous film and on the unit cell parameter (h) of the self-assembled NCs with long-range order.

To quantify the effect of ligand addition on the self-assembly of the CdSe NCs, we analyzed the scattering patterns from a range of samples presented in **Figure 5-3d&h**. The amorphous regions of the thin film showed an overall increase of the NND of 10% and 21% for the WZ and ZB phases, respectively, as the free oleic acid amount is increased. The NND showed beginning saturation upon the addition of roughly 9000 OA molecules per NC **(Figure 5-3d)**. The lattice parameter of the ordered superlattices also showed ~10% growth with increasing ligand concentration **(Figure 5-3h)**.

Grazing-incidence small-angle X-ray scattering

We also looked at the self-assembly of 5.1 nm wurtzite and 5.2 nm zinc blende NCs prepared on a silicon substrate using grazing-incidence small-angle X-ray scattering (GISAXS) to confirm the unit cell parameters of the ordered structure. We added a similar amount of free oleic acid as that which led to a OA/NC ratio of 1700 in the NMR and SAXS experiments. The scattering data are displayed in **Figure 5-4**. Self-assembled wurtzite CdSe NCs show a strong scattering rod pattern (**Figure 5-4a**), indicating a preferential perpendicular lamellae type ordering. We fitted the scattering data using a slightly distorted hexagonal unit cell having $a =$

$b = 8.1$ and $c = 14.2\ nm$ as well as $\alpha = \beta = 89.5°$ and $\gamma = 120°$. In contrast, the zinc blende NCs showed many-fold ring shaped scattering with strong directional orientations. We were able to fit the experimentally observed scattering pattern using the hexagonal like closed pack structure oriented in a mixture of different orientations (001, 010,101,110) and unit cell parameters $a = b = 8.5$ and $c = 26\ nm$ as well as $\alpha, \beta = 92$ and $\gamma = 118°$. This indicates that the ZB NCs have multiple preferred facial orientation with respect to the substrate plane. However, we were not able to fit the scattering peaks on all the four rings with c-axis close to the expected hexagonal crystal system.

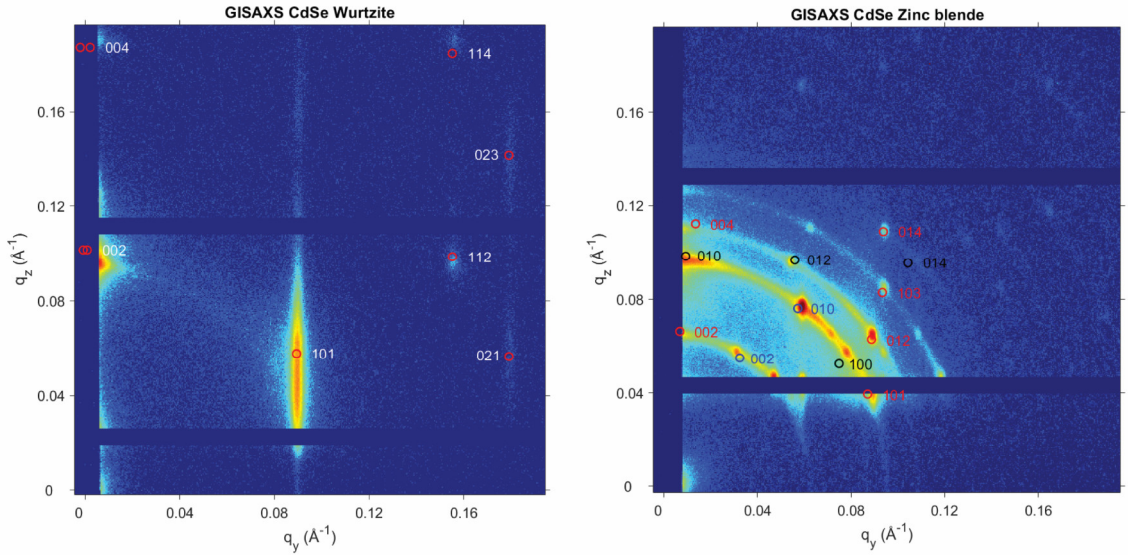

Figure 5-4 Grazing incidence small-angle X-ray scattering data. (a) Wurtzite NCs scattering pattern together with hexagonal close pack simulated pattern showing a good agreement with the experimental peaks. (b) GISAXS scattering peaks from self-assembled zinc blende NCs along with the simulated pattern having multiple crystal orientation parallel to the substrate plane. Differently colored miller planes are the projections of different nanocrystal orientations parallel to the plane of the substrate.

Purification steps can sometime remove the bound ligands from the surface of the NCs as well. This decreases the ligand density of NCs and increases the core to core interaction of NCs. Self-assembly from such NC solutions results in a disordered thin film (**Figure 5-3a,e**). The addition of free ligands increases the surface ligand density (**Figure 5-2b,c**) and the excess of free ligand helps to form a long range ordered assembly of NCs on slow evaporation of solvent (**Figure 5-3b,c,f,g**). The increased amount of free ligand allows expanding the nearest neighbour distance up to 21% in the amorphous film (**Figure 5-3d**). In addition, the excess ligand helps in the formation of ordered assemblies and increases the lattice parameter by up

to 10% (**Figure 5-3h**). The GISAXS data showed slightly larger (~0.8 nm) unit cell parameters, even after taking differenct sizes of NCs ino account, then the lattice parameters obtained by SAXS measurements.

Conclusion

In summary, we synthesized and characterized two phases of CdSe NCs and studied the effect of free ligand amount on the self-assembly of the NCs. The addition of free oleic acid increases the surface coverage of the wurtzite NCs as shown by NMR spectroscopy. Our results show that the completely cleaned NCs form unordered assemblies on drying. Increased ligand interactions appear to help in preventing kinetic arrest and fascilitate the formation of assemblies with a higher degree of long-range order. We statistically showed the free ligand concentration provides a handle to tune unit cell volume.

Experimental Section

Chemicals

Cadmium oxide (CdO, 99.99%, Aldrich), oleic acid (OA, 90%, Aldrich), trioctylphosphine (TOP, 97%, Abcr), trioctylphosphine oxide (TOPO, 99%, Aldrich), hexadecylamine (HDA, 90%, Aldrich), 1-octadecene (ODE, 90%, Acros Organics), selenium pellet (Se, 99.999%, Aldrich), ammonium iodide (99.999%, Aldrich), N-methylformamide (NMF, 99%, Aldrich), hexane (Extra Dry, 96%, Acros Organics), ethanol (Extra Dry, 99.5%, Acros Organics), acetone (Extra Dry, 99.8%, Acros Organics), dimethyl sulfoxide (DMSO, 99.7%, Acros Organics), acetonitrile (Extra Dry, 99.9%, Acros Organics). All chemicals were stored and used inside the nitrogen-filled glovebox except the chemicals used in CdSe NCs synthesis.

Nanocrystal Synthesis

CdSe NCs were synthesized in wurtzite and zinc-blende crystal phases using the literature reported process.[105,174] The wurtzite phase was synthesized, briefly, 176.7 mg of CdO, 8 g HDA, 8 g TOPO, 2.2 mL OA in 45.8 mL ODE taken in a three-neck round bottom flask. The content of the flask was degassed for 2 h at 10^{-2} mbar. The mixture was dissolved at 300 °C, and already prepared a mixture of 1.6 mL of 1 M TOPSe with 6.4 mL of TOP and 8.0 mL of ODE was added swiftly to the reaction mixture at 275 °C. After NCs growth for 25 min, the flask was submerged in the water bath to quickly quench the reaction. So, formed NCs were transferred to the glove-box and purified using first ethanol, then acetone, and finally

ethanol as antisolvents and repeating each step at least twice to completely clean the particles, unreacted raw material, and excess organic ligands. The particles were then redispersed in hexane.

Zinc blende crystalline phase NCs were prepared using literature procedure,[105] briefly, 22.5 mg CdO, 80 mg myristic acid, and 5 mL ODE taken in a three-neck round bottom flask and kept under vacuum for 2 h at 10^{-2} mbar. The slurry was heated to 240 °C for 5 min under N_2 atmosphere to dissolve the precursor material. The temperature was then reduced to 60 °C to add selenium precursor. A freshly prepared mixture of 1 mL cadmium acetate and 19 mg of SeO_2 in 12 mL ODE was added to the reaction mixture, and the temperature was raised to 240 °C, and 3 mL of 1:2 OA/ODE mixture was also added at this temperature and NCs were grown for 1 h. After that, NCs were taken inside the glove box for purification with toluene–acetone and toluene–methanol solvent–antisolvent combination. Further purification was carried out using DCM–ethanol mixture and then washing the oily NCs with acetone and centrifuging at 12000 rpm for 10 min and finally redispersing the NCs in hexane.

Ligand quantification

Nuclear magnetic resonance (NMR) speectroscopy is used to quantify the amount of free oleic acid and bounded oleic acid to the CdSe NCs surface using a 400 MHz Bruker instrument. Ethylene carbonate of known concentration (0.1 M) was used as internal standard to quantify the amount of oleic acid present (bound and free). The regions of the NMR peaks corresponding to free and bound ligands were integrated using the software TopSpin and compared to the integration of the standard peak. The satellite peak lying right to the free oleic acid peak was integrated and subtracted from the bound oleic acid peak to correct for the satellite peak contribution. The ligand densities were calculated using the concetration of NCs extractred from optical spectroscopy using the empirical relationship between the NC diameter and the first excitonic peak.[106]

Self-assembly preparation

Self-assembly of NCs was prepared on a Si_3N_4 window supported by Si substrate. We drop-casted roughly a 10-6 M CdSe NC solution on the substrate for a typical self-assembly experiment and allowed the solvent to evaporate in a semi-closed container. Small-angle X-ray scattering experiments were performed at P10 Coherence Beamline PETRA III at E=13.8 keV using GINIX setup. Eiger4M detector was placed at 370 mm downstream for the accessing SAXS and WAXS regions simultaneously. A 10×10 to 30×30 μm^2 area was scanned with

a step size ranging from 0.2 to 1 μm using a highly focused, 400 nm diameter beam and 0.3–0.5 s data acquisition time. Allowing us to get a statistical overview of the sample.

For in-house GISAXS measurements, samples were prepared on a silicon substrate using a similar procedure. The laboratory GISAXS is a Xenuss 2.0 Geniy3D setup using Cu ULD as the X-ray source, having 1.54 Å wavelength of energy 8.04 eV. Two slit pairs were used as the beam collimator achieving a $0.5 \times 0.5\ mm$ beam dimension. The scattering data were recorded using a Pilatus 300 K detector.

6 Summary (Zusammenfassung)

6.1 Summary

The work reported in this thesis is divided into three projects. This work focuses on the various properties of the CdSe nanocrystals. CdSe nanocrystals are one of the synthetically mature semiconductor nanocrystals. The size distribution of CdSe nanocrystals is narrow (≤ 5 %) with high reproducibility as well.[233] Therefore, these nanocrystals are highly suitable in terms of integrating nanocrystalline properties for their use in electrical/optical devices. This thesis explores the different aspects of such device preparation from nanocrystals. As synthesized nanocrystals have a layer of highly insulating organic surfactant molecules (such as oleic acid, trioctylphosphine oxide, hexadecylamine) necessary for their synthesis. However, these surfactant molecules inhibit the electronic interaction of neighboring nanocrystals in the solid-state by imposing a large energetic barrier of substantial height (large energy gap of molecular orbitals (MO) of ligands) and width (~twice the size of the bound ligands). So, these ligands have to be replaced with other ligand molecules in order to have an electrically conducting thin-film. Small inorganic ligands have been used for the surface modification of the nanocrystals and high mobilities for these devices have been achieved. The short inorganic ligands improve the electrical transconductance properties of the thin-film device however, as such they do not bring any novel properties to the system, or in other words, they serve no purpose from an electronic standpoint other than reducing the interparticle distance.[84,234]

The alternative route for surface modification is *via* ligand exchange with organic semiconductor ligands having molecular orbitals positioned to allow electronic coupling with the neighboring nanocrystals. This strategy of forming a hybrid material composed of large number of alternating organic and inorganic interface has an additional advantage in terms of charge transfer efficiency and invoking new material properties.[110,235] This thesis work explores the structural, optical, and electronic properties of thin-film CdSe nanocrystals and their enhancement by coupling them with organic dye molecules.

The first article shows the enhancement of the laser-assisted on/off properties of the CdSe nanocrystals coupled with Zn4APc dye molecules in the red spectral region. Remarkably, the coupled system shows an increase of ~4 orders of magnitude in photocurrent in the near-infrared region whereas the non-functionalised CdSe/I^- nanocrystals show poor response and a

slower rise of the photocurrent, which hints at surface trap-states. Transient absorption measurements show that the hybrid material exhibits charge transfer from dye molecule to CdSe nanocrystals in 5 ps. The hybrid system also illustrates a fast rise in photocurrent at 779 nm excitation as depicted by the time-resolved photocurrent measurements.

The second article shows the coupling of CdSe nanocrystals with aryleneethylene derivative (AE **1**). Long-chain organic π-linker show aggregation-induced emission in thin films or highly concentrated environments. The hybrid material poses a dual-band fluorescence behavior from the band-edge emission of the CdSe nanocrystals and the aggregation induced emission. Continuous measurement of the steady-state photoluminescence reveals that the intensity of these two bands (nanocrystals emission and the aggregation induced emission peak) varies randomly in an anticorrelated manner at room temperature, *i.e.,* the intensity of one peak increases with simultaneous decrease in the intensity of the other peak. This intensity change is also associated with ~10 nm change in the position of the aggregation induced emission band. The Raman peak extracted from the fluorescence spectrum of the hybrid film showed no sign of chemical transformation in the molecule during the intensity variation of the thin film. The intensity variation behaved in a periodic manner under low temperature and roughly an order of magnitude lower laser power. The time period of the oscillation of "on-off" fluorescence was observed to be dependent on the laser power. We attributed the fluorescence variations to the structural change in the alignment of the linker molecules effecting the energy transfer between nanocrystals and linker.

The third article investigates the structural properties of CdSe nanocrystals in wurtzite and zinc blende phases. NMR spectroscopy showed the amount of free and bound linker in the self-assembly solution of wurtzite nanocrystals. Interestingly, the self-assembly of nanocrystals showed a dependence on the availability of free linker in solution. Increasing the free linker showed 10–21% increase in nearest-neighboring distance in nanocrystals thin film and roughly a 10% increase in the lattice constant of the self-assembled particles.

For future endeavors in this field, one could explore the coupling of CdSe nanocrystals with different OSC linkers to further improve the mobility of the electrical device and the induced photocurrent with different excitation energy. Time-resolved photocurrent measurements of these hybrid nanocrystals have shown that these materials can display optical switching on the order of few tens to hundreds of nanoseconds. A more systematic study involving a detailed analysis of photocurrent measurements while exploring the effects of

parameters like temperature could be performed for a better understanding of the system. The optical properties of nanocrystals coupled with aryleneethylene derivatives, exhibit new fluorescence behavior; thus future work in the field could focus on exploring whether similar effects also arise with other cruciform linkers. If so, then how does temperature affect the optical properties? Also, the fluorescence enhancement could be checked for different bands using a tunable cavity mode.

6.2 Zussamenfassung

Die Arbeit, über die in dieser Dissertation berichtet wird, ist in drei Projekte unterteilt. Diese Arbeit konzentriert sich auf die verschiedenen Eigenschaften der CdSe Nanokristalle. CdSe Nanokristalle gehören zu den synthetisch ausgereiften Halbleiter Nanokristallen. Die Größenverteilung der CdSe Nanokristalle ist schmal (≤ 5 %) und weist ebenfalls eine hohe Reproduzierbarkeit auf.[233] Daher können diese Nanokristalle sehr gut in elektrischen/optischen Geräten eingesetzt werden, um nanokristalline Eigenschaften einzuführen. Diese Arbeit untersucht die verschiedenen Aspekte bei der Herstellung solcher Bauelemente aus Nanokristallen. Native Nanokristalle weisen eine Schicht aus hochisolierenden organischen Tensidmolekülen (wie Ölsäure, Trioctylphosphinoxid, Hexadecylamin) auf, die für ihre Synthese notwendig sind. Diese Tensidmoleküle hemmen jedoch die elektronische Wechselwirkung benachbarter Nanokristalle im festen Zustand, indem sie eine große Energiebarriere von beträchtlicher Höhe (große Energielücke der Molekülorbitale (MO) der Liganden) und Breite (~doppelt so groß wie die gebundenen Liganden) errichten. Diese Liganden müssen also durch andere Ligandenmoleküle ersetzt werden, um einen elektrisch leitenden dünnen Film zu erhalten. Für die Oberflächenmodifikation der Nanokristalle wurden kurze anorganische Liganden verwendet und es wurden hohe Mobilitäten für diese Bauelemente erreicht. Die kurzen anorganischen Liganden verbessern die elektrischen Transkonduktanzeigenschaften des Dünnschicht-Bauelements, bringen jedoch als solche keine neuen Eigenschaften in das System ein oder, anders ausgedrückt, sie dienen aus elektronischer Sicht keinem anderen Zweck als der Verringerung des Abstands zwischen den Teilchen.[84,234]

Der alternative Weg zur Oberflächenmodifikation führt über Ligandenaustausch mit organischen Halbleiterliganden, deren Molekülorbitale so positioniert sind, dass sie elektronische Kopplung mit den benachbarten Nanokristallen ermöglichen. Diese Strategie der Bildung eines Hybridmaterials, das aus einer großen Anzahl alternierender organischer und

anorganischer Grenzflächen besteht, hat einen zusätzlichen Vorteil in Bezug auf die Effizienz des Ladungstransfers und die Herbeiführung neuer Materialeigenschaften.[110,235] In dieser Arbeit werden die strukturellen, optischen und elektronischen Eigenschaften von dünnen Filmen aus CdSe Nanokristallen und ihre Verbesserung durch Kopplung mit organischen Farbstoffmolekülen untersucht.

Der erste Artikel zeigt die im roten Spektralbereich auftretende Verbesserung der lasergestützten Ein/Aus-Eigenschaften der CdSe Nanokristalle, die mit Zn4APc-Farbstoffmolekülen gekoppelt sind. Bemerkenswert ist, dass das gekoppelte System einen Anstieg des Photostroms im nahen Infrarotbereich um ~4 Größenordnungen zeigt, während die nicht funktionalisierten CdSe/I- Nanokristalle ein schlechtes Ansprechverhalten und einen langsameren Anstieg des Photostroms zeigen, was auf Oberflächen-Fallenzustände hindeutet. Transiente Absorptionsmessungen zeigen, dass das Hybridmaterial einen Ladungstransfer vom Farbstoffmolekül auf die CdSe Nanokristalle in 5 ps aufweist. Das Hybridsystem veranschaulicht auch einen schnellen Anstieg des Photostroms bei 779 nm Anregung, wie er durch die zeitaufgelösten Photostrommessungen dargestellt wird.

Der zweite Artikel zeigt die Kopplung von CdSe Nanokristallen mit dem Arylenethylenderivat (AE **1**). Langkettige organische π-Linker zeigen aggregationsinduzierte Emission in dünnen Filmen oder hochkonzentrierten Umgebungen. Das Hybridmaterial zeigt ein Zweibanden-Fluoreszenzverhalten bestehend aus der Bandkantenemission der CdSe Nanokristalle und der aggregationsinduzierten Emission. Die kontinuierliche Messung der Photolumineszenz im Gleichgewichtszustand zeigt, dass die Intensität dieser beiden Banden (Emission der Nanokristalle und aggregationsinduzierter Emissionspeak) bei Raumtemperatur zufällig antikorreliert variiert, d.h. die Intensität eines Peaks nimmt bei gleichzeitiger Intensitätsabnahme des anderen Peaks zu. Diese Intensitätsänderung ist mit einer Verschiebung der aggregationsinduzierten Emissionsbande um ~10 nm verbunden. Der aus dem Fluoreszenzspektrum des Hybridfilms extrahierte Raman-Peak zeigte keine Anzeichen einer chemischen Umwandlung des Moleküls während der Intensitätsvariation des dünnen Films. Die Intensitätsvariation verhielt sich bei tiefer Temperatur und etwa eine Größenordnung niedrigerer Laserleistung periodisch. Es wurde beobachtet, dass die Zeitdauer der Oszillation der "ein-aus"-Fluoreszenz von der Laserleistung abhängig war. Wir führten die Fluoreszenzvariationen auf die strukturelle Änderung in der Ausrichtung der Linkermoleküle zurück, die den Energietransfer zwischen Nanokristallen und Linker bewirkt.

Der dritte Artikel untersucht die strukturellen Eigenschaften von CdSe Nanokristallen in Wurtzit- und Zinkblende-Struktur. NMR-Spektroskopie zeigte die Menge an freiem und gebundenem Linker in der Lösung für die Selbstassemblierung von Wurtzit Nanokristallen. Interessanterweise zeigte die Selbstassemblierung der Nanokristalle eine Abhängigkeit von der Verfügbarkeit des freien Linkers in Lösung. Eine Zunahme des freien Linkers zeigte eine 10-21%ige Zunahme des Abstands zum nächsten Nachbarn in der Dünnschicht der Nanokristalle und eine etwa 10%ige Zunahme der Gitterkonstante der selbstorganisierten Teilchen.

Für zukünftige Bestrebungen auf diesem Gebiet könnte man die Kopplung von CdSe Nanokristallen mit verschiedenen OSC-Linkern untersuchen, um die Mobilität des elektrischen Geräts und den mit unterschiedlicher Anregungsenergie induzierten Photostrom weiter zu verbessern. Zeitaufgelöste Photostrommessungen dieser hybriden NCs haben gezeigt, dass diese Hybridmaterialien ein optisches Schalten in der Größenordnung von einigen zehn bis hundert Nanosekunden anzeigen können. Zum besseren Verständnis des Systems könnte eine systematischere Studie durchgeführt werden, die eine detaillierte Analyse von Photostrommessungen beinhaltet und gleichzeitig den Einfluss von Parametern wie der Temperatur untersucht. Die optischen Eigenschaften von Nanokristallen, die mit Arylenethylenderivaten gekoppelt sind, zeigen ein neues Fluoreszenzverhalten; daher könnten sich zukünftige Arbeiten auf diesem Gebiet darauf konzentrieren, zu untersuchen, ob ähnliche Effekte auch bei anderen kreuzförmigen Linkern auftreten. Wenn ja, wie wirkt sich die Temperatur auf die optischen Eigenschaften aus? Außerdem könnte die Fluoreszenzverstärkung für verschiedene Banden mit Hilfe eines durchstimmbaren Resonators untersucht werden.

(*Sprachberaterin: Christine A. Schedel*)

Appendix A

Supporting Information

A Fast, Infrared-Active Optical Transistor Based on Dye-Sensitized CdSe Nanocrystals

Krishan Kumar[1], Quan Liu[1,2], Jonas Hiller[1], Christine Schedel[1], Andre Maier,[1] Alfred Meixner[1,3], Kai Braun[1], Jannika Lauth[4,5], Marcus Scheele[1,3,]*

[1] Institute for Physical and Theoretical Chemistry, University of Tübingen, Auf der Morgenstelle 18, 72076 Tübingen, Germany.

[2] Charles Delaunay Institute, CNRS Light, nanomaterials, nanotechnologies (L2n, former "LNIO") University of Technology of Troyes, 12 rue Marie Curie - CS 42060, 10004 Troyes Cedex, France

[3] Center for Light-Matter Interaction, Sensors & Analytics LISA+, University of Tübingen, Auf der Morgenstelle 15, 72076 Tübingen, Germany

[4] Institute for Physical Chemistry and Electrochemistry, Universität Hannover, Callinstr. 3A, 30167, Hannover, Germany

[5] Cluster of Excellence PhoenixD (Photonics, Optics, and Engineering – Innovation Across Disciplines), Hannover, Germany.

* Corresponding author, Marcus Scheele, E-mail: marcus.scheele@uni-tuebingen.de

Fig. S1 shows temporal slices of a CdSe/I$^-$/Zn4APc-COIN optical transistor photoexcited at 640 nm near-resonantly to the first excitonic transition of the CdSe NCs and – unlike measurements with a photoexcitation wavelength of ≥ 710 nm - lacking a time-correlation between the decay of bleach feature 1 and 1a and bleach feature 2 in the first 25 ps of the measurement due to a charge transfer mechanism (no rise time in bleach feature 2). The dynamics of the Zn4APc bleaches 1/1a and the CdSe NC bleaches 2 are fitted with a double-

exponential ($\tau_1 = 3.7 \pm 2.3$ ps, $\tau_2 = 74 \pm 17$ ps for the rather noisy bleach feature 1 and $\tau_1 = 1.4 \pm 0.1$ ps, $\tau_2 = 34 \pm 2.0$ ps for the nicely resolved bleach feature 1a, $\tau_1 = 4.6 \pm 0.2$ ps, $\tau_2 = 71 \pm 2.5$ ps for bleach feature 2).

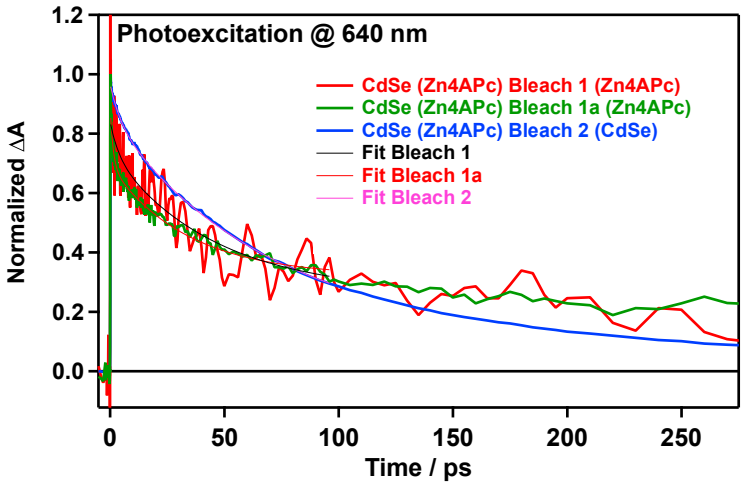

Figure A-S1 Decay of Davydov-split bleach features 1 and 1a of the Zn4APc and decay of bleach feature 2 due to direct photoexcitation of the CdSe NCs.

By comparing the time constants of the decay in bleach feature 1 and 1a at different photoexcitation wavelengths with the rise of bleach feature 2 in the first 25 ps of the measurement, we find that at photoexcitation wavelengths of 800 nm (close to the wavelength of the photocurrent measurements), particularly photoexcited electrons from the energetically lower lying S_{11} level of the Zn4APc molecule seem to be transferred to the CdSe S_{1e} level, while at 710 nm, electrons from the S_{12} transition in the Zn4APc molecule seem to be preferred for transfer to the CdSe S_{1e} level (see **Fig. S2** and **S3** respectively). **Fig. S2** shows almost the same time constants of a biexponential fit for the decay of the directly photobleached Davydov-split $S_0 \rightarrow S_{11}$ transition (bleach feature 1, $\tau_1 = 330$ fs $\pm$ 25 fs, $\tau_2 = 5.8 \pm 0.2$ ps) photoexcited at 800 nm and the time corelated rise of bleach feature 2 due to charge transfer into the CdSe $1S_e$ level (bleach feature 2, $\tau_1 = 300 \pm 34$ fs, $\tau_2 = 4.7 \pm 0.1$ ps). Time constants for the decay of the $S_0 \rightarrow S_{12}$ transition in bleach feature 1a are $\tau_1 = 640$ fs $\pm$ 110 fs, $\tau_2 = 6.5 \pm 0.4$ ps.

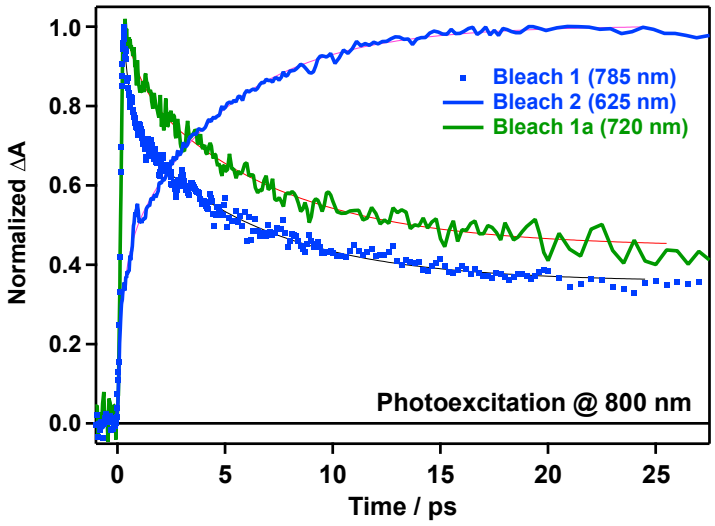

Figure A-S2 Decay of bleach feature 1 at 785 nm when photoexciting CdSe/I-/Zn4APc-COIN at 800 nm (Davydov-split $S_0 \rightarrow S_{11}$ transition) and time correlated ultrafast rise (before decay at longer times) of CdSe-associated bleach feature 2.

Photoexciting the sample at 710 nm close to the $S_0 \rightarrow S_{12}$ transition of the Zn4APc leads to the time constants of bleach feature 1a ($\tau_1 = 550$ fs $\pm$ 26 fs, $\tau_2 = 4.8 \pm 0.3$ ps) being almost the same as in the rise of bleach feature 2 ($\tau_1 = 480 \pm 24$ fs, $\tau_2 = 3.7 \pm 0.1$ ps), whereas at 710 nm the $S_0 \rightarrow S_{11}$ transition decays faster ($\tau_1 = 190 \pm 45$ fs, $\tau_2 = 5.0 \pm 0.5$ ps).

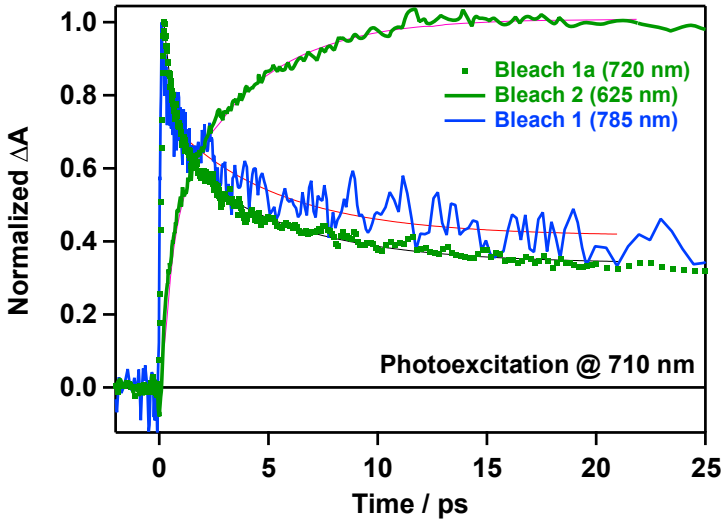

Figure A-S3 Decay of bleach feature 1a at 720 nm when photoexciting CdSe/I-/Zn4APc-COIN at 710 nm (Davydov-split $S_0 \rightarrow S_{12}$ transition) time correlated ultrafast rise (before decay at longer times) of CdSe-associated bleach feature 2 as discussed above.

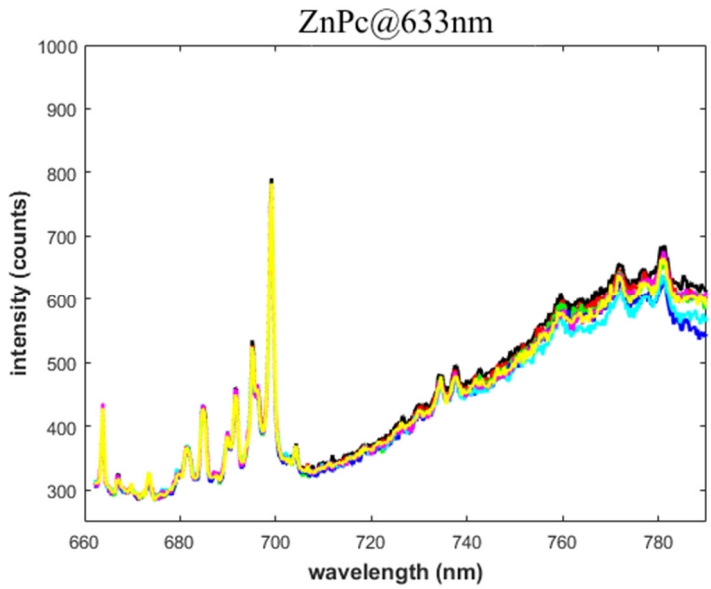

Figure A-S4 Solid-state fluorescence of a thin film of pure Zn4APc on quartz under 633 nm excitation. The sharp lines are due to Raman modes. We attribute the broad band with a maximum at 780 nm to the $S_1 \rightarrow S_0$ transition and note the generally very small quantum yield (< 1 %) of this transition for this molecule in accordance with an earlier report.[236]

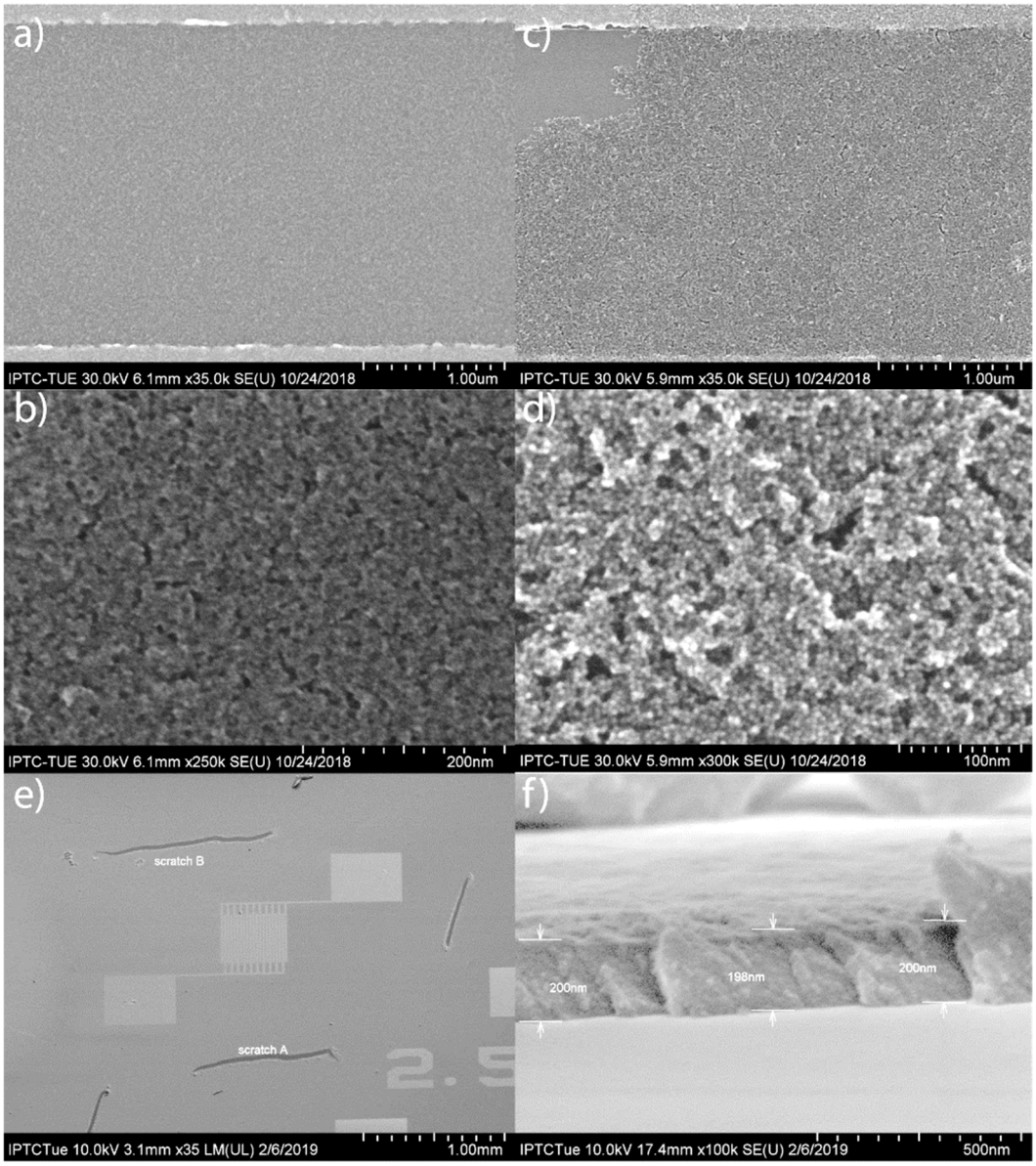

Figure A-S5 Scanning electron micrographs of typical CdSe NC films used in this work. a)/b) CdSe NCs capped with I^- at two different magnifications. The lighter regions at the top and bottom of a) are the gold contacts of the channel. c)/d) CdSe NCs capped with I^- after ligand excahnge with Zn4APc at two different magnifications. e) Low-magnification microgaph showing a dense film with several intended scratches to determine the height of the film. f) High-magnification micrograph of one of the scratches under a tilt of 85 °. The average height of the film is 200 nm.

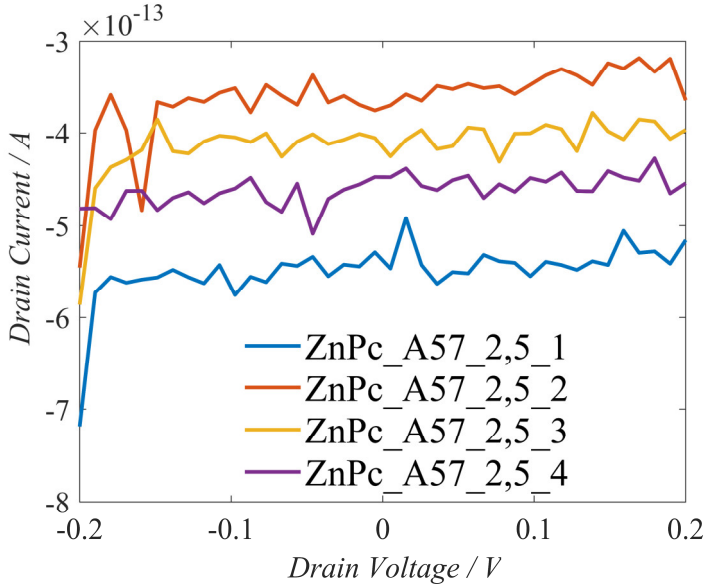

Figure A-S6 Current/voltage transport charaterization of four different channels (length: 2.5 µm) of pure Zn4APc films without any CdSe NCs. The current range of 10^{-13} A reflects the noise level of the measurement set-up. In combination with the essentially flat I/V behavior, this indicates insulating behavior of the Zn4APc film.

Appendix B

Supporting Information

Periodic Fluorescence Variations of CdSe Quantum Dots Coupled to Aryleneethynylenes with Aggregation Induced Emission

Krishan Kumar[1], Jonas Hiller[1], Markus Bender[2], Saeed Nosrati[1], Quan Liu[1,3], Frank Wackenhut[1], Alfred J. Meixner[1,4], Kai Braun[1], Uwe H. F. Bunz[2], Marcus Scheele[1,4]

[1] Institute for Physical and Theoretical Chemistry, University of Tübingen, Auf der Morgenstelle 18, 72076 Tübingen, Germany.

[2] Organisch-Chemisches Institut and Centre for Advanced Materials, Ruprecht-Karls-Universität Heidelberg, Im Neuenheimer Feld 270, 69120 Heidelberg, Germany

[3] Charles Delaunay Institute, CNRS Light, nanomaterials, nanotechnologies (L2n, former "LNIO") University of Technology of Troyes, 12 rue Marie Curie - CS 42060, 10004 Troyes Cedex, France

[4] Center for Light-Matter Interaction, Sensors & Analytics LISA+, University of Tübingen, Auf der Morgenstelle 15, 72076 Tübingen, Germany

AE 1 Synthesis

General Remarks

All reactions requiring exclusion of oxygen and moisture were carried out in dry glassware under a dry and oxygen free nitrogen atmosphere. The addition of solvents or reagents was carried out using nitrogen flushed stainless steel cannulas and plastic syringes. For spectroscopic and analytic characterizations, the following devices were used:

Analytical thin layer chromatography (TLC) was performed on Macherey & Nagel Polygram® SIL G/UV254 precoated plastic sheets. Components were visualized by observation under UV light (254 nm or 365 nm) or in the case of UV-inactive substances by using the suitably coloring solutions. The following coloring solutions were used for the visualization of UV-inactive substances:

$KMnO_4$ solution: 2.0 g $KMnO_4$, 10.0 g K_2CO_3, 0.3 g NaOH, 200 mL distilled water. Cer solution: 10.0 g $Ce(SO_4)_2$, 25 g phosphomolybdic acid hydrate, 1 L distilled water, 50 mL conc. H_2SO_4.

Flash column chromatography was carried out using silica gel S (32 μm-62 μm), purchased from Sigma Aldrich, according to G. Nill, unless otherwise stated.[237] As noted, Celite® 545, coarse, (Fluka) was used for filtration.

Dialysis was carried out using an appropriate length of the commercially available regenerated cellulose tubular membranes: Spectra/Por® Biotech Cellulose Ester (CE) Dialysis Membranes with the following specifications:

Molecular weight cut off:	500-1000 D
Flat width:	31 mm
Vol/cm:	3.1 mL/cm
Diameter in dry state:	20 mm

Unless stated otherwise the equipped tubular membranes were put into excess (~ 10 L) of deionized water and stirred for 5 d by changing the surrounding solvent once every day. The dialysed solution was freeze-dried afterwards.

Melting points (m.p.) were determined in open glass capillaries on a Melting Point Apparatus MEL-TEMP (Electrothermal, Rochford, UK) and are not corrected.

^{1}H NMR NMR spectra were recorded in $CDCl_3$ at room temperature on a Bruker DRX 300 (300 MHz), Bruker Avance III 300 (300 MHz), Bruker Avance III 400 (400 MHz), Bruker Avance III 500 (500 MHz) or Bruker Avance III 600 (600 MHz) spectrometer. The data were interpreted in first order spectra. All spectra were recorded in $CDCl_3$ or D_2O. Chemical shifts are reported in δ units relative to the solvent residual peak ($CHCl_3$ in $CDCl_3$ at δ_H = 7.27 ppm, HDO in D_2O at δ_H = 4.75 ppm or TMS (δ_H = 0.00 ppm).[238] The following abbreviations are used to indicate the signal multiplicity: s (singlet), d (doublet), t (triplet), q (quartet), quin (quintet), sext (sextet), dd (doublet of doublet), dt (doublet of triplet), ddd (doublet of doublet of doublet), etc., br. s (broad signal), m (multiplet), m_c (centered multiplet). Coupling constants (*J*) are given in Hz and refer to H,H-couplings. All NMR spectra were integrated and processed using ACD/Spectrus Processor.

^{13}C NMR spectra were recorded at room temperature on the following spectrometers: Bruker Avance III 400 (100 MHz) or Bruker Avance III 600 (150 MHz). The spectra were recorded in $CDCl_3$. Chemical shifts are reported in δ units relative to the solvent signal: $CDCl_3$ [δ_C = 77.00 ppm (central line of the triplet)] or TMS (δ_c = 0.00 ppm).

High resolution mass spectra (HR-MS) were either recorded on the JEOL JMS-700 (EI^+), Bruker ApexQehybrid 9.4 T FT-ICR-MS (ESI^+) or a Finnigan LCQ (ESI^+) mass spectrometer at the Organisch-Chemisches Institut der Universität Heidelberg.

Elemental Analyses were carried out at the Organisch-Chemisches Institut der Universität Heidelberg.

IR spectra were recorded on a JASCO FT/IR-4100. Substances were applied as a film, solid or in solution. Processing of data was done using the software JASCO Spectra Manager™ II.

Reagents and Solvents

Unless recorded otherwise, solvents were purchased from the chemical store of the Organisch-Chemisches Institut der Universität Heidelberg and distilled prior to use. Absolute solvents were prepared according to standard procedures and stored under argon over

appropriately sized molecular sieve.[239] Absolute THF, Et_2O, toluene, CH_2Cl_2 and MeCN were purchased from Sigma-Aldrich and purified by a solvent purification system (MBraun, MB SPS-800, filter material: MB-KOL-A, MB-KOL-M; catalyst: MB-KOL-C). Chemicals other than solvents were either purchased from the chemical store of the Organisch-Chemisches Institut Universität Heidelberg or from commercial laboratory suppliers unless reported otherwise.

Compounds

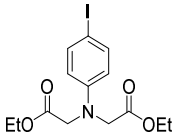

1

Diethyl 2,2'-((4-iodophenyl)azanediyl)diacetate (1): Ethylbromoacetate (15.2 mL, 22.9 g, 137 mmol) was added to a solution of 4-Iodoanilline (10.0 g, 45.7 mmol) and *N*-ethyl-*N*-isopropylpropan-2-amine (40 mL) and was stirred at 120 °C for 4 h. The crude reaction mixture was quenched with H_2O, extracted with ethyl acetate, dried over $MgSO_4$ and evaporated *in vacuo*. The crude product was purified by flash chromatography on silica gel [petroleum ether/ethyl acetate (4/1)] to afford **1** (17.8 g, 99%) as an orange oil. ^{1}H NMR (400 MHz, $CDCl_3$): δ = 6.48-6.38 (m, 4 H), 4.22 (q, *J* = 7.2 Hz, 4 H), 4.10 (s, 4H), 1.28 (t, *J* = 7.2 Hz, 6 H) ppm. ^{13}C NMR (100 MHz, $CDCl_3$): δ = 170.4, 147.6, 137.8, 114.8, 79.8, 61.2, 53.5, 14.2 ppm ppm. IR (cm^{-1}): ν 2979, 2935, 2905, 1730, 1588, 1561, 1495, 1445, 1430, 1370, 1343, 1316, 1294, 1255, 1175, 1113, 1095, 1076, 1053, 1022, 993, 968, 922, 855, 803, 727, 692, 631, 611, 550, 505, 441, 431. HR-MS (ESI^+): *m*/*z* calcd. for $C_{14}H_{19}INO_4^+$ 392.0353 $[M+H]^+$; found. 392.0355. $C_{14}H_{18}INO_4$ (391.03): calcd. C 42.98, H 4.64, N 3.58; found C 43.80, H 4.64, N 3.67.

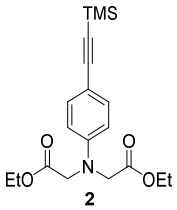

2

Diethyl 2,2'-((4-((trimethylsilyl)ethynyl)phenyl)azanediyl)diacetate (2): 1 (12.0 g, 30.7 mmol) was dissolved in THF/NEt_3 (2:1, 60 mL/30 mL) and degassed for 30 min with a

stream of nitrogen. TMS-acetylene (5.68 mL, 3.92 g, 39.9 mmol), $Pd(PPh_3)_2Cl_2$ (393 mg, 613 µmol) and CuI (234 mg, 1.23 mmol) were added and the mixture was stirred under nitrogen at 50 °C for 48 h until TLC monitoring showed complete conversion. The reaction mixture was filtered over a pad of silica gel and evaporated *in vacuo*. The crude product was purified by flash chromatography on silica gel [petroleum ether/ethyl acetate (6/1)] to afford **2** (6.05 g, 68%) as a yellow solid (m. p. 53-55 °C). ^{1}H NMR (300 MHz, $CDCl_3$): δ = 7.36-7.30 (m, 2 H), 6.55-6.50 (m, 2 H), 4.22 (q, *J* = 7.14 Hz, 4 H), 4.13 (s, 4 H), 1.28 (t, *J* = 7.14 Hz, 6 H), 0.23 (s, 9 H) ppm. ^{13}C NMR (75 MHz, $CDCl_3$): δ = 170.4, 147.9, 133.3, 112.4, 112.0, 105.8, 91.9, 61.3, 53.4, 14.2, 0.1 ppm. IR (cm^{-1}): ν 2979, 2913, 2148, 1745, 1725, 1605, 1516, 1476, 1444, 1416, 1371, 1349, 1302, 1280, 1247, 1220, 1180, 1117, 1063, 1030, 968, 936, 858, 839, 820, 762, 737, 703, 650, 637, 599, 580, 534, 471, 449. HR-MS (ESI^+): *m*/*z* calcd. for $C_{19}H_{28}NO_4Si^+$ 362.1782 $[M+H]^+$; found 362.1784. $C_{19}H_{27}NO_4Si$ (391.03): calcd. C 63.13, H 7.53, N 3.87; found C 63.24, H 7.62, N 3.76.

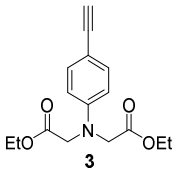

3

Ethyl 2-(2,5-diethynyl-4-methoxyphenoxy)acetate (**3**): **2** (6.00 g, 16.6 mmol) was dissolved in THF (50 mL), placed in an ice bath and degassed for 15 min with a stream of nitrogen. TBAF (1M in THF, 18.4 mL) was added and the mixture was stirred for 10 min. The reaction mixture was quenched with SiO_2, filtered and evaporated *in vacuo*. The crude product was purified by flash chromatography on silica gel [(petroleum ether/ethyl acetate (6/1 → 1/1)] to afford **3** (2.54 g, 52%) as a light yellow/green oil. ^{1}H NMR (300 MHz, $CDCl_3$): δ = 7.39-7.33 (m, 2 H), 6.58-6.51 (m, 2 H), 4.23 (q, *J* = 7.14 Hz, 4 H), 4.14 (s, 4 H), 2.97 (s, 1 H), 1.28 (t, *J* = 7.14 Hz, 6 H) ppm. ^{13}C NMR (75 MHz, $CDCl_3$): δ = 170.4, 148.0, 133.4, 112.1, 111.3, 84.2, 75.3, 61.3, 53.4, 14.2 ppm. IR (cm^{-1}): ν 3280, 2981, 2937, 2101, 1731, 1607, 1557, 1515, 1446, 1388, 1371, 1343, 1324, 1298, 1257, 1175, 1114, 1095, 1056, 1022, 968, 932, 856, 816, 715, 646, 591, 533, 454, 438, 405. HR-MS (ESI^+): *m*/*z* calcd. For $C_{16}H_{20}NO_4^+$ 290.1387 $[M+H]^+$; found 290.1388. $C_{16}H_{19}NO_4$ (289.13): calcd. C 66.42, H 6.62, N 4.84; found C 66.23, H 6.78, N 4.68.

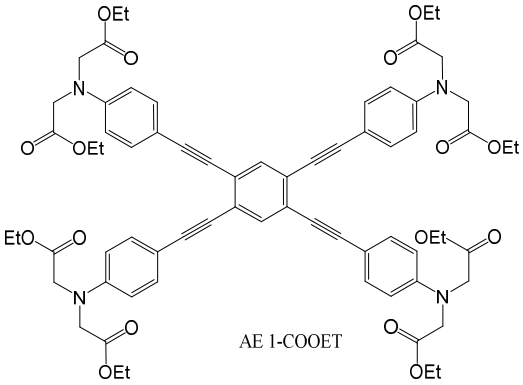

Octaethyl 2,2',2'',2''',2'''',2''''',2'''''',2'''''''-(((benzene-1,2,4,5-tetrayltetrakis(ethyne-2,1-diyl))tetrakis(benzene-4,1-diyl))tetrakis(azanetriyl))octaacetate (AE 1-COOET): 1,2,4,5-Tetraiodobenzene[240] (320 mg, 550 µmol) and **3** (686 mg, 2.31 mmol) were dissolved in degassed THF/NEt_3 (1:1, 1.5 mL/1.5 mL). $Pd(PPh_3)_2Cl_2$ (39 mg, 55 µmol) and CuI (11 mg, 55 µmol) was added and the mixture was stirred under nitrogen at 60 °C for 24 h. The reaction mixture was filtered over a pad of silica gel and evaporated *in vacuo*. The crude product was purified by flash chromatography on silica gel [petroleum ether/ethyl acetate (1/1)] to afford **AE 1-COOET** (398 mg, 59%) as a red film. ^{1}H NMR (600 MHz, $CDCl_3$): δ = 7.64 (s, 2 H), 7.44-7.41 (m, 8 H), 6.61-6.58 (m, 8 H), 4.22 (q, *J* = 7.15 Hz, 18 H), 4.17 (s, 16 H), 1.30 (t, *J* = 7.15 Hz, 24 H) ppm. ^{13}C NMR (150 MHz, $CDCl_3$): δ = 170.5, 147.9, 134.4, 133.0, 124.8, 112.5, 112.3, 95.6, 86.6, 61.3, 53.4, 14.2 ppm. IR (cm^{-1}): ν 2979, 2935, 2197, 1730, 1604, 1556, 1520, 1444, 1386, 1370, 1343, 1296, 1257, 1174, 1135, 1094, 1057, 1020, 967, 855, 813, 727, 647, 531, 467, 441. HR-MS (ESI^+): *m/z* calcd. for $C_{70}H_{74}N_4NaO_{16}^+$ 1249.4992 $[M+Na]^+$; found 1249.5004. $C_{70}H_{74}N_4O_{16}$ (1227.37): calcd. C, 68.50; H, 6.08; N, 4.56; found C 67.85, H 6.51, N 4.11.

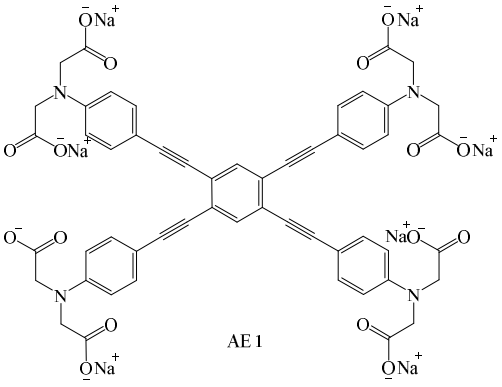

Sodium 2,2',2'',2''',2'''',2''''',2'''''',2'''''''-(((benzene-1,2,4,5-tetrayltetrakis(ethyne-2,1-diyl))tetrakis(benzene-4,1-diyl))tetrakis(azanetriyl))octaacetate (AE 1): **AE 1-COOET**

(316 mg, 257 mmol) was dissolved in MeOH/H_2O (1:1, 10 mL/10 mL) and NaOH (515 mg, 12.9 mmol) was added. The resulting mixture was stirred at 70°C for 2 d. The solvent was evaporated *in vacuo.* The residue was dissolved in H_2O and filtrated. The resulting solution was adjusted to pH 7 and dialyzed against DI H_2O for 5 d. After filtration and freeze-drying the title compound **AE 1** was afforded as brown fluffy solid (250 mg, 97%). ^{1}H NMR (600 MHz, D_2O): δ = 7.71-7.69 (m, 2 H), 7.48-7.44 (m, 8 H), 6.58-6.54 (m, 8 H), 3.93 (m, 16H) ppm. Due to low solubility, ^{13}C NMR spectrum could not be obtained. IR (cm^{-1}): ν 3589, 3327, 3171, 3037, 2928, 2650, 2193, 1577, 1516, 1457, 1381, 1298, 1232, 1176, 1134, 972, 906, 817, 695, 610, 515, 456, 43

Selected 1H-NMR Spectra

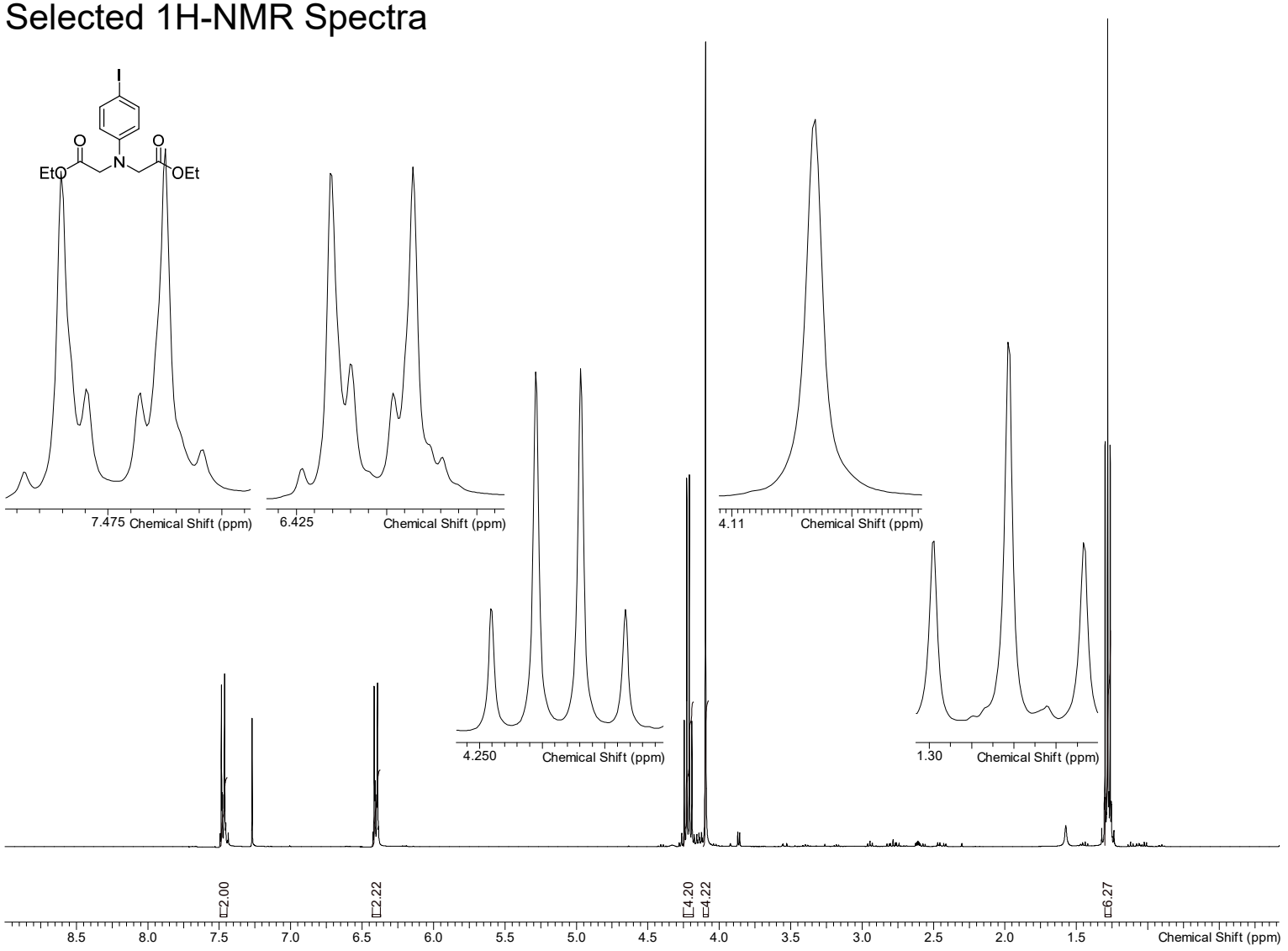

Current Data Parameters

NAME	c180320ubmb.63
EXPNO	2
PROCNO	1

F2 - Acquisition Parameters

Date	20180321
Time	8.17
INSTRUM	spect
PROBHD	Z130030_0004
PULPROG	zg30
TD	65536
SOLVENT	$CDCl_3$
NS	128
DS	2
SWH	12019.230 Hz
FIDRES	0.366798 Hz
AQ	2.7262976 sec
RG	181
DW	41.600 usec
DE	10.00 usec
TE	295.0 K
D1	0.50000000 sec
TD0	16

====== CHANNEL f1 =====

NUC1	1H
P1	11.50 usec
PLW1	10.00000000 W
SFO1	400.3320009 MHz

F2 - Processing parameters

SI	65536
SF	400.3300377 MHz
WDW	EM
SSB	0
LB	0.30 Hz
GB	0
PC	1.00

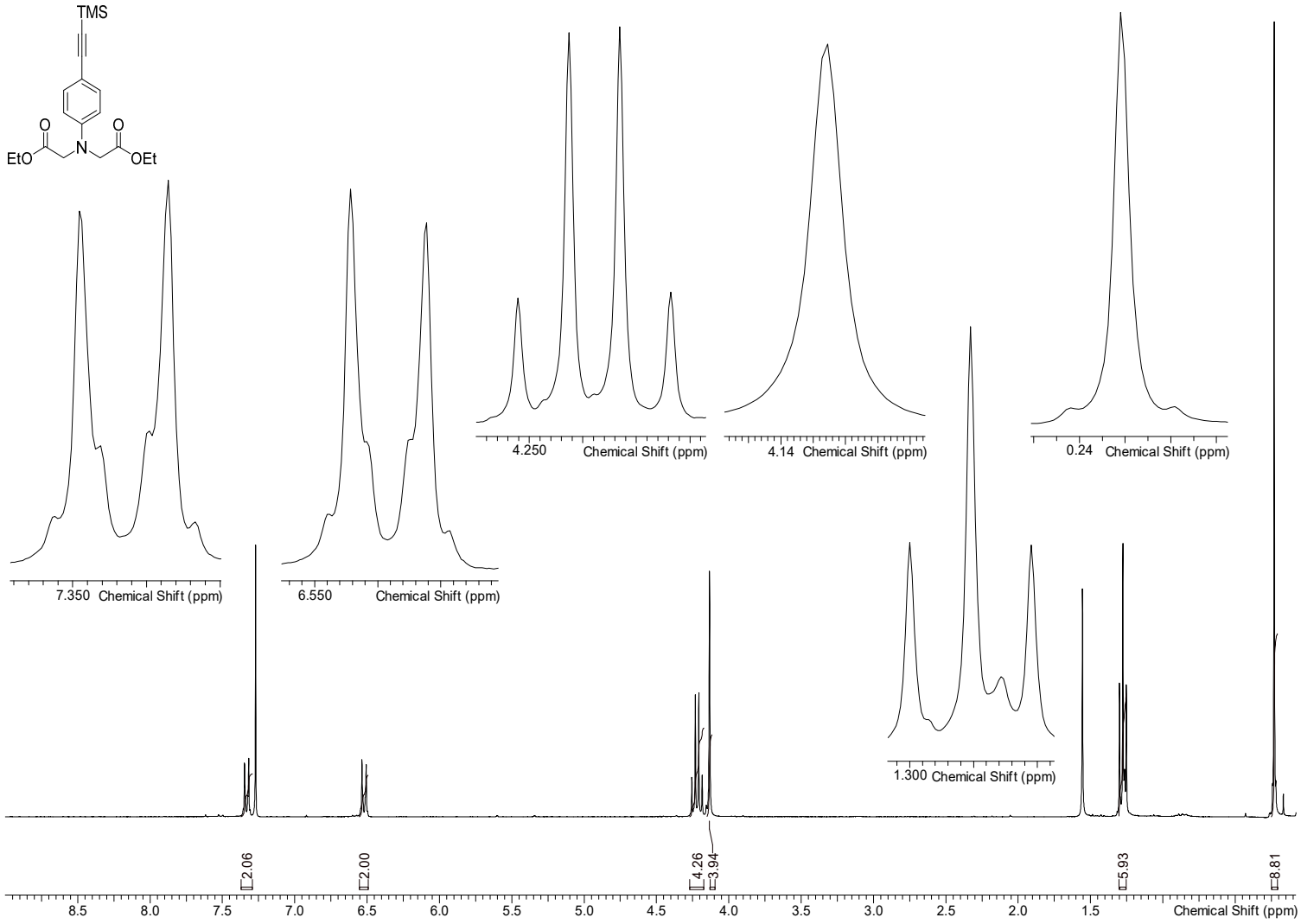

Current Data Parameters

NAME	b180323ubmb 67
EXPNO	2
PROCNO	1

F2 - Acquisition Parameters

Date	20180324
Time	18.29
INSTRUM	spect
PROBHD	5 mm PATXO 31P
PULPROG	zg30
TD	65536
SOLVENT	$CDCl_3$
NS	128
DS	2
SWH	8992.806 Hz
FIDRES	0.137219 Hz
AQ	3.6438515 sec
RG	574.7
DW	55.600 usec
DE	6.00 usec
TE	298.2 K
D1	0.10000000 sec
TD0	16

====== CHANNEL f1 =====

NUC1	1H
P1	11.50 usec
PL1	-3.00 dB
SFO1	300.1315007 MHz

F2 - Processing parameters

SI	32768
SF	300.1315007 MHz
WDW	EM
SSB	0
LB	0.30 Hz
GB	0
PC	1.00

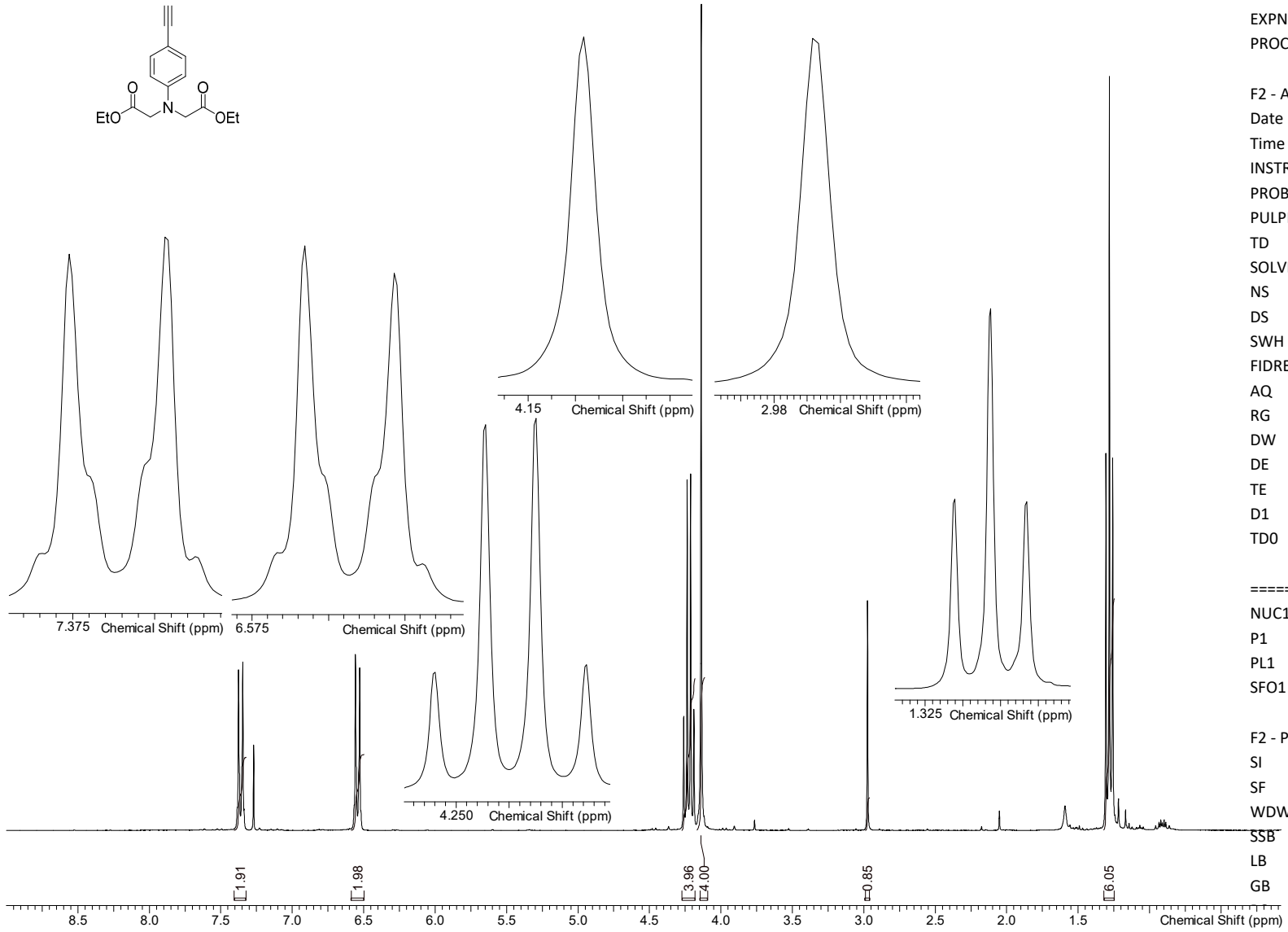

Current Data Parameters

NAME	b180323ubmb.68
EXPNO	2
PROCNO	1

F2 - Acquisition Parameters

Date	20180326
Time	7.57
INSTRUM	spect
PROBHD	5 mm PATXO 31P
PULPROG	zg30
TD	65536
SOLVENT	$CDCl_3$
NS	128
DS	2
SWH	8992.806 Hz
FIDRES	0.137219 Hz
AQ	3.6438515 sec
RG	322.5
DW	55.600 usec
DE	6.00 usec
TE	298.2 K
D1	0.10000000 sec
TD0	16

====== CHANNEL f1 =====

NUC1	1H
P1	11.50 usec
PL1	-3.00 dB
SFO1	300.1315007 MHz

F2 - Processing parameters

SI	32768
SF	300.1300268 MHz
WDW	EM
SSB	0
LB	0.30 Hz
GB	0
	1.00

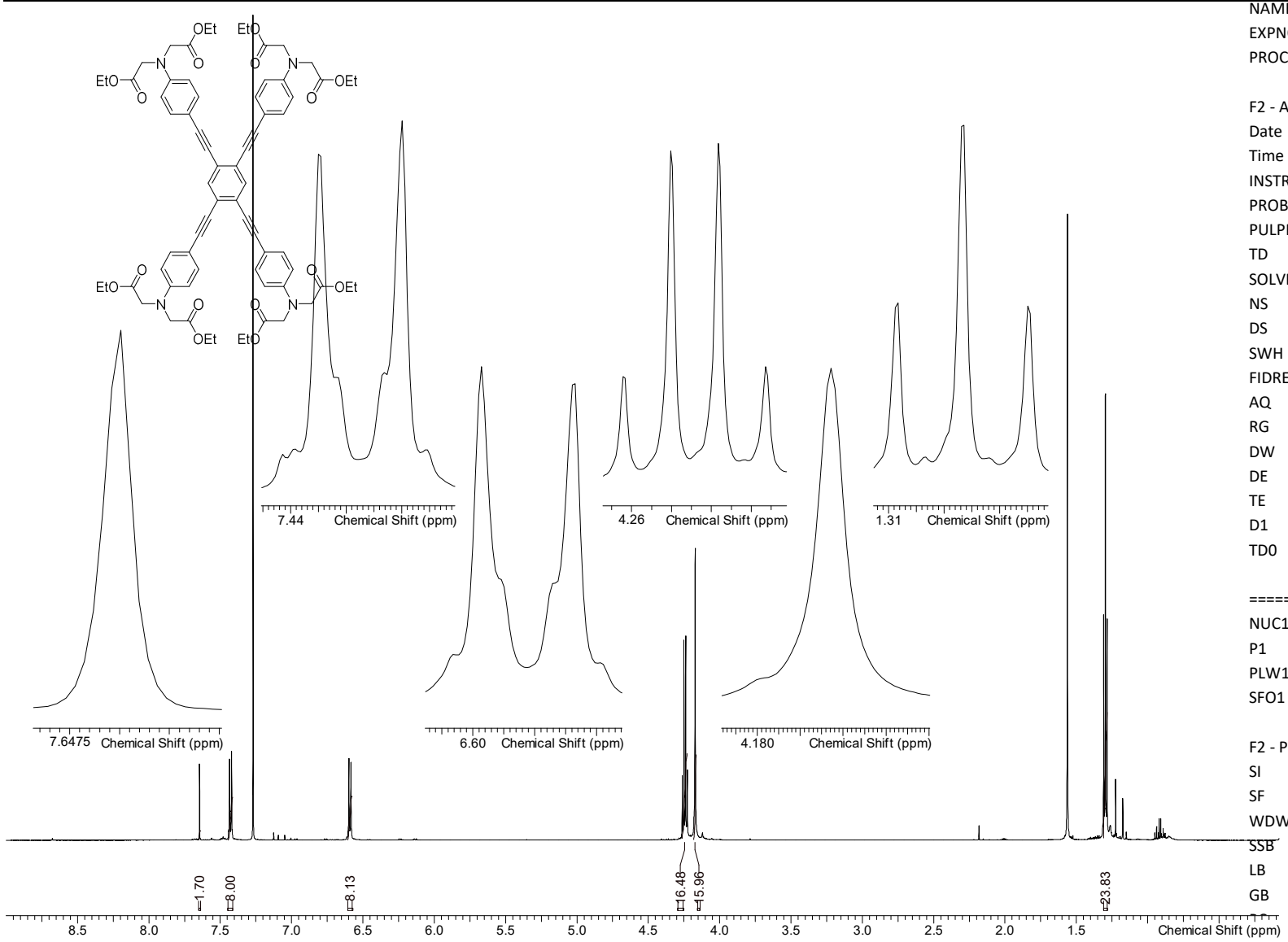

Current Data Parameters

NAME	e180329ubmb.71
EXPNO	2
PROCNO	1

F2 - Acquisition Parameters

Date	20180331
Time	16.54
INSTRUM	spect
PROBHD	Z132808_0001 (
PULPROG	zg30
TD	131072
SOLVENT	$CDCl_3$
NS	128
DS	2
SWH	18028.846 Hz
FIDRES	0.275098 Hz
AQ	3.6350634 sec
RG	15.35
DW	27.733 usec
DE	12.00 usec
TE	295.0 K
D1	0.10000000 sec
TD0	16

====== CHANNEL f1 =====

NUC1	1H
P1	7.63 usec
PLW1	7.5000000 W
SFO1	600.2468302 MHz

F2 - Processing parameters

SI	65536
SF	600.2438290 MHz
WDW	EM
SSB	0
LB	0.30 Hz
GB	0
	1.00

CdSe NCs synthesis

Chemicals Used

Chemicals used were cadmium oxide (CdO, 99.99%, Aldrich), oleicacid (OA, 90%, Aldrich), trioctylphosphine (TOP, 97%, Abcr), trioctylphosphine oxide (TOPO, 99%, Aldrich), hexadecylamine(HDA, 90%, Aldrich), 1-octadecene (ODE, 90%, Acros Organics), selenium pellet (Se, 99.999%, Aldrich), ammonium iodide (99.999%,Aldrich), N-methylformamide (NMF, 99%, Aldrich), hexane (ExtraDry, 96%, Acros Organics), ethanol (Extra Dry, 99.5%, AcrosOrganics), acetone (Extra Dry, 99.8%, Acros Organics), dimethylsulfoxide (DMSO, 99.7%, Acros Organics), and acetonitrile (ExtraDry, 99.9%, Acros Organics).

All chemicals, except those used in CdSe NC synthesis, were stored and used inside a nitrogen-filled glovebox. All sample preparations for electrical or fluorescence measurements were carried out in a nitrogen-filled glovebox. The samples were inserted into probe station for low temperature photocurrent measurements using an air tight arm sealed inside the glove box. Samples were kept under low pressure for at least 2 h before starting any measurements.

CdSe NCs and Device Preparation

Wurtzite CdSe NCs having ~5 nm size were synthesized using a literature reported synthesis.[62,70] As synthesized NCs were dispersed in hexane. CdSe NCs 5 mL, ~10 mg/mL were taken for ligand exchange with 300 µL of a 1 M solution of NH_4I in NMF further diluted using 2.7 mL acetone. This biphasic mixture was stirred until the NCs change their phase, then centrifuged and washed using excess of acetone. CdSe/I^- thus obtained were dispersed in NMF having 60–100 mg/mL concentration. For device preparation we used commercially available gold patterned Si/SiO_2 with 230 nm thick dielectric layer and $2.5\ \mu m \times 1\ cm$ channel provided by the Fraunhofer Institute for Photonic Microsystems, Dresden, Germany. In a typical device preparation, 70 µL of CdSe/I^- NCs were dropped on an FET substrate, mixed with 30 µL of AE **1** solution in NMF with a concentration of roughly 1 mg/mL and kept undisturbed for 6 h. The still wet mixture of CdSe/I^-/AE **1** was then spun off at 30 rps for 1 min. Then the substrate was washed with acetonitrile multiple times and annealed at 190° C for 35 min. A similar procedure was followed for preparing samples on coverslips for fluorescence measurements.

Electrical and Optical Measurements

Electrical measurements were carried out under nitrogen by using a *Keithley 2634B source meter*. The charge-carrier mobility was extracted using the gradual channel approximation in the linear regime. The error in the mobility (S) was calculated using the standard deviation error in the slope of I_d vs V_g curve at 5 V source-drain voltage:

$$S = \sqrt{\frac{1}{N-1}\sum_{i=1}^{N}\left|A_i - \overline{A}\right|}; \qquad \overline{A} = \frac{1}{N}\sum_{i=1}^{N} A_i$$

Here, A is the slope from N measurements with the mean value $\overline{A}$.

Absorption measurements were acquired using a *Carry 5000 UV-Vis-NIR* spectrophotometer on a thin glass coverslip or in methanol as stated in the text. Photocurrent low temperature measurements were recorded using a *CRX-6.5K (Lake shore Desert)* probe station operated under low pressure $5 \times 10^6\ mbar$ and a *Keithley 2634B source meter*. Samples were illuminated using a 408 nm *LP405-SF10* laser diode manufactured by *Thorlabs* having theoretical maximum output power 11.5 – 30 mW. This output power decreases orders of magnitude due to beam decollimation, scattering and inefficient coupling of optical fiber when calibrated using a test sample comes out to be 10 – 18 μW.

Room Temperature Fluorescence Measurements

$12 \times 12\ mm$ glass coverslips were cleaned by submerging in a chromic acid cleaning solution for several hours followed by three subsequent washing steps with triple distilled water and spectroscopy grade methanol. Fluorescence samples were then prepared on these coverslips using the drop casting method described above. The film was washed with acetonitrile and annealed at 190 °C before taking any measurements.

The room temperature steady-state photoluminescence spectral measurements as well as photoluminescence and scattering image acquisition were carried out using a homebuilt inverted confocal laser scanning microscope.[109] A 488nm *TOPTICA Photonics* iBeam smart diode laser with a gaussian intensity profile, operated in continuous wave mode was employed as the light source. The laser intensity in the diffraction limited focus at maximum laser power

is estimated to be $10^7\ W/cm^2$operated at roughly 30-60% of maximum power. Focusing of the laser on the sample and the subsequent collection of reflected, as well as scattered and emitted light was achieved through an oil immersion objective (NA = 1.25). The spectral data was recorded using an *Acton SpectraPro 2300i* spectrometer with a grating of 300/mm and a detector temperature of -45 °C. Photoluminescence and scattering images were acquired by scanning the area of interest while utilizing two separate avalanche photodiodes (APDs) as detectors. The exclusion of atmospheric oxygen was achieved by nearly completely enclosing the upper part of the sample holder and passing a constant flow of nitrogen through this apparatus.

Low Temperature Fluorescence Measurements

Low temperature fluorescence was measured using a home-built confocal microscope mounted on a damped optical table and a standard microscope objective (60X DIN Achromatic objective, NA = 0.85, Edmund Optics) located inside a cryostat (SVT-200, Janis). A Cernox temperature sensor (CX-1030-SD-HT 0.3L) was positioned close to the sample to measure the temperature by a LakeShore Model 336 temperature controller. The sample holder was mounted on the scan stage. Attocube systems linear stages (ANPx320 and ANPz101eXT) and scanners (ANSxy100lr and ANSz100lr) were used to scan and position the sample.

A continuous wave 488 nm laser diode (OBIS LS 20 mW, Coherent Inc) was used to excite the sample. The excitation intensity of the laser was measured between 0.35 mW and 4.80 mW before entering into the cryostat. The excitation light was then aligned into the objective (60X DIN Achromatic air objective, Edmund Optics) to get an optimal focus. The excitation intensity in the focus was between 5.5×10^4 and $7.52 \times 10^5\ W/c\mathrm{m}^2$.[241]

The collected fluorescence signal was passed through the dichroic mirror and a longpass filter (488 LP Edge Basic, AHF Analysentechnik). It was detected by a single-photon counting avalanche photodiode (APD, COUNT-100C, Laser Components). Fluorescence spectra were also acquired with integration times of one second by a Shamrock 500 spectrograph in combination with an Andor Newton back illuminated deep depleted CCD camera (DU920PPR-DD). Further details for low temperature confocal imaging and spectroscopy setup can be found elsewhere.[242]

Time-resolved photoluminescence decay measurements

Time-resolved photoluminescence spectra were measured with a home built scanning confocal microscope.[243] The sample was fixed on a piezo stage (Physik Instrumente) via magnets to avoid movement. A constant nitrogen flow was applied to maintain an inert atmosphere and avoid oxidation of the sample. To avoid bleaching, the lifetime was always measured before a fluorescence measurement.

A linearly polarized continuous wave laser (488 nm,0.33 mW measured before objective lens) was focused on the sample by a high numerical aperture (NA=1.46) oil objective, the fluorescence was collected by the same objective and sent to a spectrometer (Acton SP-2500i, Princeton Instruments). For lifetime measurement, the laser was operated in the pulsed mode ($5.3 \times 10^3\ W/cm^2, 20\ MHz$). The signal was sent to a single photon avalanche photodiode (APD), connected to a time-correlated Single Photon Counting module (TCSP, HydraHarp 400). Decay curves were fitted and analysed by SymPhoTime 64.

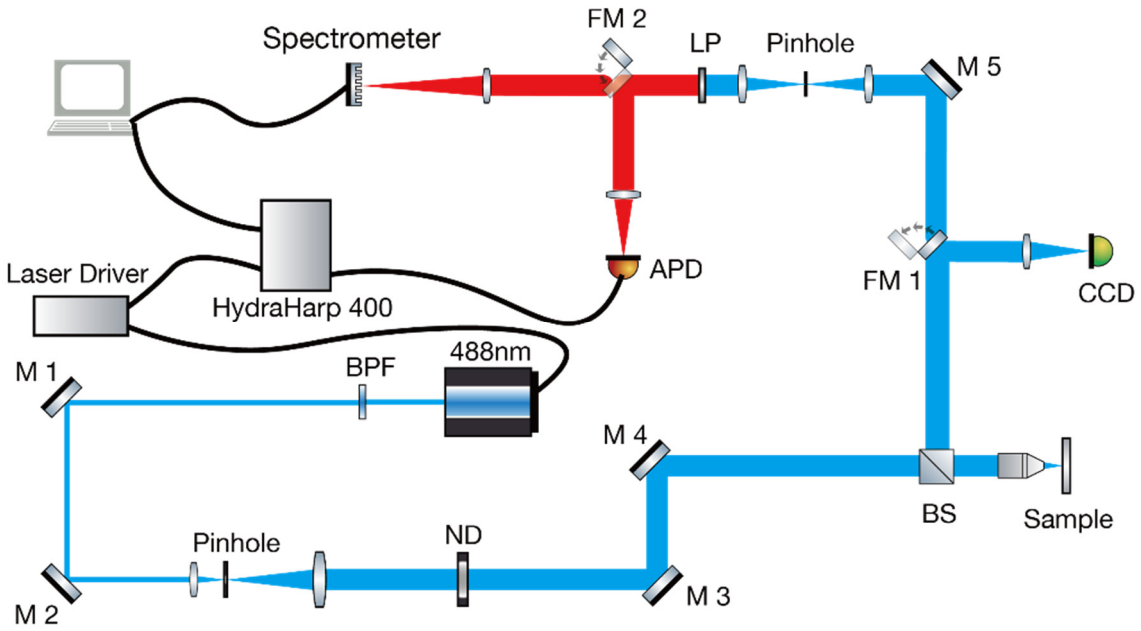

Scheme S1 Sketch of optical setup for fluorescence lifetime measurement. Abbreviations FM: Flip mirror, LP: Long-pass filter, M: Mirror, BPE: Band pass filter, ND: neutral-density filter, BS: Beam split.

Supplementary Figures

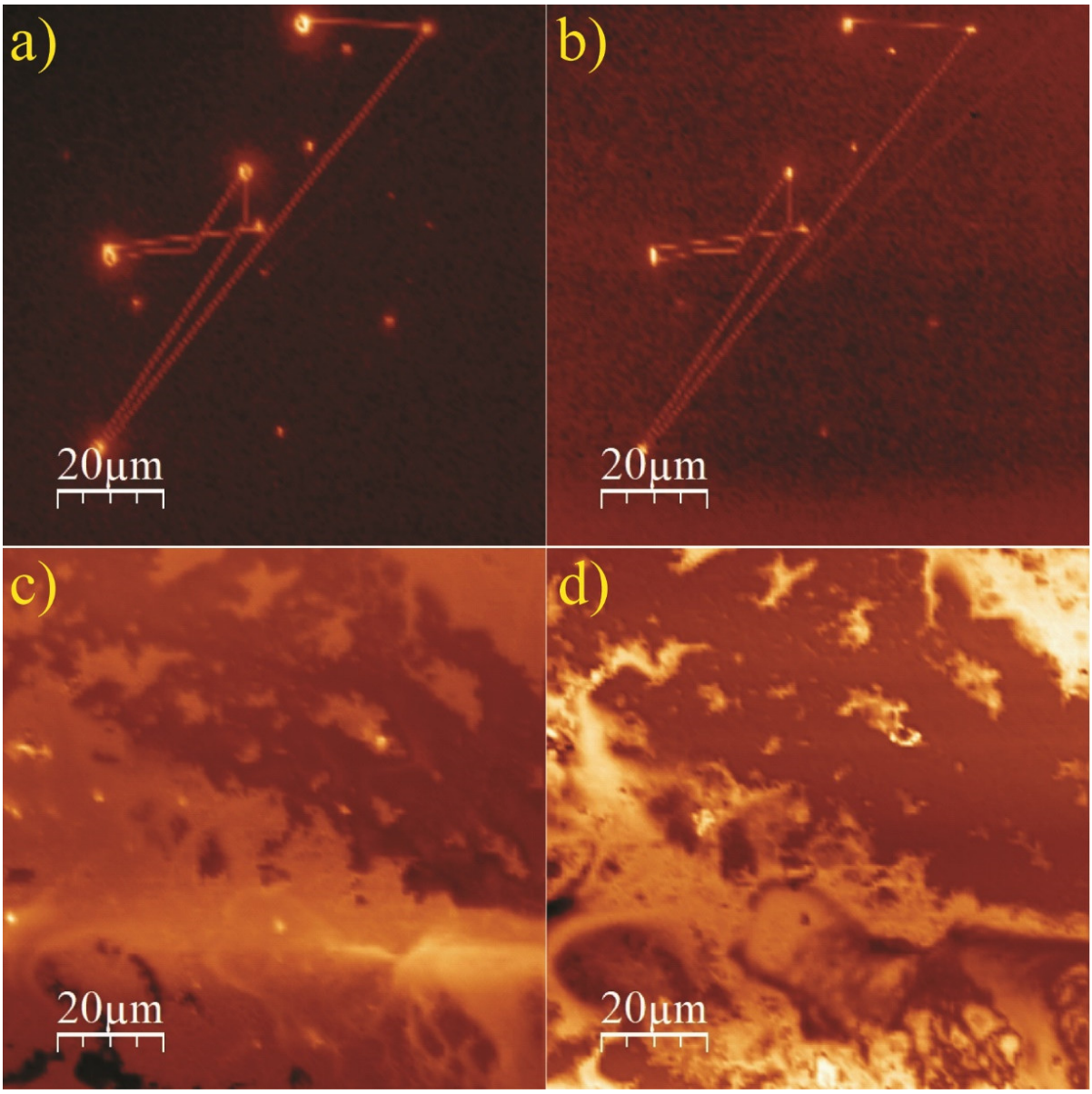

Figure B-S1 a&c) Luminescence and **b&d)** scattering images of pure linker (upper panel) & CdSe/I-/AE **1.** Pure linker films show laser tracing after continuous exposure to 488 nm laser indicating some changes in the film.

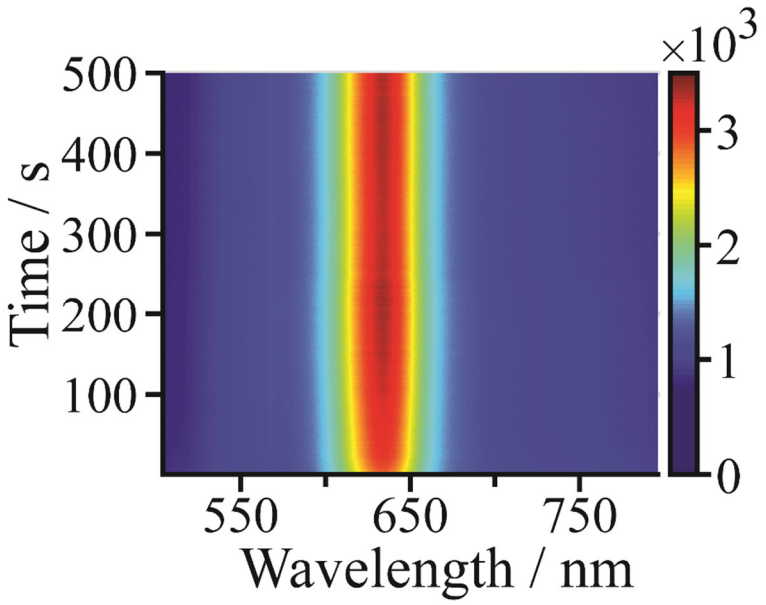

Figure B-S2 Thin film fluorescence of CdSe/I- NCs during 500 s of continuous excitation at 488 nm.

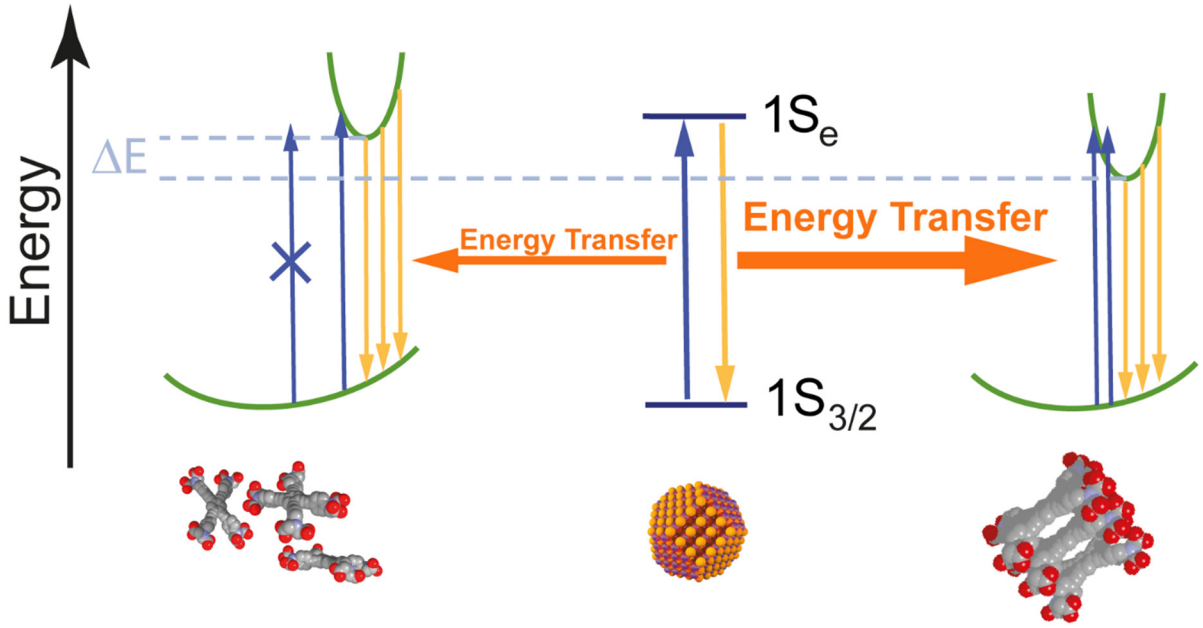

Scheme S2 Simplified energy level diagram of CdSe/I⁻/AE **1** NC thin films in the ordered state (**right**) as well as in the disordered state (**left**). **Blue arrows** indicate absorption, **yellow arrows** indicate emission pathways. Upon resonant excitation of the $1S_{3/2}$ - $1S_e$ transition of the NCs, the electron in the NC can either relax to the ground-state by radiative recombination or by transfer of its energy to AE **1** (**orange arrows**). For energy transfer, the emission energy in the NCs needs to match the absorption energy in AE **1**. This absorption energy exhibits a broad distribution due to the large number of rotamers with different energies (**green parabolas**), especially in the excited state, which are locked-in in the solid state. For ordered stacks of AE

1 molecules (**right**), there are several transitions between rotamers, which can be excited via energy transfer from the NCs. Thus, energy transfer is relatively efficient, resulting in bright fluorescence of AE **1**. In the disordered state (**left**), the average transition energy between rotamers is larger by ΔE compared to the ordered state. This is a consequence of the smaller degree of planarization of the molecules. In effect, the transferred energy from the NCs is not sufficient to excite most of the transitions between different rotamers in the disordered state, which leads to poor energy transfer and weak emission.

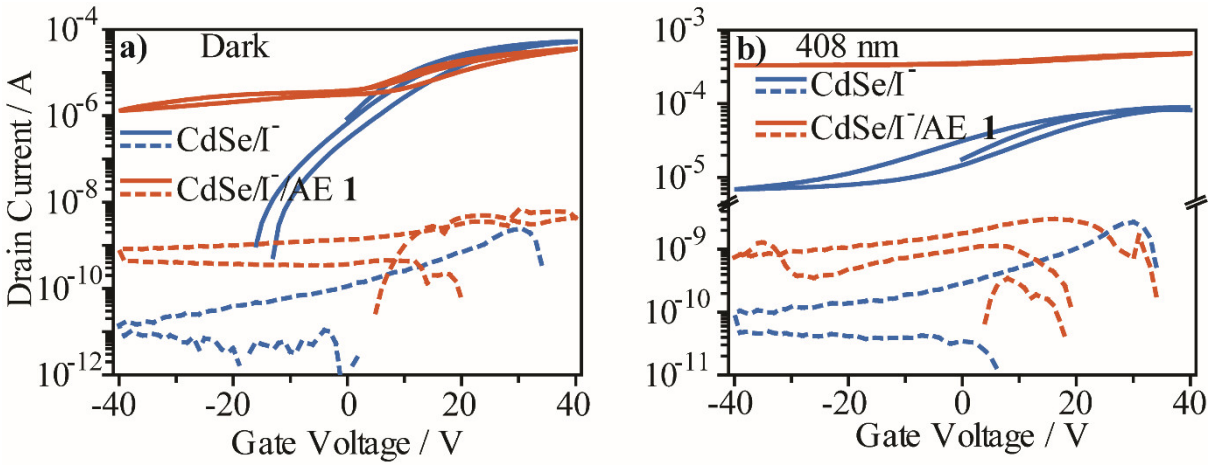

Figure B-S3 Typical gate-sweep curve at 5 V source-drain voltage measured at 200 K with channel dimension 2.5 µm × 1 cm **a)** under no illumination **b)** under 408 nm laser illumination. Solid curve represents the drain current and dotted curve represent the respective leakage current; negative data have been ignored for the logarithmic plot.

Symbols and Abbreviations

COIN	Coupled Organic-Inorganic Nanocrystals
NCs	Nanocrystals
OSCs	Organic Semiconductors
Zn4APc	zinc β-tetraaminophthalocyanine
AE **1**	Aryleneethynylene derivative
AIE	Aggregation Induced Emission
SAXS	Small Angle X-ray Scattering
GISAXS	Grazing Incidence Small Angle X-ray Scattering
a_B	Exciton Bohr radius
FETs	Field-Effect Transistor
CNT	Classical Nucleation Theory
ΔG	Gibbs free energy difference
R/r	Radius of nanocrystal
γ	Surface energy density
C_s	Saturation concentration
C_{min}	Minimum critical concentration
eV	Electron Volt
(IP)-EMA/EMA	Infinite Potential/Effective Mass Approimation
TB	Tight Binding

MOs	Molecular Orbitals
h	Planck's constant
E_g	Bulk band gap
ϵ	Permitivity of a medium
QDs	Quantum Dots
OA/Olm	Oleic Acid/Oleyl amine
TOP/TOPO	Trioctyl Phosphine/Oxide
HOMO/LUMO	Highest Occupied/Lowest Unoccupied -Molecular Orbital
β	Transfer integral
E_c	Chanrging energy
$\Delta\alpha$	Energetic disorder
Γ	Tunneling rate constant
C_{self}/ C_m	Self/mutual capacitance
BJT	Bipolar Junction Transistor
JFET	Junction Field Effect Transistor
MOSFET	Metal Oxide Semiconductor Field Effect Transistor
W	Applied reverse bias
W_0	Pinch-off potential
CB/VB	Conduction/Valence Band
E_f	Fermi level energy

N_c/N_v	Density of charge carriers in Conduction/Valence Band
i_{ph}	Photocurrent
G_i	Internal photoconductive gain
T_t	Transit time
τ	Lifetime of charge carrier
R_i	Sensitivity
k_B	Boltzmann constant
SEM/TEM	Scanning/Transmission Electron Microsccopy
XRD	X-ray Diffraction
$\vec{Q}$	Scattering vector
$\vec{k}$	Wave vector
$\Delta\phi$	Phase difference
ϵ	Exciton cofficient
NMR	Nuclear Magnetic Resonance
SSPL	Steady-State Photo Luminescence
TRPL	Time Resolved Photo Luminescence
TAS	Transient Absorption Spectroscopy

Table of Figures

List of Publications

Krishan Kumar, Jonas Hiller, Markus Bender, Saeed Nosrati, Quan Liu, Frank Wackenhut, Alfred J. Meixner, Kai Braun, Uwe H. F. Bunz, Marcus Scheele,"Periodic Fluorescence Variations of CdSe Quantum Dots Coupled to Aryleneethynylenes with Aggregation Induced Emission", submitted, **2020**

Krishan Kumar, Quan Liu, Jonas Hiller, Christine Schedel, Andre Maier, Alfred J Meixner, Kai Braun, Jannika Lauth, and Marcus Scheele, "Fast, Infrared-Active Optical Transistors Based on Dye-Sensitized CdSe Nanocrystals", *ACS Appl. Mater. Interfaces* **2019**, 11, 48271–48280.

Acknowledgements

Upon completion of this work, I would like to take this opportunity to express my sincere gratitude to the people involved.

First and foremost, I am wholeheartedly thankful to my supervisor Prof. Dr. Marcus Scheele. His scientific knowledge, constant support, optimism, and outstanding cooperation have helped me to advance my scientific career. His honest and critical review of my research work has enabled me to advance my scientific skills. His remarkable helpfulness in my social wellbeing is highly appreciable. I am very grateful for getting an opportunity to work in his research group.

I am thankful to my collaborators Prof. Dr. Alfred J. Meixner, Prof. Dr. Frank Schreiber, Dr. Jannika Lauth, and Prof. Dr. Uwe H. F. Bunz without these beneficial cooperation; this work wouldn't have been possible in its current form.

I am wholeheartedly thankful to my officemates Dr. Alexander André, Dr. Mahdi S. Khoshkhoo, Christine Schedel, Andre Maier for providing a great office environment and being always ready for scientific and non-scientific discussion. I extend my special thanks to the members of the group specially Björn Märker, Sonam Maiti, Michelle Weber, Kai Wurst, Jan Wahl, Christopher Kirsch, Sophia Westendorf, Philipp Frech, and the new colleague Philipp Haizmann for helping me with their different experience to carry out experiments and providing a fun and adaptive environment during various hangouts. I have enjoyed my time working with them.

I would further like to extend my sincere thanks to my colleagues from AK Meixner group, notably, Dr. Kai Braun, Dr. Frank Wackenhut and Dr. Imran Ashraf for their excellent and timely guidance on various experiments and social aspect of life. I would also like to thank Achim Junginger, Saeed Nosrati, Quan Liu, Otto Hauler, Jonas Hiller, and Tim Rammler for taking out their valuable time to help and carry out numerous experiments.

I appreciate Dr. Wolfgang Langer, Mrs. Brigitte Doez, Mrs. Diana Strauss and Mrs. Heike Alexa for their assistance with the administrative work. I am thankful to Mr. Karsten Stampke and Mr. Jochen Mehne for helping me in the issues related to electronics and student practical respectively. I further extend my thanks to Mrs. Elke Nadler, Andre Maier and NMR facility staff for taking out their long time to measure my SEM and NMR samples.

I am thankful to Andre Maier, Dr. Praveen Kumar, Dr. Ravi Yadav for proofreading my thesis. I am also thankful to Christine Schedel for translating summary of thesis to German.

I am grateful to the intern and master students of the group specially Konstantin, Theresa, Patrick for performing experiments. I would like to thank all my colleagues from AK Scheele and AK Meixner for providing a pleasant working environment.

I express my gratefulness to all my friends, in and out of Tübingen to make my time in Germany enjoyable and memorable.

Finally, my deepest gratitude to my parents, my partner Shivani Yadav and other members of the family for their continuous and unparalleled love, help and support. I am thankful for their sacrifices to promote my education.

References

(1) Quantum dot display https://en.wikipedia.org/wiki/Quantum_dot_display (accessed Jul 1, 2020).

(2) Werner, K. Five Short Display Stories from CES 2018. *Inf. Disp. (1975).* **2018**, *34*, 28–34.

(3) Rieger, M. L. Retrospective on VLSI Value Scaling and Lithography. *J. Micro/Nanolithography, MEMS, MOEMS* **2019**, *18*, 040902.

(4) Hey, A. *Feynman and Computation*; CRC Press: Boca Raton, Fla, 2018.

(5) Drexler, K. E. *Engines of Creation*; Science, technical; Anchor Press/Doubleday, 1986.

(6) Rossetti, R.; Nakahara, S.; Brus, L. E. Quantum Size Effects in the Redox Potentials, Resonance Raman Spectra, and Electronic Spectra of CdS Crystallites in Aqueous Solution. *J. Chem. Phys.* **1983**, *79*, 1086–1088.

(7) Brus, L. E. A Simple Model for the Ionization Potential, Electron Affinity, and Aqueous Redox Potentials of Small Semiconductor Crystallites. *J. Chem. Phys.* **1983**, *79*, 5566–5571.

(8) Murray, C. B.; Norris, D. J.; Bawendi, M. G. Synthesis and Characterization of Nearly Monodisperse CdE (E = Sulfur, Selenium, Tellurium) Semiconductor Nanocrystallites. *J. Am. Chem. Soc.* **1993**, *115*, 8706–8715.

(9) Cao, Y. C.; Wang, J. One-Pot Synthesis of High-Quality Zinc-Blende CdS Nanocrystals. *J. Am. Chem. Soc.* **2004**, *126*, 14336–14337.

(10) Bullen, C. R.; Mulvaney, P. Nucleation and Growth Kinetics of CdSe Nanocrystals in Octadecene. *Nano Lett.* **2004**, *4*, 2303–2307.

(11) Chen, Q.; Rondinone, A. J.; C. Chakoumakos, B.; John Zhang, Z. Synthesis of Superparamagnetic MgFe2O4 Nanoparticles by Coprecipitation. *J. Magn. Magn. Mater.* **1999**, *194*, 1–7.

(12) Mikhaylova, M.; Kim, D. K.; Bobrysheva, N. P.; Osmolowsky, M.; Semenov, V.; Tsakalakos, T.; Muhammed, M. Superparamagnetism of Magnetite Nanoparticles: Dependence on Surface Modification. *Langmuir* **2004**, *20*, 2472–2477.

(13) Amendola, V. Surface Plasmon Resonance of Silver and Gold Nanoparticles in the Proximity of Graphene Studied Using the Discrete Dipole Approximation Method. *Phys. Chem. Chem. Phys.* **2016**, *18*, 2230–2241.

(14) Jeon, H. Bin; Tsalu, P. V.; Ha, J. W. Shape Effect on the Refractive Index Sensitivity at Localized Surface Plasmon Resonance Inflection Points of Single Gold Nanocubes with Vertices. *Sci. Rep.* **2019**, *9*, 1–8.

(15) Zecchina, A.; Groppo, E.; Bordiga, S. Selective Catalysis and Nanoscience: An Inseparable Pair. *Chem. - A Eur. J.* **2007**, *13*, 2440–2460.

(16) Valden, M.; Lai, X.; Goodman, D. W. Onset of Catalytic Activity of Gold Clusters on Titania with the Appearance of Nonmetallic Properties. *Science* **1998**, *281*, 1647–1650.

(17) Baker, D. R.; Kamat, P. V. Tuning the Emission of CdSe Quantum Dots by Controlled Trap Enhancement. *Langmuir* **2010**, *26*, 11272–11276.

(18) Kovalenko, M. V.; Scheele, M.; Talapin, D. V. Colloidal Nanocrystals with Molecular Metal Chalcogenide Surface Ligands. *Science* **2009**, *324*, 1417–1420.

(19) Dirin, D. N.; Dreyfuss, S.; Bodnarchuk, M. I.; Nedelcu, G.; Papagiorgis, P.; Itskos, G.; Kovalenko, M. V. Lead Halide Perovskites and Other Metal Halide Complexes As Inorganic Capping Ligands for Colloidal Nanocrystals. *J. Am. Chem. Soc.* **2014**, *136*, 6550–6553.

(20) Nag, A.; Kovalenko, M. V.; Lee, J. S.; Liu, W.; Spokoyny, B.; Talapin, D. V. Metal-Free Inorganic Ligands for Colloidal Nanocrystals: S2-, HS-, Se2-, HSe-, Te2-, HTe-, TeS32-, OH-, and NH2-as Surface Ligands. *J. Am. Chem. Soc.* **2011**, *133*, 10612–10620.

(21) Huang, J.; Liu, W.; Dolzhnikov, D. S.; Protesescu, L.; Kovalenko, M. V.; Koo, B.; Chattopadhyay, S.; Shenchenko, E. V.; Talapin, D. V. Surface Functionalization of Semiconductor and Oxide Nanocrystals with Small Inorganic Oxoanions (PO43-, MoO42-) and Polyoxometalate Ligands. *ACS Nano* **2014**, *8*, 9388–9402.

(22) Lee, J.; Kovalenko, M. V; Huang, J.; Chung, D. S.; Talapin, D. V. Band-like Transport, High Electron Mobility and High Photoconductivity in All-Inorganic Nanocrystal Arrays. *Nat. Nanotechnol.* **2011**, *6*, 348–352.

(23) Oh, S. J.; Wang, Z.; Berry, N. E.; Choi, J. H.; Zhao, T.; Gaulding, E. A.; Paik, T.; Lai, Y.; Murray, C. B.; Kagan, C. R. Engineering Charge Injection and Charge Transport for

High Performance PbSe Nanocrystal Thin Film Devices and Circuits. *Nano Lett.* **2014**, *14*, 6210–6216.

(24) Samadi Khoshkhoo, M.; Joseph, Y.; Maiti, S.; Schreiber, F.; Chassé, T.; Scheele, M. Tunable Charge Transport in Hybrid Superlattices of Indium Tin Oxide Nanocrystals and Metal Phthalocyanines-Toward Sensing Applications. *Adv. Mater. Interfaces* **2018**, *5*, 1701623.

(25) Liu, Y.; Gibbs, M.; Puthussery, J.; Gaik, S.; Ihly, R.; Hillhouse, H. W.; Law, M. Dependence of Carrier Mobility on Nanocrystal Size and Ligand Length in PbSe Nanocrystal Solids. *Nano Lett.* **2010**, *10*, 1960–1969.

(26) Scheele, M.; Hanifi, D.; Zherebetskyy, D.; Chourou, S. T.; Axnanda, S.; Rancatore, B. J.; Thorkelsson, K.; Xu, T.; Liu, Z.; Wang, L. W.; Liu, Y.; Alivisatos, A. P. PbS Nanoparticles Capped with Tetrathiafulvalenetetracarboxylate: Utilizing Energy Level Alignment for Efficient Carrier Transport. *ACS Nano* **2014**, *8*, 2532–2540.

(27) Wurst, K. M.; Bender, M.; Lauth, J.; Maiti, S.; Chassé, T.; Meixner, A.; Siebbeles, L. D. A.; Bunz, U. H. F.; Braun, K.; Scheele, M. Correlated, Dual-Beam Optical Gating in Coupled Organic-Inorganic Nanostructures. *Angew. Chemie Int. Ed.* **2018**, *57*, 11559–11563.

(28) Vitukhnovsky, A. G.; Lebedev, V. S.; Selyukov, A. S.; Vashchenko, A. A.; Vasiliev, R. B.; Sokolikova, M. S. Electroluminescence from Colloidal Semiconductor CdSe Nanoplatelets in Hybrid Organic–Inorganic Light Emitting Diode. *Chem. Phys. Lett.* **2015**, *619*, 185–188.

(29) Ongul, F.; Yuksel, S. A.; Allahverdi, C.; Bozar, S.; Kazici, M.; Gunes, S. Influences of CdSe NCs on the Photovoltaic Parameters of BHJ Organic Solar Cells. *Spectrochim. Acta Part A Mol. Biomol. Spectrosc.* **2018**, *194*, 50–56.

(30) Guo, X.; Tan, Q.; Liu, S.; Qin, D.; Mo, Y.; Hou, L.; Liu, A.; Wu, H.; Ma, Y. High-Efficiency Solution-Processed CdTe Nanocrystal Solar Cells Incorporating a Novel Crosslinkable Conjugated Polymer as the Hole Transport Layer. *Nano Energy* **2018**, *46*, 150–157.

(31) Dabbousi, B. O.; Bawendi, M. G.; Onitsuka, O.; Rubner, M. F. Electroluminescence from CdSe Quantum-dot/Polymer Composites. *Appl. Phys. Lett.* **1995**, *66*, 1316–1318.

(32) Colvin, V. L.; Schlamp, M. C.; Alivisatos, A. P. Light-Emitting Diodes Made from Cadmium Selenide Nanocrystals and a Semiconducting Polymer. *Nature* **1994**, *370*, 354–357.

(33) Dong, R.; Bi, C.; Dong, Q.; Guo, F.; Yuan, Y.; Fang, Y.; Xiao, Z.; Huang, J. An Ultraviolet-to-NIR Broad Spectral Nanocomposite Photodetector with Gain. *Adv. Opt. Mater.* **2014**, *2*, 549–554.

(34) Konstantatos, G.; Clifford, J.; Levina, L.; Sargent, E. H. Sensitive Solution-Processed Visible-Wavelength Photodetectors. *Nat. Photonics* **2007**, *1*, 531–534.

(35) Becker, R.; Döring, W. Kinetische Behandlung Der Keimbildung in Übersättigten Dämpfen. *Ann. Phys.* **1935**, *416*, 719–752.

(36) Mer, V. K. La. Nucleation in Phase Transitions. *Ind. Eng. Chem.* **1952**, *44*, 1270–1277.

(37) Polte, J. Fundamental Growth Principles of Colloidal Metal Nanoparticles – a New Perspective. *CrystEngComm* **2015**, *17*, 6809–6830.

(38) LaMer, V. K.; Dinegar, R. H. Theory, Production and Mechanism of Formation of Monodispersed Hydrosols. *J. Am. Chem. Soc.* **1950**, *72*, 4847–4854.

(39) Peng, X.; Wickham, J.; Alivisatos, A. P. Kinetics of II-VI and III-V Colloidal Semiconductor Nanocrystal Growth: "Focusing" of Size Distributions. *J. Am. Chem. Soc.* **1998**, *120*, 5343–5344.

(40) Tian, H. Z.; Xiang, Y. L. How Does a Transient Amorphous Precursor Template Crystallization. *J. Am. Chem. Soc.* **2007**, *129*, 13520–13526.

(41) Zhang, T. H.; Liu, X. Y. Nucleation: What Happens at the Initial Stage? *Angew. Chemie - Int. Ed.* **2009**, *48*, 1308–1312.

(42) Savage, J. R.; Dinsmore, A. D. Experimental Evidence for Two-Step Nucleation in Colloidal Crystallization. *Phys. Rev. Lett.* **2009**, *102*, 15–18.

(43) Peng, Z. A.; Peng, X. Nearly Monodisperse and Shape-Controlled CdSe Nanocrystals via Alternative Routes: Nucleation and Growth. *J. Am. Chem. Soc.* **2002**, *124*, 3343–3353.

(44) Xia, Y.; Xia, X.; Peng, H. C. Shape-Controlled Synthesis of Colloidal Metal Nanocrystals: Thermodynamic versus Kinetic Products. *J. Am. Chem. Soc.* **2015**, *137*,

7947–7966.

(45) Peng, X. Mechanisms for the Shape-Control and Shape-Evolution of Colloidal Semiconductor Nanocrystals. *Adv. Mater.* **2003**, *15*, 459–463.

(46) Manna, L.; Milliron, D. J.; Meisel, A.; Scher, E. C.; Alivisatos, A. P. Controlled Growth of Tetrapod-Branched Inorganic Nanocrystals. *Nat. Mater.* **2003**, *2*, 382–385.

(47) Lu, H. M.; Jiang, Q. Size-Dependent Surface Energies of Nanocrystals. *J. Phys. Chem. B* **2004**, *108*, 5617–5619.

(48) Rempel, J. Y.; Trout, B. L.; Bawendi, M. G.; Jensen, K. F. Density Functional Theory Study of Ligand Binding on CdSe (0001), (000$\bar{1}$), and (11$\bar{2}$0) Single Crystal Relaxed and Reconstructed Surfaces: Implications for Nanocrystalline Growth. *J. Phys. Chem. B* **2006**, *110*, 18007–18016.

(49) Bealing, C. R.; Baumgardner, W. J.; Choi, J. J.; Hanrath, T.; Hennig, R. G. Predicting Nanocrystal Shape through Consideration of Surface-Ligand Interactions. *ACS Nano* **2012**, *6*, 2118–2127.

(50) Nag, A.; Hazarika, A.; Shanavas, K. V.; Sharma, S. M.; Dasgupta, I.; Sarma, D. D. Crystal Structure Engineering by Fine-Tuning the Surface Energy: The Case of CdE (E = S/Se) Nanocrystals. *J. Phys. Chem. Lett.* **2011**, *2*, 706–712.

(51) Thanh, N. T. K.; Maclean, N.; Mahiddine, S. Mechanisms of Nucleation and Growth of Nanoparticles in Solution. *Chem. Rev.* **2014**, *114*, 7610–7630.

(52) Rao, C. N. R.; Müller, A.; Cheetham, A. K. *The Chemistry of Nanomaterials: Synthesis, Properties and Applications*; John Wiley & Sons, 2004.

(53) Efros, A. L.; Efros, A. L. Interband Light Absorption in Semiconductor Spheres. *Sov. Phys. Semicond. USSR* **1982**, *16*, 772–775.

(54) Brus, L. Electronic Wave Functions in Semiconductor Clusters: Experiment and Theory. *J. Phys. Chem.* **1986**, *90*, 2555–2560.

(55) Brus, L. E. Electron–Electron and Electron-hole Interactions in Small Semiconductor Crystallites: The Size Dependence of the Lowest Excited Electronic State. *J. Chem. Phys.* **1984**, *80*, 4403–4409.

(56) Kayanuma, Y. Quantum-Size Effects of Interacting Electrons and Holes in

Semiconductor Microcrystals with Spherical Shape. *Phys. Rev. B* **1988**, *38*, 9797–9805.

(57) Kayanuma, Y. Wannier Exciton in Microcrystals. *Solid State Commun.* **1986**, *59*, 405–408.

(58) Sapra, S.; Sarma, D. D. Evolution of the Electronic Structure with Size in II-VI Semiconductor Nanocrystals. *Phys. Rev. B - Condens. Matter Mater. Phys.* **2004**, *69*, 1–7.

(59) Kayanuma, Y.; Momiji, H. Incomplete Confinement of Electrons and Holes in Microcrystals. *Phys. Rev. B* **1990**, *41*, 10261–10263.

(60) Norris, D. J.; Sacra, A.; Murray, C. B.; Bawendi, M. G. Measurement of the Size Dependent Hole Spectrum in CdSe Quantum Dots. *Phys. Rev. Lett.* **1994**, *72*, 2612–2615.

(61) Norris, D. J.; Bawendi, M. G. Measurement and Assignment of the Size-Dependent Optical Spectrum in CdSe Quantum Dots. *Phys. Rev. B* **1996**, *53*, 16338–16346.

(62) Sayevich, V.; Guhrenz, C.; Dzhagan, V. M.; Sin, M.; Werheid, M.; Cai, B.; Borchardt, L.; Widmer, J.; Zahn, D. R. T.; Brunner, E.; Lesnyak, V.; Gaponik, N.; Eychmüller, A. Hybrid N-Butylamine-Based Ligands for Switching the Colloidal Solubility and Regimentation of Inorganic-Capped Nanocrystals. *ACS Nano* **2017**, *11*, 1559–1571.

(63) Zhang, H.; Jang, J.; Liu, W.; Talapin, D. V. Colloidal Nanocrystals with Inorganic Halide, Pseudohalide, and Halometallate Ligands. *ACS Nano* **2014**, *8*, 7359–7369.

(64) Lee, D. C.; Robel, I.; Pietryga, J. M.; Klimov, V. I. Infrared-Active Heterostructured Nanocrystals with Ultralong Carrier Lifetimes. *J. Am. Chem. Soc.* **2010**, *132*, 9960–9962.

(65) Scheele, M.; Brütting, W.; Schreiber, F. Coupled Organic–Inorganic Nanostructures (COIN). *Phys. Chem. Chem. Phys.* **2015**, *17*, 97–111.

(66) Ghosh Chaudhuri, R.; Paria, S. Core/Shell Nanoparticles: Classes, Properties, Synthesis Mechanisms, Characterization, and Applications. *Chem. Rev.* **2012**, *112*, 2373–2433.

(67) Kudera, S.; Maus, L.; Zanella, M.; Pelaz, B.; Zhang, Q.; Parak, W. J.; del Pino, P.; Parak, W. J. Inorganic Core–Shell Nanoparticles. In *Comprehensive Nanoscience and Nanotechnology*; Elsevier, 2016; Vol. 1–5, pp 171–186.

(68) Majetich, S.; Carter, A.; McCullough, R. D.; Seth, J.; Belot, J. A. Connected CdSe Nanocrystallite Networks. *Zeitschrift für Phys. D Atoms, Mol. Clust.* **1993**, *26*, 210–212.

(69) Talapin, D. V.; Lee, J.-S.; Kovalenko, M. V.; Shevchenko, E. V. Prospects of Colloidal Nanocrystals for Electronic and Optoelectronic Applications. *Chem. Rev.* **2010**, *110*, 389–458.

(70) Kumar, K.; Liu, Q.; Hiller, J.; Schedel, C.; Maier, A.; Meixner, A.; Braun, K.; Lauth, J.; Scheele, M. Fast, Infrared-Active Optical Transistors Based on Dye-Sensitized CdSe Nanocrystals. *ACS Appl. Mater. Interfaces* **2019**, *11*, 48271–48280.

(71) Szendrei, K.; Jarzab, D.; Yarema, M.; Sytnyk, M.; Pichler, S.; Hummelen, J. C.; Heiss, W.; Loi, M. A. Surface Modification of Semiconductor Nanocrystals by a Methanofullerene Carboxylic Acid. *J. Mater. Chem.* **2010**, *20*, 8470–8473.

(72) André, A.; Zherebetskyy, D.; Hanifi, D.; He, B.; Samadi Khoshkhoo, M.; Jankowski, M.; Chassé, T.; Wang, L.-W.; Schreiber, F.; Salleo, A.; Liu, Y.; Scheele, M. Toward Conductive Mesocrystalline Assemblies: PbS Nanocrystals Cross-Linked with Tetrathiafulvalene Dicarboxylate. *Chem. Mater.* **2015**, *27*, 8105–8115.

(73) André, A.; Theurer, C.; Lauth, J.; Maiti, S.; Hodas, M.; Samadi Khoshkhoo, M.; Kinge, S.; Meixner, A. J.; Schreiber, F.; Siebbeles, L. D. A.; Braun, K.; Scheele, M. Structure, Transport and Photoconductance of PbS Quantum Dot Monolayers Functionalized with a Copper Phthalocyanine Derivative. *Chem. Commun.* **2017**, *53*, 1700–1703.

(74) Maiti, S.; Maiti, S.; Maier, A.; Hagenlocher, J.; Chumakov, A.; Schreiber, F.; Scheele, M. Understanding the Formation of Conductive Mesocrystalline Superlattices with Cubic PbS Nanocrystals at the Liquid/Air Interface. *J. Phys. Chem. C* **2019**, *123*, 1519–1526.

(75) Samadi Khoshkhoo, M.; Maiti, S.; Schreiber, F.; Chassé, T.; Scheele, M. Surface Functionalization with Copper Tetraaminophthalocyanine Enables Efficient Charge Transport in Indium Tin Oxide Nanocrystal Thin Films. *ACS Appl. Mater. Interfaces* **2017**, *9*, 14197–14206.

(76) Maiti, S.; Maiti, S.; Joseph, Y.; Wolf, A.; Brütting, W.; Dorfs, D.; Schreiber, F.; Scheele, M. Electronically Coupled, Two-Dimensional Assembly of Cu1.1S Nanodiscs for Selective Vapor Sensing Applications. *J. Phys. Chem. C* **2018**, *122*, 23720–23727.

(77) Maiti, S.; Maiti, S.; Khan, A. H.; Wolf, A.; Dorfs, D.; Moreels, I.; Schreiber, F.; Scheele, M. Dye-Sensitized Ternary Copper Chalcogenide Nanocrystals: Optoelectronic Properties, Air Stability, and Photosensitivity. *Chem. Mater.* **2019**, *31*, 2443–2449.

(78) Maiti, S.; Maiti, S.; Maier, A.; Banerjee, R.; Shen, C.; Murphy, B. M.; Scheele, M.; Schreiber, F. In Situ Formation of Electronically Coupled Superlattices of Cu1.1S Nanodiscs at the Liquid/Air Interface. *Chem. Commun.* **2019**, *55*, 4805–4808.

(79) Quinn, A. J.; Beecher, P.; Iacopino, D.; Floyd, L.; De Marzi, G.; Shevchenko, E. V.; Weller, H.; Redmond, G. Manipulating the Charging Energy of Nanocrystal Arrays. *Small* **2005**, *1*, 613–618.

(80) Penn, D. R. Wave-Number-Dependent Dielectric Function of Semiconductors. *Phys. Rev.* **1962**, *128*, 2093–2097.

(81) Sharma, A. C. Size-Dependent Energy Band Gap and Dielectric Constant within the Generalized Penn Model Applied to a Semiconductor Nanocrystallite. *J. Appl. Phys.* **2006**, *100*, 084301.

(82) Zabet-Khosousi, A.; Trudeau, P.-E.; Suganuma, Y.; Dhirani, A.-A.; Statt, B. Metal to Insulator Transition in Films of Molecularly Linked Gold Nanoparticles. *Phys. Rev. Lett.* **2006**, *96*, 156403.

(83) Collier, C. P.; Saykally, R. J.; Shiang, J. J.; Henrichs, S. E.; Heath, J. R. Reversible Tuning of Silver Quantum Dot Monolayers through the Metal- Insulator Transition. *Science* **1997**, *277*, 1978–1981.

(84) Murray, C. B.; Kagan, C. R.; Bawendi, M. G. Synthesis and Characterization of Monodisperse Nanocrystals and Close-Packed Nanocrystal Assemblies. *Annu. Rev. Mater. Sci.* **2000**, *30*, 545–610.

(85) Shockley, W. A Unipolar “Field-Effect” Transistor. *Proc. IRE* **1952**, *40*, 1365–1376.

(86) Horowitz, G. Organic Field-Effect Transistors. *Adv. Mater.* **1998**, *10*, 365–377.

(87) Weis, M. Gradual Channel Approximation Models for Organic Field-Effect Transistors: The Space-Charge Field Effect. *J. Appl. Phys.* **2012**, *111*, 054506.

(88) Nagpal, P.; Klimov, V. I. Role of Mid-Gap States in Charge Transport and Photoconductivity in Semiconductor Nanocrystal Films. *Nat. Commun.* **2011**, *2*, 486.

(89) Talgorn, E.; Gao, Y.; Aerts, M.; Kunneman, L. T.; Schins, J. M.; Savenije, T. J.; van Huis, M. A.; van der Zant, H. S. J.; Houtepen, A. J.; Siebbeles, L. D. A. Unity Quantum Yield of Photogenerated Charges and Band-like Transport in Quantum-Dot Solids. *Nat. Nanotechnol.* **2011**, *6*, 733–739.

(90) Rose, A. *Concepts in Photoconductivity and Allied Problems*; Interscience tracts on physics and astronomy; Interscience Publishers, 1963.

(91) Rose, A. Recombination Processes in Insulators and Semiconductors. *Phys. Rev.* **1955**, *97*, 322–333.

(92) Saran, R.; Curry, R. J. Lead Sulphide Nanocrystal Photodetector Technologies. *Nat. Photonics* **2016**, *10*, 81–92.

(93) Gao, Y.; Aerts, M.; Sandeep, C. S. S.; Talgorn, E.; Savenije, T. J.; Kinge, S.; Siebbeles, L. D. A.; Houtepen, A. J. Photoconductivity of PbSe Quantum-Dot Solids: Dependence on Ligand Anchor Group and Length. *ACS Nano* **2012**, *6*, 9606–9614.

(94) Shabaev, A.; Efros, A. L.; Efros, A. L. Dark and Photo-Conductivity in Ordered Array of Nanocrystals. *Nano Lett.* **2013**, *13*, 5454–5461.

(95) Boles, M. A.; Engel, M.; Talapin, D. V. Self-Assembly of Colloidal Nanocrystals: From Intricate Structures to Functional Materials. *Chem. Rev.* **2016**, *116*, 11220–11289.

(96) Pérez-Juste, J.; Rodríguez-González, B.; Mulvaney, P.; Liz-Marzán, L. M. Optical Control and Patterning of Gold-Nanorod-Poly(Vinyl Alcohol) Nanocomposite Films. *Adv. Funct. Mater.* **2005**, *15*, 1065–1071.

(97) Frederick, M. T.; Achtyl, J. L.; Knowles, K. E.; Weiss, E. A.; Geiger, F. M. Surface-Amplified Ligand Disorder in CdSe Quantum Dots Determined by Electron and Coherent Vibrational Spectroscopies. *J. Am. Chem. Soc.* **2011**, *133*, 7476–7481.

(98) Luedtke, W. D.; Landman, U. Structure, Dynamics, and Thermodynamics of Passivated Gold Nanocrystallites and Their Assemblies. *J. Phys. Chem.* **1996**, *100*, 13323–13329.

(99) Hong, Y.; Lam, J. W. Y.; Tang, B. Z. Aggregation-Induced Emission: Phenomenon, Mechanism and Applications. *Chem. Commun.* **2009**, No. 29, 4332.

(100) Henzie, J.; Grünwald, M.; Widmer-Cooper, A.; Geissler, P. L.; Yang, P. Self-Assembly of Uniform Polyhedral Silver Nanocrystals into Densest Packings and Exotic

Superlattices. *Nat. Mater.* **2012**, *11*, 131–137.

(101) Ye, X.; Chen, J.; Murray, C. B. Polymorphism in Self-Assembled AB 6 Binary Nanocrystal Superlattices. *J. Am. Chem. Soc.* **2011**, *133*, 2613–2620.

(102) Liu, Y.; Lin, X.-M.; Sun, Y.; Rajh, T. In Situ Visualization of Self-Assembly of Charged Gold Nanoparticles. *J. Am. Chem. Soc.* **2013**, *135*, 3764–3767.

(103) Sutter, E.; Sutter, P.; Tkachenko, A. V.; Krahne, R.; de Graaf, J.; Arciniegas, M.; Manna, L. In Situ Microscopy of the Self-Assembly of Branched Nanocrystals in Solution. *Nat. Commun.* **2016**, *7*, 11213.

(104) Sayevich, V.; Guhrenz, C.; Sin, M.; Dzhagan, V. M.; Weiz, A.; Kasemann, D.; Brunner, E.; Ruck, M.; Zahn, D. R. T.; Leo, K.; Gaponik, N.; Eychmüller, A. Chloride and Indium-Chloride-Complex Inorganic Ligands for Efficient Stabilization of Nanocrystals in Solution and Doping of Nanocrystal Solids. *Adv. Funct. Mater.* **2016**, *26*, 2163–2175.

(105) Chen, O.; Chen, X.; Yang, Y.; Lynch, J.; Wu, H.; Zhuang, J.; Cao, Y. C. Synthesis of Metal-Selenide Nanocrystals Using Selenium Dioxide as the Selenium Precursor. *Angew. Chemie Int. Ed.* **2008**, *47*, 8638–8641.

(106) Yu, W. W.; Qu, L.; Guo, W.; Peng, X. Experimental Determination of the Extinction Coefficient of CdTe, CdSe, and CdS Nanocrystals. *Chem. Mater.* **2003**, *15*, 2854–2860.

(107) Knauf, R. R.; Lennox, J. C.; Dempsey, J. L. Quantifying Ligand Exchange Reactions at CdSe Nanocrystal Surfaces. *Chem. Mater.* **2016**, *28*, 4762–4770.

(108) Anderson, N. C.; Hendricks, M. P.; Choi, J. J.; Owen, J. S. Ligand Exchange and the Stoichiometry of Metal Chalcogenide Nanocrystals: Spectroscopic Observation of Facile Metal-Carboxylate Displacement and Binding. *J. Am. Chem. Soc.* **2013**, *135*, 18536–18548.

(109) Wackenhut, F.; Virgilio Failla, A.; Züchner, T.; Steiner, M.; Meixner, A. J. Three-Dimensional Photoluminescence Mapping and Emission Anisotropy of Single Gold Nanorods. *Appl. Phys. Lett.* **2012**, *100*, 263102.

(110) Lauth, J.; Grimaldi, G.; Kinge, S.; Houtepen, A. J.; Siebbeles, L. D. A.; Scheele, M. Ultrafast Charge Transfer and Upconversion in Zinc β-Tetraaminophthalocyanine-Functionalized PbS Nanostructures Probed by Transient Absorption Spectroscopy. *Angew. Chemie - Int. Ed.* **2017**, *56*, 14061–14065.

(111) Lauth, J.; Kinge, S.; Siebbeles, L. D. A. Ultrafast Transient Absorption and Terahertz Spectroscopy as Tools to Probe Photoexcited States and Dynamics in Colloidal 2D Nanostructures. *Zeitschrift fur Phys. Chemie* **2017**, *231*, 107–119.

(112) Smit, M.; van der Tol, J.; Hill, M. Moore's Law in Photonics. *Laser Photon. Rev.* **2012**, *6*, 1–13.

(113) Thomson, D.; Zilkie, A.; Bowers, J. E.; Komljenovic, T.; Reed, G. T.; Vivien, L.; Marris-Morini, D.; Cassan, E.; Virot, L.; Fédéli, J.-M.; Hartmann, J.-M.; Schmid, J. H.; Xu, D.-X.; Boeuf, F.; O'Brien, P.; Mashanovich, G. Z.; Nedeljkovic, M. Roadmap on Silicon Photonics. *J. Opt.* **2016**, *18*, 073003.

(114) Franz, J.; Jain, V. K. Optical Communications : Components and Systems : Analysis, Design, Optimization, Application. CRC Press ; New Delhi : Narosa Pub. House: Boca Raton, Fla 2000.

(115) Feng, D.; Liao, S.; Liang, H.; Fong, J.; Bijlani, B.; Shafiiha, R.; Luff, B. J.; Luo, Y.; Cunningham, J.; Krishnamoorthy, A. V; Asghari, M. High Speed GeSi Electro-Absorption Modulator at 1550 Nm Wavelength on SOI Waveguide. *Opt. Express* **2012**, *20*, 22224.

(116) Liu, M.; Yin, X.; Ulin-Avila, E.; Geng, B.; Zentgraf, T.; Ju, L.; Wang, F.; Zhang, X. A Graphene-Based Broadband Optical Modulator. *Nature* **2011**, *474*, 64–67.

(117) Tang, Y.; Peters, J. D.; Bowers, J. E. Over 67 GHz Bandwidth Hybrid Silicon Electroabsorption Modulator with Asymmetric Segmented Electrode for 13 Mm Transmission. *Opt. Express* **2012**, *20*, 11529.

(118) Yu, Y.; Zhang, Y.; Zhang, Z.; Zhang, H.; Song, X.; Cao, M.; Che, Y.; Dai, H.; Yang, J.; Wang, J.; Zhang, H.; Yao, J. Broadband Phototransistor Based on CH 3 NH 3 PbI 3 Perovskite and PbSe Quantum Dot Heterojunction. *J. Phys. Chem. Lett.* **2017**, *8*, 445–451.

(119) Bao, J.; Bawendi, M. G. A Colloidal Quantum Dot Spectrometer. *Nature* **2015**, *523*, 67–70.

(120) Konstantatos, G.; Sargent, E. H. Nanostructured Materials for Photon Detection. *Nat. Nanotechnol.* **2010**, *5*, 391–400.

(121) Yu, Y.; Zhang, Y.; Song, X.; Zhang, H.; Cao, M.; Che, Y.; Dai, H.; Yang, J.; Zhang, H.;

Yao, J. PbS-Decorated WS 2 Phototransistors with Fast Response. *ACS Photonics* **2017**, *4*, 950–956.

(122) Aqua, T.; Naaman, R.; Aharoni, A.; Banin, U.; Paltiel, Y. Hybrid Nanocrystals-Organic-Semiconductor Light Sensor. *Appl. Phys. Lett.* **2008**, *92*, 223112.

(123) Neubauer, A.; Yochelis, S.; Amit, Y.; Banin, U.; Paltiel, Y. Highly Sensitive Room Temperature Infrared Hybrid Organic-Nanocrystal Detector. *Sensors Actuators A Phys.* **2015**, *229*, 166–171.

(124) Adinolfi, V.; Sargent, E. H. Photovoltage Field-Effect Transistors. *Nature* **2017**, *542*, 324–327.

(125) Kufer, D.; Nikitskiy, I.; Lasanta, T.; Navickaite, G.; Koppens, F. H. L.; Konstantatos, G. Hybrid 2D-0D MoS 2 -PbS Quantum Dot Photodetectors. *Adv. Mater.* **2015**, *27*, 176–180.

(126) Clifford, J. P.; Konstantatos, G.; Johnston, K. W.; Hoogland, S.; Levina, L.; Sargent, E. H. Fast, Sensitive and Spectrally Tuneable Colloidal-Quantum-Dot Photodetectors. *Nat. Nanotechnol.* **2009**, *4*, 40–44.

(127) Konstantatos, G.; Howard, I.; Fischer, A.; Hoogland, S.; Clifford, J.; Klem, E.; Levina, L.; Sargent, E. H. Ultrasensitive Solution-Cast Quantum Dot Photodetectors. *Nature* **2006**, *442*, 180–183.

(128) McDonald, S. A.; Konstantatos, G.; Zhang, S.; Cyr, P. W.; Klem, E. J. D.; Levina, L.; Sargent, E. H. Solution-Processed PbS Quantum Dot Infrared Photodetectors and Photovoltaics. *Nat. Mater.* **2005**, *4*, 138–142.

(129) Greenham, N. C.; Peng, X.; Alivisatos, A. P. Charge Separation and Transport in Conjugated-Polymer/Semiconductor-Nanocrystal Composites Studied by Photoluminescence Quenching and Photoconductivity. *Phys. Rev. B* **1996**, *54*, 17628–17637.

(130) Leatherdale, C. A.; Kagan, C. R.; Morgan, N. Y.; Empedocles, S. A.; Kastner, M. A.; Bawendi, M. G. Photoconductivity in CdSe Quantum Dot Solids. *Phys. Rev. B* **2000**, *62*, 2669–2680.

(131) Dolzhnikov, D. S.; Zhang, H.; Jang, J.; Son, J. S.; Panthani, M. G.; Shibata, T.; Chattopadhyay, S.; Talapin, D. V. Composition-Matched Molecular “Solders” for

Semiconductors. *Science* **2015**, *347*, 6–10.

(132) Kagan, C. R.; Lifshitz, E.; Sargent, E. H.; Talapin, D. V. Building Devices from Colloidal Quantum Dots. *Science* **2016**, *353*, aac5523–aac5523.

(133) Kagan, C. R. Flexible Colloidal Nanocrystal Electronics. *Chem. Soc. Rev.* **2019**, *48*, 1626–1641.

(134) Wang, Y.; Fedin, I.; Zhang, H.; Talapin, D. V. Direct Optical Lithography of Functional Inorganic Nanomaterials. *Science* **2017**, *357*, 385–388.

(135) Lee, J.-S.; Kovalenko, M. V; Huang, J.; Chung, D. S.; Talapin, D. V. Band-like Transport, High Electron Mobility and High Photoconductivity in All-Inorganic Nanocrystal Arrays. *Nat. Nanotechnol.* **2011**, *6*, 348–352.

(136) Marmon, J. K.; Rai, S. C.; Wang, K.; Zhou, W.; Zhang, Y. Light-Effect Transistor (LET) with Multiple Independent Gating Controls for Optical Logic Gates and Optical Amplification. *Front. Phys.* **2016**, *4*.

(137) Ra, H.-S.; Kwak, D.-H.; Lee, J.-S. A Hybrid MoS 2 Nanosheet–CdSe Nanocrystal Phototransistor with a Fast Photoresponse. *Nanoscale* **2016**, *8*, 17223–17230.

(138) Lee, A.-Y.; Ra, H.-S.; Kwak, D.-H.; Jeong, M.-H.; Park, J.-H.; Kang, Y.-S.; Chae, W.-S.; Lee, J.-S. Hybrid Black Phosphorus/Zero-Dimensional Quantum Dot Phototransistors: Tunable Photodoping and Enhanced Photoresponsivity. *ACS Appl. Mater. Interfaces* **2018**, *10*, 16033–16040.

(139) Qin, J.-K.; Ren, D.-D.; Shao, W.-Z.; Li, Y.; Miao, P.; Sun, Z.-Y.; Hu, P.; Zhen, L.; Xu, C.-Y. Photoresponse Enhancement in Monolayer ReS 2 Phototransistor Decorated with CdSe–CdS–ZnS Quantum Dots. *ACS Appl. Mater. Interfaces* **2017**, *9*, 39456–39463.

(140) Kim, S.; Noh, J.; Choi, H.; Ha, H.; Song, J. H.; Shim, H. C.; Jang, J.; Beard, M. C.; Jeong, S. One-Step Deposition of Photovoltaic Layers Using Iodide Terminated PbS Quantum Dots. *J. Phys. Chem. Lett.* **2014**, *5*, 4002–4007.

(141) Choi, J.-H.; Fafarman, A. T.; Oh, S. J.; Ko, D.-K.; Kim, D. K.; Diroll, B. T.; Muramoto, S.; Gillen, J. G.; Murray, C. B.; Kagan, C. R. Bandlike Transport in Strongly Coupled and Doped Quantum Dot Solids: A Route to High-Performance Thin-Film Electronics. *Nano Lett.* **2012**, *12*, 2631–2638.

(142) Lauth, J.; Grimaldi, G.; Kinge, S.; Houtepen, A. J.; Siebbeles, L. D. A.; Scheele, M. Ultrafast Charge Transfer and Upconversion in Zinc β-Tetraaminophthalocyanine-Functionalized PbS Nanostructures Probed by Transient Absorption Spectroscopy. *Angew. Chemie Int. Ed.* **2017**, *56*, 14061–14065.

(143) Kale, R. B.; Sartale, S. D.; Chougule, B. K.; Lokhande, C. D. Growth and Characterization of Nanocrystalline CdSe Thin Films Deposited by the Successive Ionic Layer Adsorption and Reaction Method. *Semicond. Sci. Technol.* **2004**, *19*, 980–986.

(144) Babu, N. S.; Khadar, M. A. Electrical Properties of Grain Size Tuned CdSe Nanocrystal Films for Practical Applications. *Sol. Energy Mater. Sol. Cells* **2018**, *178*, 106–114.

(145) Tackley, D. R.; Dent, G.; Ewen Smith, W. Phthalocyanines: Structure and Vibrations. *Phys. Chem. Chem. Phys.* **2001**, *3*, 1419–1426.

(146) Stöckmann, F. Negative Photoeffekte in Halbleitern. *Zeitschrift für Phys.* **1955**, *143*, 348–356.

(147) Xu, J.; Rechav, K.; Popovitz-Biro, R.; Nevo, I.; Feldman, Y.; Joselevich, E. High-Gain 200 Ns Photodetectors from Self-Aligned CdS-CdSe Core-Shell Nanowalls. *Adv. Mater.* **2018**, *30*, 1800413.

(148) Guo, P.; Xu, J.; Gong, K.; Shen, X.; Lu, Y.; Qiu, Y.; Xu, J.; Zou, Z.; Wang, C.; Yan, H.; Luo, Y.; Pan, A.; Zhang, H.; Ho, J. C.; Yu, K. M. On-Nanowire Axial Heterojunction Design for High-Performance Photodetectors. *ACS Nano* **2016**, *10*, 8474–8481.

(149) Oertel, D. C.; Bawendi, M. G.; Arango, A. C.; Bulović, V. Photodetectors Based on Treated CdSe Quantum-Dot Films. *Appl. Phys. Lett.* **2005**, *87*, 213505.

(150) Nusir, A. I.; Aguilar, J.; Bever, Z.; Manasreh, M. O. Uncooled Photodetectors Based on CdSe Nanocrystals with an Interdigital Metallization. *Appl. Phys. Lett.* **2014**, *104*, 051124.

(151) Shen, T.; Li, B.; Zheng, K.; Pullerits, T.; Cao, G.; Tian, J. Surface Engineering of Quantum Dots for Remarkably High Detectivity Photodetectors. *J. Phys. Chem. Lett.* **2018**, *9*, 3285–3294.

(152) Wurst, K. M.; Bender, M.; Lauth, J.; Maiti, S.; Chassé, T.; Meixner, A.; Siebbeles, L. D. A.; Bunz, U. H. F.; Braun, K.; Scheele, M. Correlated, Dual-Beam Optical Gating in Coupled Organic–Inorganic Nanostructures. *Angew. Chemie Int. Ed.* **2018**, *57*, 11559–

11563.

(153) Hollebone, B. R.; Stillman, M. J. Observation of Davydov Splitting in the MCD Spectra of α Metal-Free Phthalocyanine. *Chem. Phys. Lett.* **1974**, *29*, 284–286.

(154) Kirk, R. S. Crystal Structure and Molecular Orientation in Phthalocyanine Thin Films. *Mol. Cryst.* **1968**, *5*, 211–215.

(155) *Physics of Organic Semiconductors*; Brütting, W., Adachi, C. T. S.-B. M.-C., Eds.; WILEY-VCH, 2012.

(156) Klimov, V. I. Spectral and Dynamical Properties of Multiexcitons in Semiconductor Nanocrystals. *Annu. Rev. Phys. Chem.* **2007**, *58*, 635–673.

(157) Cordones, A. A.; Scheele, M.; Alivisatos, A. P.; Leone, S. R. Probing the Interaction of Single Nanocrystals with Inorganic Capping Ligands: Time-Resolved Fluorescence from CdSe–CdS Quantum Dots Capped with Chalcogenidometalates. *J. Am. Chem. Soc.* **2012**, *134*, 18366–18373.

(158) Kim, D. K.; Lai, Y.; Diroll, B. T.; Murray, C. B.; Kagan, C. R. Flexible and Low-Voltage Integrated Circuits Constructed from High-Performance Nanocrystal Transistors. *Nat. Commun.* **2012**, *3*, 1216.

(159) Stinner, F. S.; Lai, Y.; Straus, D. B.; Diroll, B. T.; Kim, D. K.; Murray, C. B.; Kagan, C. R. Flexible, High-Speed CdSe Nanocrystal Integrated Circuits. *Nano Lett.* **2015**, *15*, 7155–7160.

(160) Yang, X.; Xu, X.; Wang, X.; Ni, H.; Han, Q.; Niu, Z.; Williams, D. A. Optically Controlled Quantum Dot Gated Transistors with High on/off Ratio. *Appl. Phys. Lett.* **2010**, *96*, 083503.

(161) Anthopoulos, T. D. Electro-Optical Circuits Based on Light-Sensing Ambipolar Organic Field-Effect Transistors. *Appl. Phys. Lett.* **2007**, *91*, 113513.

(162) Gong, K.; Zeng, Y.; Kelley, D. F. Extinction Coefficients, Oscillator Strengths, and Radiative Lifetimes of CdSe, CdTe, and CdTe/CdSe Nanocrystals. *J. Phys. Chem. C* **2013**, *117*, 20268–20279.

(163) Nagpal, P.; Klimov, V. I. Role of Mid-Gap States in Charge Transport and Photoconductivity in Semiconductor Nanocrystal Films. *Nat. Commun.* **2011**, *2*, 486.

(164) Adinolfi, V.; Kramer, I. J.; Labelle, A. J.; Sutherland, B. R.; Hoogland, S.; Sargent, E. H. Photojunction Field-Effect Transistor Based on a Colloidal Quantum Dot Absorber Channel Layer. *ACS Nano* **2015**, *9*, 356–362.

(165) Livache, C.; Izquierdo, E.; Martinez, B.; Dufour, M.; Pierucci, D.; Keuleyan, S.; Cruguel, H.; Becerra, L.; Fave, J. L.; Aubin, H.; Ouerghi, A.; Lacaze, E.; Silly, M. G.; Dubertret, B.; Ithurria, S.; Lhuillier, E. Charge Dynamics and Optolectronic Properties in HgTe Colloidal Quantum Wells. *Nano Lett.* **2017**, *17*, 4067–4074.

(166) Britton, J.; Antunes, E.; Nyokong, T. Fluorescence Quenching and Energy Transfer in Conjugates of Quantum Dots with Zinc and Indium Tetraamino Phthalocyanines. *J. Photochem. Photobiol. A Chem.* **2010**, *210*, 1–7.

(167) Shabaev, A.; Efros, A. L.; Efros, A. L. Dark and Photo-Conductivity in Ordered Array of Nanocrystals. *Nano Lett.* **2013**, *13*, 5454–5461.

(168) Prins, F.; Buscema, M.; Seldenthuis, J. S.; Etaki, S.; Buchs, G.; Barkelid, M.; Zwiller, V.; Gao, Y.; Houtepen, A. J.; Siebbeles, L. D. A.; van der Zant, H. S. J. Fast and Efficient Photodetection in Nanoscale Quantum-Dot Junctions. *Nano Lett.* **2012**, *12*, 5740–5743.

(169) Gréboval, C.; Izquierdo, E.; Livache, C.; Martinez, B.; Dufour, M.; Goubet, N.; Moghaddam, N.; Qu, J.; Chu, A.; Ramade, J.; Aubin, H.; Cruguel, H.; Silly, M.; Lhuillier, E.; Ithurria, S. Impact of Dimensionality and Confinement on the Electronic Properties of Mercury Chalcogenide Nanocrystals. *Nanoscale* **2019**, *11*, 3905–3915.

(170) Mir, W. J.; Livache, C.; Goubet, N.; Martinez, B.; Jagtap, A.; Chu, A.; Coutard, N.; Cruguel, H.; Barisien, T.; Ithurria, S.; Nag, A.; Dubertret, B.; Ouerghi, A.; Silly, M. G.; Lhuillier, E. Strategy to Overcome Recombination Limited Photocurrent Generation in CsPbX 3 Nanocrystal Arrays. *Appl. Phys. Lett.* **2018**, *112*, 113503.

(171) Weber, M.; Westendorf, S.; Märker, B.; Braun, K.; Scheele, M. Opportunities and Challenges for Electrochemistry in Studying the Electronic Structure of Nanocrystals. *Phys. Chem. Chem. Phys.* **2019**, *21*, 8992–9001.

(172) Grimaldi, G.; Crisp, R. W.; ten Brinck, S.; Zapata, F.; van Ouwendorp, M.; Renaud, N.; Kirkwood, N.; Evers, W. H.; Kinge, S.; Infante, I.; Siebbeles, L. D. A.; Houtepen, A. J. Hot-Electron Transfer in Quantum-Dot Heterojunction Films. *Nat. Commun.* **2018**, *9*, 2310.

(173) Kim, S.; Fisher, B.; Eisler, H.-J.; Bawendi, M. Type-II Quantum Dots: CdTe/CdSe(Core/Shell) and CdSe/ZnTe(Core/Shell) Heterostructures. *J. Am. Chem. Soc.* **2003**, *125*, 11466–11467.

(174) Sayevich, V.; Guhrenz, C.; Dzhagan, V. M.; Sin, M.; Werheid, M.; Cai, B.; Borchardt, L.; Widmer, J.; Zahn, D. R. T.; Brunner, E.; Lesnyak, V.; Gaponik, N.; Eychmüller, A. Hybrid N -Butylamine-Based Ligands for Switching the Colloidal Solubility and Regimentation of Inorganic-Capped Nanocrystals. *ACS Nano* **2017**, *11*, 1559–1571.

(175) Sayevich, V.; Gaponik, N.; Plötner, M.; Kruszynska, M.; Gemming, T.; Dzhagan, V. M.; Akhavan, S.; Zahn, D. R. T.; Demir, H. V.; Eychmüller, A. Stable Dispersion of Iodide-Capped PbSe Quantum Dots for High-Performance Low-Temperature Processed Electronics and Optoelectronics. *Chem. Mater.* **2015**, *27*, 4328–4337.

(176) Lauth, J.; Kinge, S.; Siebbeles, L. D. A. Ultrafast Transient Absorption and Terahertz Spectroscopy as Tools to Probe Photoexcited States and Dynamics in Colloidal 2D Nanostructures. *Zeitschrift für Phys. Chemie* **2017**, *231*, 107–119.

(177) Konrad, A.; Metzger, M.; Kern, A. M.; Brecht, M.; Meixner, A. J. Controlling the Dynamics of Förster Resonance Energy Transfer inside a Tunable Sub-Wavelength Fabry–Pérot-Resonator. *Nanoscale* **2015**, *7*, 10204–10209.

(178) Luo, J.; Xie, Z.; Lam, J. W. Y.; Cheng, L.; Tang, B. Z.; Chen, H.; Qiu, C.; Kwok, H. S.; Zhan, X.; Liu, Y.; Zhu, D. Aggregation-Induced Emission of 1-Methyl-1,2,3,4,5-Pentaphenylsilole. *Chem. Commun.* **2001**, No. 18, 1740–1741.

(179) Barbara, P. F.; Rand, S. D.; Rentzepis, P. M. Direct Measurements of Tetraphenylethylene Torsional Motion by Picosecond Spectroscopy. *J. Am. Chem. Soc.* **1981**, *103*, 2156–2162.

(180) Bunz, U. H. F. Poly(Aryleneethynylene)s: Syntheses, Properties, Structures, and Applications. *Chem. Rev.* **2000**, *100*, 1605–1644.

(181) Chen, Y.; Lam, J. W. Y.; Kwok, R. T. K.; Liu, B.; Tang, B. Z. Aggregation-Induced Emission: Fundamental Understanding and Future Developments. *Mater. Horizons* **2019**, *6*, 428–433.

(182) Cai, Y.; Du, L.; Samedov, K.; Gu, X.; Qi, F.; Sung, H. H. Y.; Patrick, B. O.; Yan, Z.; Jiang, X.; Zhang, H.; Lam, J. W. Y.; Williams, I. D.; Lee Phillips, D.; Qin, A.; Tang, B.

Z. Deciphering the Working Mechanism of Aggregation-Induced Emission of Tetraphenylethylene Derivatives by Ultrafast Spectroscopy. *Chem. Sci.* **2018**, *9*, 4662–4670.

(183) Bunz, U. H. F. Poly(Aryleneethynylene)S. *Macromol. Rapid Commun.* **2009**, *30*, 772–805.

(184) Leung, N. L. C.; Xie, N.; Yuan, W.; Liu, Y.; Wu, Q.; Peng, Q.; Miao, Q.; Lam, J. W. Y.; Tang, B. Z. Restriction of Intramolecular Motions: The General Mechanism behind Aggregation-Induced Emission. *Chem. - A Eur. J.* **2014**, *20*, 15349–15353.

(185) Parrott, E. P. J.; Tan, N. Y.; Hu, R.; Zeitler, J. A.; Tang, B. Z.; Pickwell-Macpherson, E. Direct Evidence to Support the Restriction of Intramolecular Rotation Hypothesis for the Mechanism of Aggregation-Induced Emission: Temperature Resolved Terahertz Spectra of Tetraphenylethene. *Mater. Horizons* **2014**, *1*, 251–258.

(186) Yamamoto, N. Mechanisms of Aggregation-Induced Emission and Photo/Thermal E / Z Isomerization of a Cyanostilbene Derivative: Theoretical Insights. *J. Phys. Chem. C* **2018**, *122*, 12434–12440.

(187) Maity, S.; Wu, W. C.; Tracy, J. B.; Clarke, L. I.; Bochinski, J. R. Nanoscale Steady-State Temperature Gradients within Polymer Nanocomposites Undergoing Continuous-Wave Photothermal Heating from Gold Nanorods. *Nanoscale* **2017**, *9*, 11605–11618.

(188) Borzenkov, M.; Pallavicini, P.; Chirico, G. Photothermally Active Inorganic Nanoparticles: From Colloidal Solutions to Photothermally Active Printed Surfaces and Polymeric Nanocomposite Materials. *Eur. J. Inorg. Chem.* **2019**, *2019*, 4397–4404.

(189) Park, C. H.; Yun, H.; Yang, H.; Lee, J.; Kim, B. J. Fluorescent Block Copolymer-MoS 2 Nanocomposites for Real-Time Photothermal Heating and Imaging. *Adv. Funct. Mater.* **2017**, *27*, 1604403.

(190) Crane, M. J.; Zhou, X.; Davis, E. J.; Pauzauskie, P. J. Photothermal Heating and Cooling of Nanostructures. *Chem. - An Asian J.* **2018**, *13*, 2575–2586.

(191) Resch-Genger, U.; Grabolle, M.; Cavaliere-Jaricot, S.; Nitschke, R.; Nann, T. Quantum Dots versus Organic Dyes as Fluorescent Labels. *Nat. Methods* **2008**, *5*, 763–775.

(192) Lutich, A. A.; Jiang, G.; Susha, A. S.; Rogach, A. L.; Stefani, F. D.; Feldmann, J. Energy Transfer versus Charge Separation in Type-II Hybrid Organic-Inorganic

Nanocomposites. *Nano Lett.* **2009**, *9*, 2636–2640.

(193) Walker, B. J.; Nair, G. P.; Marshall, L. F.; Bulović, V.; Bawendi, M. G. Narrow-Band Absorption-Enhanced Quantum Dot/J-Aggregate Conjugates. *J. Am. Chem. Soc.* **2009**, *131*, 9624–9625.

(194) Beane, G.; Boldt, K.; Kirkwood, N.; Mulvaney, P. Energy Transfer between Quantum Dots and Conjugated Dye Molecules. *J. Phys. Chem. C* **2014**, *118*, 18079–18086.

(195) Luo, X.; Han, Y.; Chen, Z.; Li, Y.; Liang, G.; Liu, X.; Ding, T.; Nie, C.; Wang, M.; Castellano, F. N.; Wu, K. Mechanisms of Triplet Energy Transfer across the Inorganic Nanocrystal/Organic Molecule Interface. *Nat. Commun.* **2020**, *11*, 1–10.

(196) Freyria, F. S.; Cordero, J. M.; Caram, J. R.; Doria, S.; Dodin, A.; Chen, Y.; Willard, A. P.; Bawendi, M. G. Near-Infrared Quantum Dot Emission Enhanced by Stabilized Self-Assembled J-Aggregate Antennas. *Nano Lett.* **2017**, *17*, 7665–7674.

(197) Stöferle, T.; Scherf, U.; Mahrt, R. F. Energy Transfer in Hybrid Organic/ Inorganic Nanocomposites. *Nano Lett.* **2009**, *9*, 453–456.

(198) Guzelturk, B.; Demir, H. V. Near-Field Energy Transfer Using Nanoemitters For Optoelectronics. *Adv. Funct. Mater.* **2016**, *26*, 8158–8177.

(199) Zhang, H.; Rominger, F.; Bunz, U. H. F.; Freudenberg, J. Aggregation-Induced Emission of Triphenyl-Substituted Tristyrylbenzenes. *Chem. – A Eur. J.* **2019**, *25*, 11218–11222.

(200) Zucchero, A. J.; McGrier, P. L.; Bunz, U. H. F. Cross-Conjugated Cruciform Fluorophores. *Acc. Chem. Res.* **2010**, *43*, 397–408.

(201) Li, N.; Jia, K.; Wang, S.; Xia, A. Theoretical Study of Spectroscopic Properties of Dimethoxy- p -Phenylene-Ethynylene Oligomers: Planarization of the Conjugated Backbone †. *J. Phys. Chem. A* **2007**, *111*, 9393–9398.

(202) Miteva, T.; Palmer, L.; Kloppenburg, L.; Neher, D.; Bunz, U. H. F. Interplay of Thermochromicity and Liquid Crystalline Behavior in Poly(p- Phenyleneethynylene)s: Π−π Interactions or Planarization of the Conjugated Backbone? *Macromolecules* **2000**, *33*, 652–654.

(203) Sluch, M. I.; Godt, A.; Bunz, U. H. F.; Berg, M. A. Excited-State Dynamics of Oligo(p

-Phenyleneethynylene): Quadratic Coupling and Torsional Motions. *J. Am. Chem. Soc.* **2001**, *123*, 6447–6448.

(204) Wierzbicka, M.; Bylińska, I.; Czaplewski, C.; Wiczk, W. Experimental and Theoretical Studies of the Spectroscopic Properties of Simple Symmetrically Substituted Diphenylacetylene Derivatives. *RSC Adv.* **2015**, *5*, 29294–29303.

(205) Panzer, F.; Bässler, H.; Köhler, A. Temperature Induced Order-Disorder Transition in Solutions of Conjugated Polymers Probed by Optical Spectroscopy. *J. Phys. Chem. Lett.* **2017**, *8*, 114–125.

(206) Castruita, G.; Arias, E.; Moggio, I.; Pérez, F.; Medellín, D.; Torres, R.; Ziolo, R.; Olivas, A.; Giorgetti, E.; Muniz-Miranda, M. Synthesis, Optical Properties and Supramolecular Order of π-Conjugated 2,5-Di(Alcoxy)Phenyleneethynylene Oligomers. *J. Mol. Struct.* **2009**, *936*, 177–186.

(207) Köhler, A.; Khan, A. L. T.; Wilson, J. S.; Dosche, C.; Al-Suti, M. K.; Shah, H. H.; Khan, M. S. The Role of C-H and C-C Stretching Modes in the Intrinsic Non-Radiative Decay of Triplet States in a Pt-Containing Conjugated Phenylene Ethynylene. *J. Chem. Phys.* **2012**, *136*, 094905.

(208) Min, Y.; Akbulut, M.; Kristiansen, K.; Golan, Y.; Israelachvili, J. The Role of Interparticle and External Forces in Nanoparticle Assembly. *Nat. Mater.* **2008**, *7*, 527–538.

(209) Maier, A.; Lapkin, D.; Mukharamova, N.; Frech, P.; Assalauova, D.; Ignatenko, A.; Khubbutdinov, R.; Lazarev, S.; Sprung, M.; Laible, F.; Löffler, R.; Previdi, N.; Bräuer, A.; Günkel, T.; Fleischer, M.; Schreiber, F.; Vartanyants, I. A.; Scheele, M. Structure–Transport Correlation Reveals Anisotropic Charge Transport in Coupled PbS Nanocrystal Superlattices. *Adv. Mater.* **2020**, *32*, 2002254.

(210) Fetzer, F.; Maier, A.; Hodas, M.; Geladari, O.; Braun, K.; Meixner, A. J.; Schreiber, F.; Schnepf, A.; Scheele, M. *Structural Order Matters: Enhanced Electronic Coupling in Self Assembled Micro-Crystals of Au-Nanoclusters*; 2020.

(211) Chen, W.; Zhong, J.; Li, J.; Saxena, N.; Kreuzer, L. P.; Liu, H.; Song, L.; Su, B.; Yang, D.; Wang, K.; Schlipf, J.; Körstgens, V.; He, T.; Wang, K.; Müller-Buschbaum, P. Structure and Charge Carrier Dynamics in Colloidal PbS Quantum Dot Solids. *J. Phys.*

Chem. Lett. **2019**, *10*, 2058–2065.

(212) Bian, K.; Choi, J. J.; Kaushik, A.; Clancy, P.; Smilgies, D. M.; Hanrath, T. Shape-Anisotropy Driven Symmetry Transformations in Nanocrystal Superlattice Polymorphs. *ACS Nano* **2011**, *5*, 2815–2823.

(213) Weidman, M. C.; Smilgies, D. M.; Tisdale, W. A. Kinetics of the Self-Assembly of Nanocrystal Superlattices Measured by Real-Time in Situ X-Ray Scattering. *Nat. Mater.* **2016**, *15*, 775–781.

(214) Hanrath, T.; Choi, J. J.; Smilgies, D.-M. Structure/Processing Relationships of Highly Ordered Lead Salt Nanocrystal Superlattices. *ACS Nano* **2009**, *3*, 2975–2988.

(215) Goodfellow, B. W.; Patel, R. N.; Panthani, M. G.; Smilgies, D.-M.; Korgel, B. A. Melting and Sintering of a Body-Centered Cubic Superlattice of PbSe Nanocrystals Followed by Small Angle X-Ray Scattering. *J. Phys. Chem. C* **2011**, *115*, 6397–6404.

(216) Evers, W. H.; Schins, J. M.; Aerts, M.; Kulkarni, A.; Capiod, P.; Berthe, M.; Grandidier, B.; Delerue, C.; Van Der Zant, H. S. J.; Van Overbeek, C.; Peters, J. L.; Vanmaekelbergh, D.; Siebbeles, L. D. A. High Charge Mobility in Two-Dimensional Percolative Networks of PbSe Quantum Dots Connected by Atomic Bonds. *Nat. Commun.* **2015**, *6*, 1–8.

(217) Choi, J. J.; Bealing, C. R.; Bian, K.; Hughes, K. J.; Zhang, W.; Smilgies, D.-M.; Hennig, R. G.; Engstrom, J. R.; Hanrath, T. Controlling Nanocrystal Superlattice Symmetry and Shape-Anisotropic Interactions through Variable Ligand Surface Coverage. *J. Am. Chem. Soc.* **2011**, *133*, 3131–3138.

(218) Winslow, S. W.; Swan, J. W.; Tisdale, W. A. The Importance of Unbound Ligand in Nanocrystal Superlattice Formation. *J. Am. Chem. Soc.* **2020**.

(219) Murray, C. B.; Kagan, C. R.; Bawendi, M. G. Self-Organization of CdSe Nanocrystallites into Three-Dimensional Quantum Dot Superlattices. *Science* **1995**, *270*, 1335–1338.

(220) Kalyuzhny, G.; Murray, R. W. Ligand Effects on Optical Properties of CdSe Nanocrystals. *J. Phys. Chem. B* **2005**, *109*, 7012–7021.

(221) Dabbousi, B. O.; Bawendi, M. G.; Onitsuka, O.; Rubner, M. F. Electroluminescence from CdSe Quantum - Dot / Polymer Composites Electroluminescence from CdSe

Quantum-Dot / Polymer Composites. *Appl. Phys. Lett.* **2014**, *1316*, 11–14.

(222) Mattoussi, H.; Radzilowski, L. H.; Dabbousi, B. O.; Thomas, E. L.; Bawendi, M. G.; Rubner, M. F. Electroluminescence from Heterostructures of Poly(Phenylene Vinylene) and Inorganic CdSe Nanocrystals. *J. Appl. Phys.* **1998**, *83*, 7965–7974.

(223) Coe, S.; Woo, W. K.; Bawendi, M.; Bulović, V. Electroluminescence from Single Monolayers of Nanocrystals in Molecular Organic Devices. *Nature* **2002**, *420*, 800–803.

(224) Antanovich, A.; Prudnikau, A.; Matsukovich, A.; Achtstein, A.; Artemyev, M. Self-Assembly of CdSe Nanoplatelets into Stacks of Controlled Size Induced by Ligand Exchange. *J. Phys. Chem. C* **2016**, *120*, 5764–5775.

(225) Qiao, F.; Wang, X.; Wang, Q.; He, G.; Xie, Y. Functionalized Self-Assembly of Colloidal CdX (X = S, Se) Nanorods on Solid Substrates for Device Applications. *Nanoscale* **2017**, *9*, 8066–8079.

(226) Boles, M. A.; Talapin, D. V. Self-Assembly of Tetrahedral Cdse Nanocrystals: Effective "Patchiness" via Anisotropic Steric Interaction. *J. Am. Chem. Soc.* **2014**, *136*, 5868–5871.

(227) Zheng, X.; Lee, H.; Weisgraber, T. H.; Shusteff, M.; DeOtte, J.; Duoss, E. B.; Kuntz, J. D.; Biener, M. M.; Ge, Q.; Jackson, J. A.; Kucheyev, S. O.; Fang, N. X.; Spadaccini, C. M. Ultralight, Ultrastiff Mechanical Metamaterials. *Science* **2014**, *344*, 1373–1377.

(228) Lim, S. J.; Schleife, A.; Smith, A. M. Optical Determination of Crystal Phase in Semiconductor Nanocrystals. *Nat. Commun.* **2017**, *8*, 14849.

(229) Yang, Y. A.; Wu, H.; Williams, K. R.; Cao, Y. C. Synthesis of CdSe and CdTe Nanocrystals without Precursor Injection. *Angew. Chemie Int. Ed.* **2005**, *44*, 6712–6715.

(230) Mahler, B.; Lequeux, N.; Dubertret, B. Ligand-Controlled Polytypism of Thick-Shell CdSe/CdS Nanocrystals. *J. Am. Chem. Soc.* **2010**, *132*, 953–959.

(231) Fritzinger, B.; Capek, R. K.; Lambert, K.; Martins, J. C.; Hens, Z. Utilizing Self-Exchange To Address the Binding of Carboxylic Acid Ligands to CdSe Quantum Dots. *J. Am. Chem. Soc.* **2010**, *132*, 10195–10201.

(232) Liu, M.; Wang, Y. Y.; Liu, Y.; Jiang, F. L. Thermodynamic Implications of the Ligand Exchange with Alkylamines on the Surface of CdSe Quantum Dots: The Importance of

Ligand-Ligand Interactions. *J. Phys. Chem. C* **2020**, *124*, 4613–4625.

(233) Talapin, D. V; Rogach, A. L.; Kornowski, A.; Haase, M.; Weller, H. Highly Luminescent Monodisperse CdSe and CdSe/ZnS Nanocrystals Synthesized in a Hexadecylamine-Trioctylphosphine Oxide-Trioctylphospine Mixture. *Nano Lett* **2001**, *1*, 207–211.

(234) Jang, J.; Dolzhnikov, D. S.; Liu, W.; Nam, S.; Shim, M.; Talapin, D. V. Solution-Processed Transistors Using Colloidal Nanocrystals with Composition-Matched Molecular "Solders": Approaching Single Crystal Mobility. *Nano Lett.* **2015**, *15*, 6309–6317.

(235) Märker, B.; Hiller, J.; Wackenhut, F.; Braun, K.; Meixner, A.; Scheele, M. Simultaneous Positive and Negative Optical Patterning with Dye-Sensitized CdSe Quantum Dots. *J. Chem. Phys.* **2019**, *151*, 141102.

(236) Zhang, X.-F.; Li, X.; Niu, L.; Sun, L.; Liu, L. Charge Transfer Photophysics of Tetra(α-Amino) Zinc Phthalocyanine. *J. Fluoresc.* **2009**, *19*, 947–954.

(237) Helmchen, G.; Nill, G.; Flockerzi, D.; Youssef, M. S. K. Preparative Scale Directed Resolution of Enantiomeric Carboxylic Acids and Lactonesvia Liquid Chromatography and Neighboring-Group Assisted Hydrolysis of Diastereomeric Amides. *Angew. Chemie Int. Ed. English* **1979**, *18*, 63–65.

(238) Fulmer, G. R.; Miller, A. J. M.; Sherden, N. H.; Gottlieb, H. E.; Nudelman, A.; Stoltz, B. M.; Bercaw, J. E.; Goldberg, K. I. NMR Chemical Shifts of Trace Impurities: Common Laboratory Solvents, Organics, and Gases in Deuterated Solvents Relevant to the Organometallic Chemist. *Organometallics* **2010**, *29*, 2176–2179.

(239) Armarego, W. L. F.; Chai, C. L. L. *Purification of Laboratory Chemicals*; Elsevier, 2003.

(240) Mattern, D. L. Direct Aromatic Periodination. *J. Org. Chem.* **1984**, *49*, 3051–3053.

(241) Brecht, M.; Studier, H.; Elli, A. F.; Jelezko, F.; Bittl, R. Assignment of Red Antenna States in Photosystem I from Thermosynechoccocus Elongatus by Single-Molecule Spectroscopy. *Biochemistry* **2007**, *46*, 799–806.

(242) Hussels, M.; Konrad, A.; Brecht, M. Confocal Sample-Scanning Microscope for Single-Molecule Spectroscopy and Microscopy with Fast Sample Exchange at Cryogenic

Temperatures. *Rev. Sci. Instrum.* **2012**, *83*, 123706.

(243) Wackenhut, F.; Failla, A. V.; Meixner, A. J. Multicolor Microscopy and Spectroscopy Reveals the Physics of the One-Photon Luminescence in Gold Nanorods. *J. Phys. Chem. C* **2013**, *117*, 17870–17877.